Print ISSN 0033-9008
Online ISSN 1880-1765

QUARTERLY REPORT of RTRI

Feb. 2024 Vol. 65 No. 1

CONTENTS

[H] Human factors
[I] Infrastructure
[O] Operations
[R] Rolling stock
[T] Technical system integration and interaction
[W] Weather and climate change

RAILWAY TECHNICAL RESEARCH INSTITUTE

QUARTERLY REPORT of RTRI

Print ISSN 0033-9008
Online ISSN 1880-1765

February 2024 Vol. 65 No. 1

CONTENTS

PAPERS

SUMMARIES

[H] Human factors
[I] Infrastructure
[O] Operations
[R] Rolling stock
[T] Technical system integration and interaction
[W] Weather and climate change

Application of Phased Array Ultrasonic Testing Method to Flaw Detection in Vehicle Bogie Parts

Kazunari MAKINO
Vehicle & Bogie Parts Strength Laboratory, Vehicle Technology Division

An imaging technology using phased array ultrasonic testing (PAUT) was applied to bogie parts inspection, targeting welded members in bogie frames and wheel seats in axles. Regarding bogie frames, the superiority of PAUT was confirmed in detecting inclined surface flaws, and the influence of paint thickness on the flaw detection was clarified. When PAUT was applied to an actual bogie frame, the results of flaw detection were visualized clearly, demonstrating the effectiveness of PAUT in bogie frames. Regarding axles, when PAUT was applied to a wheel seat using shear-wave and longitudinal-wave angle-beam inspection techniques, flaws on the wheel seat were detected and visualized in a wheel-fitted state.

***Key words*:** *phased array ultrasonic testing (PAUT), bogie frame, axle, visualization*

1. Introduction

Nondestructive inspection techniques such as ultrasonic testing and magnetic particle testing are applied to bogie parts such as bogie frames and axles of railway vehicles during manufacturing or periodic inspection [1].

During the manufacturing process of bogie frames with welded structures, the primary welds are subjected to internal inspection using ultrasonic testing to ensure a specified level of weld quality. On this basis, inspection systems for flaws on the surface of welds caused by in-service loads have been established in periodic inspections of railway vehicles, mainly by visual testing and magnetic particle testing. However, several cases of bogie frame damage have occurred in recent years. They are thought to originate from the weld root between the side beam of a bogie frame and a bogie member, or from the weld toe between the side beam and its internal reinforcement, as shown in Fig. 1 [2, 3]. As a result, railway operators are now required to have internal inspection techniques for welds of bogie frames in periodic inspections, depending on the type of bogies.

In periodic inspections, magnetic particle testing is used for surface flaws on axles, while ultrasonic testing is used for flaws on the fitted surfaces with wheels, gears, and so on that are not visually accessible. Recently, no cases of safety-threatening damage to axles have occurred in Japan. However, in ultrasonic testing in particular, significant experience is required to determine the presence or absence of flaws from ultrasonic waveforms, which poses a challenge for technology transfer in vehicle inspection and repair sites.

As mentioned above, ultrasonic testing plays a significant role in the nondestructive testing of bogie parts such as bogie frames and axles. Currently, the mainstream application is the conventional ultrasonic angle-beam testing method (hereinafter referred to as conventional UT), which uses an angle probe with only one transducer. On the other hand, as one of the techniques in ultrasonic testing, phased array ultrasonic testing (PAUT) method [4] has attracted attention recently. PAUT is a method of testing by electronically controlling the direction of propagation and focus of ultrasonic waves using an array probe with many transducers arranged in parallel. The application of PAUT method to the inspection of structures other than railway vehicles is increasing owing to its high performance in flaw detection and easier determination of flaws by visualizing flaw detection results.

This report presents the results of visualizing and detecting flaws by applying ultrasonic imaging technology with PAUT to welds of bogie frames and fitted parts such as wheel seats of axles. After overviewing conventional UT and PAUT, we evaluated the detection performance of PAUT when it was applied to flaws on the side beam of a bogie frame whose faces were inclined to the surface of the side beam. Furthermore, the influence of the presence or absence of coating (paint thickness) on the surface of the bogie frame on the flaw detection was evaluated, and then PAUT was applied to an actual bogie frame to confirm its flaw detection performance. Finally, we show the results when PAUT by the shear-wave angle beam and longitudinal-wave angle beam was applied to axles.

2. Overview of phased array ultrasonic testing (PAUT)

Figure 2 shows a conceptual diagram comparing conventional UT with PAUT in ultrasonic angle-beam flaw detection. As shown in Fig. 2(a), the probe used in conventional UT usually incorporates one transducer, which transmits ultrasonic waves with a single refraction angle such as 45° or 70°. In actual flaw detection, inspection technicians read the distance, or beam path length of the ultrasonic

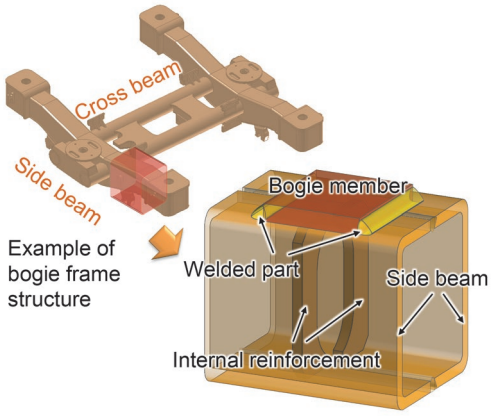

Fig. 1 Schematic of railway bogie frame with welded structure

wave reflected by the flaw (flaw echo) from the waveform that changes in real time with the probe scanning. It is necessary to evaluate the presence or absence of flaws and their positions based on the path length and the refraction angle of the probe. Therefore, the inspection technicians are required to have a specified level of skill and experience. In addition, it is necessary to use multiple probes with different refraction angles according to the inclination of a flaw and the positional relationship between the probe and the flaw.

In PAUT with a typical linear array probe, dozens of transducers (elements) are arranged in a row and embedded. Ultrasonic waves with various refraction angles are transmitted sequentially using the sector scan as shown in Fig. 2(b), by controlling the order (1 to 8 in the figure) and time difference in the excitation of transducers. For example, ultrasonic waves with refraction angles from 40° to 75° at intervals of 0.5° can be transmitted. Furthermore, each received wave in the sector scan is color-coded according to the echo height along the path length. By arranging them in a sectorial shape according to their refraction angles, the flaw detection results can be visualized in a cross-sectional manner. As a result, it becomes easier to capture the flaw positions in relation to the actual shape of test object.

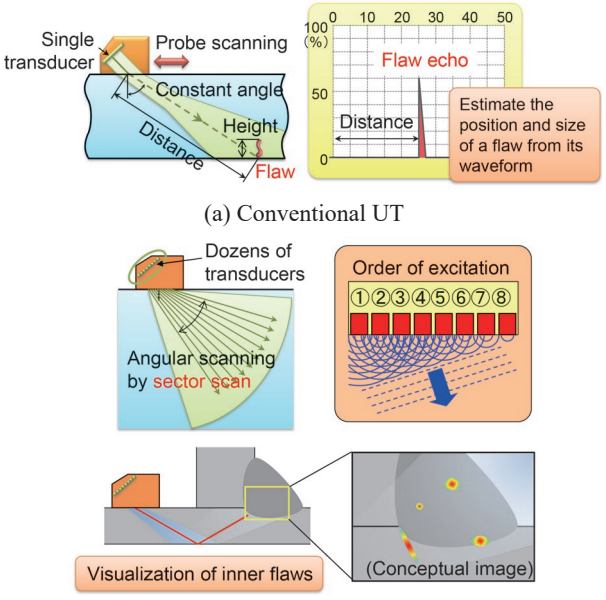

Fig. 2 Conceptual diagram comparing conventional UT with PAUT

3. Influence of flaw inclination on its detection

3.1 Overview

In ultrasonic flaw detection of surface flaws in steel plates that constitute a bogie frame, when flaw faces are perpendicular to the surface of the plate (the angle of inclination is 0°), the reflection behavior of ultrasonic waves is simple. Under these conditions, flaws can be readily detected. If the flaw faces are inclined to the surface of the plate, it may be difficult to detect them. In a structure in which a steel plate is butt-welded as shown in Fig. 3(a), weld defects that are inclined to the surface may occur depending on the groove angle. In a structure in which a bogie member is welded to the surface of a steel plate as shown in Fig. 3(b), fatigue cracks may occur depending on the shape of the heat-affected zone (HAZ) of the fillet weld. Therefore, it is important to quantitatively understand the detection performance of inclined surface flaws.

In this chapter, both of conventional UT, whose refraction angle is 70° used traditionally for the welded part of steel plates, and PAUT were targeted. When surface flaws inclined at various angles from −60° to +60° were inspected by the angle beam testing method with the single-bounce ultrasound, the behavior of ultrasound propagation was analyzed by ultrasound simulation. We focused on the echo height of the received wave with the change in the inclination angle of the surface flaw, and compared the superiority of PAUT over conventional UT in detecting inclined surface flaws.

In chapters 3 to 5, it is noted that both conventional UT and PAUT utilized shear-wave angle beams in all tests of bogie frames.

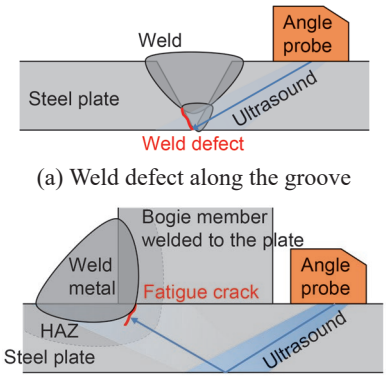

Fig. 3 Examples of inclined surface flaws generated in the welded part of steel plates in bogie frames

3.2 Analysis method

3.2.1 Analysis model

Figure 4 shows the two-dimensional finite element models used to evaluate the influence of flaw inclination on its detection. The thickness t of a steel plate was 8 mm, and a flaw with a height of d = 1.76 mm was placed on the surface of the steel plate. In conventional UT with a refraction angle of $\theta = 70°$, a vertically drilled hole with a diameter of 4 mm and height of 4 mm (hereinafter referred to as ø4 × 4 mm VDH) is used for the sensitivity adjustment. The height of d = 1.76 mm corresponds to a flaw that gives an echo height four times that of ø4 × 4 mm VDH. The inclination angle η of the flaw was defined as 0° when the flaw was perpendicular to the steel plate surface, and was changed in the range of −60° to +60° at intervals of 5°. The sign of the inclination angle η was defined as positive when the flaw was inclined away from the probe.

A situation where flaws are detected by the single-bounce method was assumed. The probe position when the distance from the probe index point to the flaw was one skip (= $2t \tan \theta$ = approx. 44.0 mm) was defined as "0 mm in the probe position." The sign of the probe position was defined as positive when the probe was moved from the reference position to the side approaching the flaw. The conventional UT probe was equipped with a transducer with a width of 5 mm and a refraction angle of 70°. The transducer in the PAUT probe consisted of 32 elements, each with a width of 0.31 mm, and the total width of the transducer was approximately 10 mm (0.31 mm × 32 elements). The wedge angle of the PAUT probe was

36°, and ultrasonic waves with a refraction angle of approximately 53.9° were transmitted without phase control of the array transducer. Table 1 shows material properties used in analysis models.

3.2.2 Analysis procedure

The direction of probe scanning in the analysis is also shown in Fig. 4 above. With the conventional UT, the probe scanned back and forth and the probe position was changed in the range of −10 mm to +10 mm at 1-mm intervals. For the PAUT, the refraction angle in the sector scan was changed in the range of 40° to 75° at 1° intervals. The focal length for PAUT was set to 50 mm.

The frequency of the transmitted wave was set to 5 MHz for both conventional UT and PAUT. Each probe scanned respective models with different inclination angles of η in the manner described above. The maximum absolute value of the received waves from the flaw in a series of scanning was defined as the echo height h. It is noted that h was calculated by the sum of volumetric strain in all transducer elements. The obtained echo height was evaluated in the percentage value when the echo height of ø4 × 4 mm VDH was adjusted to 80%. This VDH-80% echo height corresponds to the H line in the distance-amplitude curve (DAC) for flaw echo evaluation in JIS Z 3060:2015 [5]. Ultrasound simulation software ComWAVE Ver.11.0.0 developed by ITOCHU Techno-Solutions Corporation (CTC) [6] was used for the calculation.

3.3 Analysis results

The relationship between the flaw inclination angle η and the echo height h in conventional UT with a refraction angle of 70° is shown as a blue line in Fig. 5. The echo height was high for a flaw of $\eta = 0°$ and that inclined at a specific angle such as $\eta = \pm 20°$, which is the complementary angle of the refraction angle of $\theta = 70°$. However, it decreased sharply as the angle η increased.

The analysis results for PAUT are shown as an orange line in Fig. 5 in comparison with conventional UT. The echo height h in PAUT was higher than that in conventional UT over the entire angle η of flaw inclination, demonstrating the superiority of PAUT in detecting inclined surface flaws. In particular, the superiority of PAUT in detection of flaws with $\eta > 0$ inclined at an obtuse angle as viewed from the probe was significant.

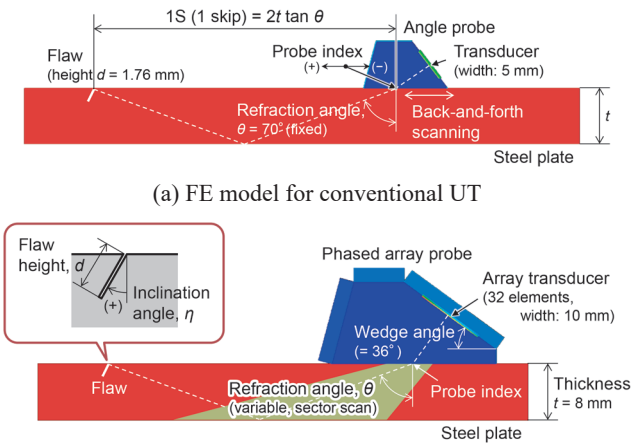

(a) FE model for conventional UT

(b) FE model for PAUT

Fig. 4 Two-dimensional finite element models to evaluate the influence of flaw inclination on its detection

Table 1 Material properties used in analysis models

Element	Material	Long.-wave sound velocity, c_L (m/s)	Shear-wave sound velocity, c_T (m/s)	Density, ρ (kg/m^3)
Bogie frame (Steel plate)	Steel	5900	3230	7800
Probe wedge (for conv. UT)	PMMA (Acrylic resin)	2730	1430	1180
Probe wedge (for PAUT)	Rexolite® (Polystyrene copolymer)	2350	1250	1050

4. Influence of paint thickness on flaw detection

4.1 Overview

In ultrasonic flaw detection of painted structures, it is common practice to remove the paint layer which is to be scanned with a probe before conducting the inspection. The reason for this is to avoid the attenuation of ultrasound in the paint layer during the back-and-forth propagation of ultrasound from the probe to the inside of the test object through the paint layer. It also helps prevent the transmission loss of ultrasound between the probe and the paint layer, as well as between the paint layer and the surface of test object. However, removal of the paint layer requires the use of wire brushes or stripping agents, taking considerable time and effort during the inspection process.

This chapter presents the influence of paint thickness on the echo height in both conventional UT and PAUT, targeting the surface of a steel test piece equivalent to the bogie frame. The echo height from the reflection source at a certain distance from the probe was analyzed using ultrasound simulation, while changing the thickness of paint layer from 0 mm to approximately 1 mm.

4.2 Analysis method

4.2.1 Analysis model

Figure 6 shows the two-dimensional analysis model used to evaluate the influence of paint thickness on the flaw detection. A circumferential surface with a radius of 50 mm (hereinafter referred to as the R surface) was used as a reflection source. The dimensions of the probe model and the configuration of transducers was the same as in Section 3.2.1.

The material properties used in the analysis model were the same as those in Table 1 except for the paint layer. The paint layer

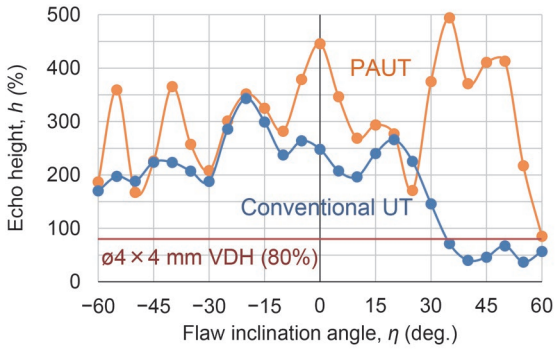

Fig. 5 Relationship between flaw inclination angle and echo height in conventional UT and PAUT

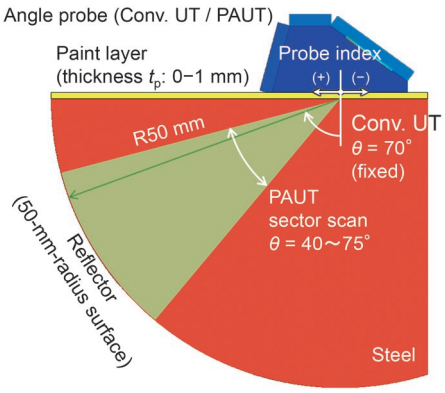

Fig. 6 Two-dimensional finite element model to evaluate the influence of paint thickness on flaw detection

was regarded to be made of a material equivalent to acrylic resin and have the same material properties as the "probe wedge (for conventional UT)" in Table 1. In order to evaluate the influence of paint thickness on the flaw detection, it is necessary to set the attenuation coefficient α of the paint layer. The attenuation coefficient α is generally defined as dB/m (the attenuation in decibel when ultrasonic waves propagate over a distance of one meter). In this analysis model, the value of α = 500 dB/m, which is based on general measurements at a frequency of 5 MHz [7], was applied.

4.2.2 Analysis procedure

In the analysis, the surface of paint layer was scanned with the probe. For the conventional UT, the probe scanned the paint layer back and forth, and the probe position was changed in the range of −3 mm to +3 mm at intervals of 0.5 mm. With the PAUT, the analysis was conducted by changing the refraction angle of sector scan in the range of 40° to 75° at 1° intervals. The focal length for PAUT was set to 50 mm, the same as in Section 3.2.2. The frequency of the transmission wave was set to 5 MHz for both conventional UT and PAUT.

The paint thickness t_p was set to seven steps of 0, 0.16, 0.32, 0.48, 0.64, 0.8, and 0.96 mm (0.16 mm interval) for conventional UT, and nine steps of the seven steps plus 0.08 and 0.24 mm for PAUT. In the conventional UT, the received wave from the R surface at each probe position was calculated when the paint layer in the model for each paint thickness was scanned back and forth with the probe. The maximum value obtained by polynomial approximation of these received waves with respect to the probe position was taken as the echo height h for each paint thickness. The obtained echo height h was normalized to the echo height with the paint thickness t_p of 0 mm as 100%, and then the influence of paint thickness t_p on the echo height h was evaluated. For the PAUT, the echo height h was calculated for beams with refraction angles from 40° to 75° in each paint thickness model. The influence of paint thickness t_p on the echo height h was evaluated for each refraction angle.

4.3 Analysis results

Figure 7 shows the relationship between the paint thickness t_p and the echo height h when the paint thickness was changed from 0 mm to approximately 1 mm in conventional UT. The echo height decreased monotonically as paint thickness increased. By linearly approximating the graph in Fig. 7, the relationship between paint thickness t_p (mm) and echo height h (%) was expressed by the equation: $h = 100\ (1 - 0.196\ t_p)$. That is, the echo height decreased by approximately 20% per 1-mm increase of paint thickness. When conducting flaw detection over a paint layer using conventional UT, it is necessary to set the flaw detection threshold considering the echo height reduction caused by ultrasonic wave attenuation in the paint layer, as determined by the above equation.

Figure 8 shows the relationship between the paint thickness t_p and the echo height h at each refraction angle of θ = 40°, 50°, 60°, and 70° when the paint thickness was changed from 0 mm to approximately 1 mm in PAUT. At any refraction angle of θ, the monotonic decrease in echo height h with increasing the paint thickness t_p, which was observed in conventional UT, was not observed. The relationship between the paint thickness and the echo height changed according to the refraction angle θ. However, within the range up to t_p = 0.96 mm, which was the maximum value of paint thickness investigated, the echo height reduction against those without paint layer was within 20% in all cases of refraction angle θ.

5. Flaw detection test on actual bogie frame

5.1 Overview

So far, we have clarified the characteristics and issues in applying PAUT to bogie frames by comparing them with conventional UT, through the evaluation of the influence of flaw inclination and paint thickness on the echo height. In this chapter, we explain how to set up the flaw detector and adjust the sensitivity in order to apply PAUT to the welded part of the actual bogie frame. The effectiveness of PAUT in the flaw detection of bogie frames is confirmed based on the visualized flaw detection results.

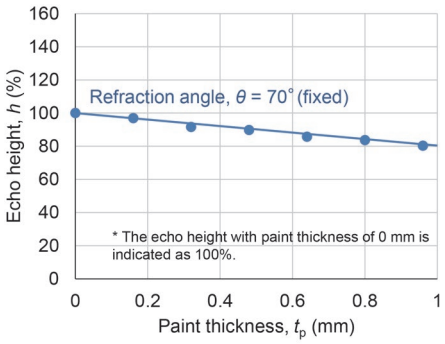

Fig. 7 Relationship between paint thickness and echo height in conventional UT

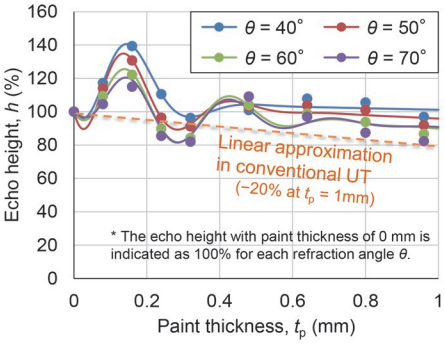

Fig. 8 Relationship between paint thickness and echo height at each refraction angle in PAUT

5.2 Flaw detection method

5.2.1 Flaw detector and its settings

Figure 9 shows the configuration of PAUT flaw detector. All components of the flaw detection system were made by ZETEC Inc. The main body was TOPAZ64 (maximum number of simultaneous excitation elements: 64), the linear-array probe was AM-10MHZ (frequency: 10 MHz, number of elements: 32, each element size: 10 mm × 0.31 mm), and the wedge was AM-55SW (refraction angle: 55°). A 1-axis rotary encoder was attached to the probe to record the probe position during scanning. Table 2 shows typical settings of the flaw detector. The focus setting was a "projection" mode, which focuses ultrasonic waves of all refraction angles at a position where the horizontal distance from the probe is constant.

5.2.2 Sensitivity adjustment

In flaw detection by PAUT, the sensitivity was adjusted according to the following procedures (1) to (3):

(1) Adjust sensitivity for each refraction angle on the 100-mm radius surface in the STB-A1 standard test block [8], ensuring constant echo heights for refraction angles between 40° to 75° in the sector scan range.
(2) Set the focus to align ultrasonic waves of all refracted angles at a horizontal distance of one skip from the probe index point, which is determined by 70° refracted ultrasound in an 8-mm-thick test piece.
(3) To maintain compatibility with conventional UT, adjust the entire flaw detector gain so that the echo height of ø4 × 4 mm VDH tested with 70° refracted ultrasound is at 80% (equivalent to the H line).

5.2.3 Scanning method

A fatigue crack was generated at the weld root along the weld line in the sleeper direction on the bottom side of the side beam by fatigue test on an actual bogie frame. The probe was placed on the bottom surface of the side beam at a position in the rail direction which was a one-skip distance of ultrasound with a refraction angle of 70° from the weld line. The probe with the encoder scanned the bottom surface along the weld line in the left-right direction (sleeper direction) while fixing the back-forth direction (rail direction) of the probe. Then, the welded part in an approximately 40-mm-length area along the weld line was tested using the single-bounce method. The coordinates output from the encoder in the left-right scanning of the probe were recorded, and cross-sectional images were acquired continuously to build a three-dimensional image of the cross section along the weld line.

5.3 Test results

Figure 10 shows the results of flaw detection on an actual bogie frame. As can be seen from the side view of the sector scan, the image of the flaw echo was displayed by the single-bounce ultrasound in a direction with a refraction angle of approximately 70°. The flaw size was estimated from the size of area where the echo height exceeds 80% in the top view from the bottom of bogie frame and the end view in the thickness direction. The flaw was approximately 8-mm long along the weld line in the sleeper direction. As can be seen from the top view, since the position of the obtained flaw image almost coincided with the targeted weld line (focal position

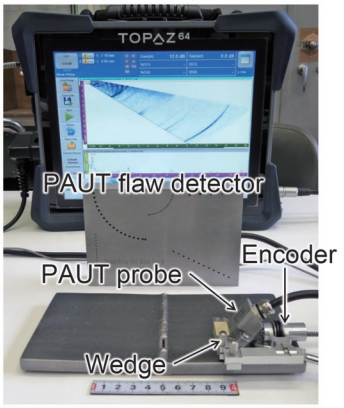

Fig. 9 Configuration of PAUT flaw detector

Table 2 Settings of PAUT flaw detector

Sound velocity	Longitudinal wave: 5920 m/s, Shear wave: 3230 m/s
Scanning mode	Sector scan Shear-wave angle: 40–75°, 0.5° pitch
Sensitivity adjustment	Reflection from the 100-mm-radius surface on the STB-A1 standard block was adjusted to be constant for all refraction angles.
Focus setting	Projection mode: Ultrasonic waves of all refraction angles are focused at the position of one-skip horizontal distance determined by the 70° shear ultrasound.

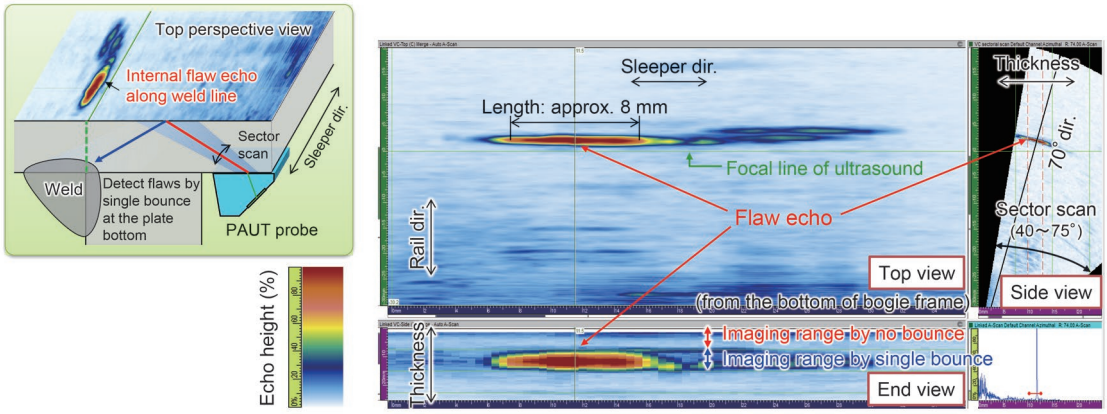

Fig. 10 Visualization of detected flaws along the weld line in a bogie frame by PAUT single-bounce method

of ultrasound), we could easily determine whether the indication was a flaw or not. In addition, it was confirmed that similar flaw echoes were observed when the same location was tested by conventional UT.

As described above, sensitivity adjustment was conducted based on the echo height of ø4 × 4 mm VDH, which ensures compatibility with conventional UT. It was then confirmed that the test results in the welded part of an actual bogie frame by PAUT could be visualized clearly. As a result, the effectiveness of PAUT was demonstrated in the flaw detection of bogie frames.

6. Ultrasonic flaw detection in axles using PAUT

6.1 Overview

For axles on railway vehicles undergoing periodic inspection, ultrasonic testing is applied to detect flaws on surfaces fitted with wheels and gears. Currently, conventional UT is the mainstream application used for ultrasonic axle flaw detection. However, as the results of flaw detection can be visualized using PAUT, it is expected that flaw detection may become easier. This chapter presents the inspection results of wheel seats, etc., of axles, when PAUT was applied to the shear-wave angle-beam and longitudinal-wave angle-beam testing methods.

6.2 Axle test blocks

Figure 11 schematically shows axles with artificial flaws, referred to as model axles. The model axles were intended for driving and trailing axles with a length of 1900 mm used in conventional (other than Shinkansen) cars. Notch-shape (N) flaws with heights of 0.5, 1, 3, 5, and 10 mm were machined by electrical discharge machining (EDM) based on the positions of A to G in each axle. Subsequently, wheels, a gear component, a brake disk component, and bearing inner rings were fitted to the respective seats of each axle. Three bolt holes were machined at intervals of 120° on both axle ends to attach the axle end cap.

6.3 Test method

6.3.1 Shear-wave angle-beam testing

A PAUT probe was attached to the axle body surface of the model trailing axle through a wedge for shear-wave angle-beam testing. A flaw detection test was then conducted using a sector scan with a shear-wave refraction angle of 35° to 75°. The left column of Table 3 lists the equipment used and typical test conditions. Owing to a relatively longer distance to the test zone than that in a bogie frame, a large probe with a 64-element transducer at a frequency of 5 MHz was used. The contact surface of the wedge with the axle was machined with a curvature to fit the diameter of the axle body. After the back-forth (axial) position of the probe was determined, an image of the flaw detection was acquired by left-right (circumferential) scanning of the probe. Figure 12(a) shows the appearance of flaw detection.

6.3.2 Longitudinal-wave angle-beam testing

A PAUT probe was attached to each end face of the model driving axle through a 5-mm-thick wedge with a central pin. The flaw detection test was conducted using a sector scan with a longitudinal-wave refraction angle ranged 0–30°. The right column of Table 3 lists the equipment used and the typical test conditions. A probe with a 64-element transducer at a frequency of 5 MHz was used also in the longitudinal-wave angle-beam testing. In the measurement of flaw echoes, the central pin of the wedge was fitted to the lathe hole on the axle end face. The probe was then rotated clockwise while maintaining a constant distance from the center of the axle to the probe index point. Figure 12(b) shows the appearance of flaw detection.

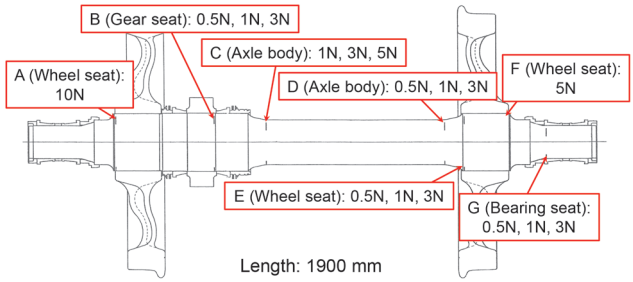

(a) Driving axle

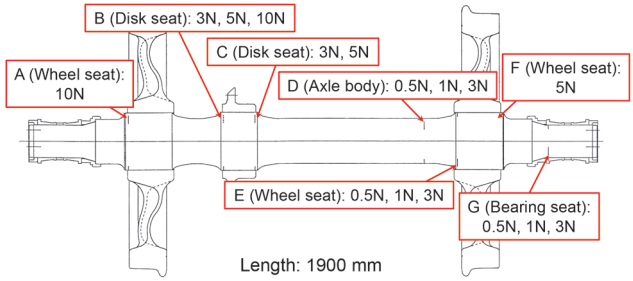

(b) Trailing axle

"N" indicates the flaw type (notch-shape flaw) and the number indicates its height in mm for each flaw at positions A to G.

Fig. 11 Schematic of two types of axles with artificial flaws (model axles)

Table 3 Equipment used and typical test conditions for PAUT axle test

	Shear-wave angle-beam testing	Longitudinal-wave angle-beam testing
Ultrasonic flaw detector	TOPAZ-64/128PR-TFM HR (ZETEC)	
Probe	LM-5MHZ (ZETEC); Frequency: 5 MHz, Number of elements: 64, Transducer size: H 38.4 mm (0.6 mm × 64 elm.) × W 10 mm	
Wedge	LM-55SW (ZETEC) for 55° shear-wave transmission use (machined the contact surface with a radius of 76 mm)	Thickness: 5 mm, Wedge angle: 0° (with a central pin)
Sound velocity setting	Longitudinal wave: 5920 m/s, Shear wave: 3230 m/s	
Scanning mode	Sector scan Shear-wave refraction angle: 35–75°, 1° pitch	Sector scan Longitudinal-wave refraction angle: 0–30°, 0.5° pitch
Sensitivity correction among sector scan angles	Reflection from the 100-mm-radius surface on the STB-A1 standard block was adjusted to be constant for all refraction angles.	Reflection from the 210-mm-radius surface on the L-wave index point measurement test block was adjusted to be constant for all refraction angles.
Focus setting	None	None
Scanned surface	The surface of the axle body	Axle end faces on both sides

6.4 Test results

6.4.1 Shear-wave angle-beam testing

The 1N flaw at position E (wheel seat) has been targeted for detection by ultrasonic testing of axles. Figure 13 shows the result of the shear-wave angle-beam testing of this flaw with the wheels fitted, which was obtained by the PAUT probe in contact with the axle body surface of the model trailing axle. The 1N flaw echo was detected at its relevant position with a sufficient signal-to-noise ratio, along with the echo due to the axle surface shape at the outer edge of the wheel seat appearing around the entire circumference. Since the flaw detection results are displayed as an image, we could easily determine if the echo is due to a flaw by comparing it with the drawing of the axle. Although not shown, it was also possible to detect a 0.5N flaw on the wheel seat.

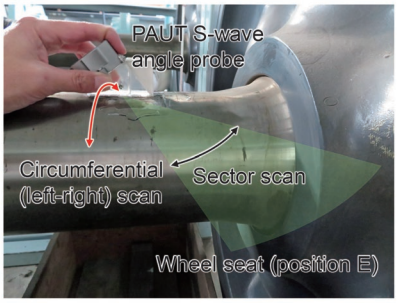

(a) Shear-weve angle-beam testing of a model trailing axle

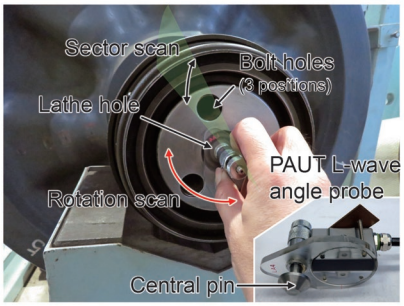

(b) Longitudinal-weve angle-beam testing of a model driving axle

Fig. 12 Ultrasonic testing of model axles using a PAUT probe for each testing method

6.4.2 Longitudinal-wave angle-beam testing

Figure 14 shows the results of longitudinal-wave angle-beam testing over the entire circumference of the model driving axle including the 1N flaw at position E (wheel seat) with the wheels fitted. They were obtained by the PAUT probe in contact with the counter-gear-side axle end face. The flaw detection results are shown with the axle drawing in Fig. 11(a) reversed horizontally. Ultrasonic waves could not be sufficiently transmitted and received when the longitudinal-wave angle probe passed over the three bolt holes on the axle end face. These were displayed as three blank lines in the top view of the inspection results. Relatively large noise signals were observed around the backing ring of the axle bearing and the part fitted with the wheel. However, flaws of 0.5, 1, and 3N at each position D (axle body), E (wheel seat), and G (bearing seat) were detected and visualized.

7. Conclusions

In this report, ultrasonic imaging technology using PAUT with an array probe was applied to welds of bogie frames and fitted parts such as wheel seats of axles, and the visualization and detection of flaws were experimented. The obtained results are as follows:

(1) When PAUT was applied to the flaws inclined against the surface of bogie frames, the echo height was higher than that in conventional UT, demonstrating the superiority of PAUT in detecting inclined surface flaws.

(2) The influence of paint thickness on the surface of bogie frames on the echo height in PAUT was evaluated. The influence changed according to the refraction angle. However, within the range of paint thickness up to approximately 1 mm, the echo height reduction was within 20% in all cases of refraction angle.

(3) PAUT was applied to an actual bogie frame and its flaw detection capability was tested. After conducting sensitivity adjustment based on the echo height of ø4 × 4 mm VDH, which ensures compatibility with conventional UT, the test results could be visualized clearly. Therefore, the effectiveness of PAUT was demonstrated in the flaw detection of bogie frames.

(4) In the ultrasonic flaw detection of axles, PAUT was applied to the shear-wave angle-beam and longitudinal-wave angle-beam testing methods. It was demonstrated that a notch-shape flaw with a height of 1 mm (1N flaw) at the wheel seat with the wheels fitted could be detected and visualized by both methods.

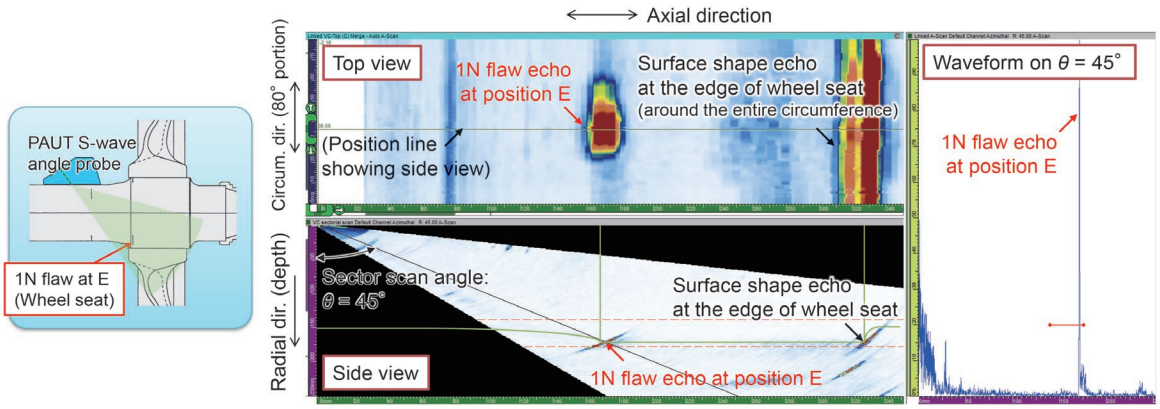

Fig. 13 Flaw detection result by shear-wave angle-beam PAUT at position E (inner boss end of wheel seat) of model trailing axle

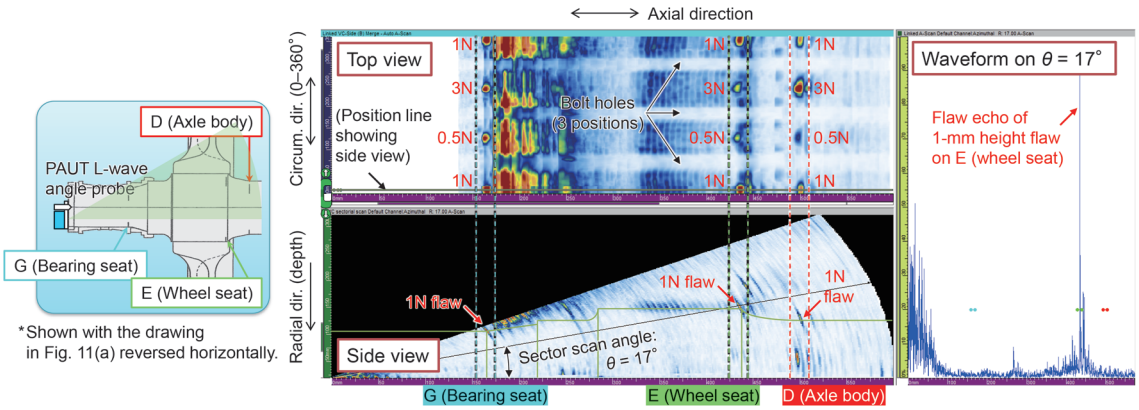

Fig. 14 Flaw detection results by longitudinal-wave angle-beam PAUT from the counter-gear-side end face of the model driving axle

By applying PAUT to the flaw detection of bogie parts, flaws in welds of bogie frames and those on wheel seats of axles with the wheels fitted can be detected as images, which is challenging to achieve using conventional UT. This prevents flaw detection failure in bogie parts and contributes to the further improvement in bogie safety.

References

[1] Ishiduka, H., "Probability of improvement in routine inspection work of Shinkansen vehicle axles," *Quarterly Report of RTRI*, Vol. 40, No. 2, pp. 70–73, 1999.

[2] Japan Transport Safety Board, *Railway Serious Incident Investigation Report*, RI2019-1-1, 2019.

[3] Japan Transport Safety Board, *Railway Accident Investigation Report*, RA2018-1-1, 2018.

[4] Olympus NDT, *Introduction to Phased Array Ultrasonic Technology Application*, Olympus NDT, 2006.

[5] JIS Z 3060:2015, "Method for ultrasonic testing for welds of ferritic steel," Annex B (normative): Examination method for flat plate joint welds.

[6] ITOCHU Techno-Solutions Corporation (CTC), "engineering-eye: Ultrasonic/Electromagnetic Wave: ComWAVE," https://www.engineering-eye.com/en/category/e14/ComWAVE/index.html, accessed on Sep 15, 2023.

[7] K. Ono, "A comprehensive report on ultrasonic attenuation of engineering materials, including metals, ceramics, polymers, fiber-reinforced composites, wood, and rocks," *Appl. Sci.* 10(7), 2230, 2020.

[8] JIS Z 2345-1:2018, "Standard test blocks for ultrasonic testing — Part 1: A1 Standard Test Block," 5.2 Shape and dimensions, Fig. 1.

Author

Kazunari MAKINO, Ph. D. (Eng.)
Chief Researcher, Vehicle & Bogie Parts Strength Laboratory, Vehicle Technology Division
Research Areas: Nondestructive Testing of Bogie Parts, Axle Strength

Adhesion Increase Method for Shinkansen Train under Snowfall in Winter

Shinichi SAGA
Braking Systems Laboratory, Vehicle Technology Division

Hua CHEN
Railway International Standards Center (Former Track Dynamics Laboratory, Railway Dynamics Division)

Junji MATSUNO
Ueda Brake Co., Ltd.

When railway vehicles running in snowy weather, the adhesive force between rails and wheels is lower than that in rainy weather. For this reason, we studied a method to increase the adhesion coefficient focusing on the temperature and the roughness of wheel treads. From the viewpoint of minimizing specification changes, improving the material of current abrasive block through full-scale dynamo bench test, we developed new abrasive block. An optimal wheel tread cleaner device operating pattern was found through running tests using an actual vehicle in winter. The execution of the pattern contributes to improving adhesive effect such as increasing roughness of wheel treads, and suppressing slipping in the high-speed range, in addition to reducing temperature rise and improving wear resistance.

***Key words*:** *Shinkansen train, low temperature snowfall, adhesion, tread cleaner device, abrasive block, wheel tread roughness, operating pattern*

1. Introduction

As Shinkansen train running speeds increase, the stopping distances must be shortened commensurately. The braking force for decelerating a vehicle is supplied by the mechanical braking device (disk, caliper, pad) mounted on the bogie, but as a fundamental principle, braking depends on the adhesion force (in the longitudinal direction of the wheels) acting between the rails and the wheels, and this is called the adhesion method.

With regards to adhesion force behavior between the rails and wheels, compared to dry conditions, the adhesion force in rainy weather is known to decrease [1]. Therefore, braking force and control are usually designed on the safe side considering these decreasing adhesion characteristics (henceforth, "adhesion formula of wet condition"): however, further increases in the adhesive force acting between the rails and wheels would enable improvement of the performance of the mechanical braking device.

The ceramic injection method [2], which is already in use, is designed to increase adhesion by supplying hard particles between the rails and wheels. The device is installed on one or two axles on a trainset: it has been reported that the adhesion effect is exhibited up to about the third car in wet conditions (simulated rainy weather), and its effect has also been confirmed in a running test on an actual vehicle [3].

On the other hand, Japan's Joetsu Shinkansen line, which receives large amounts of snowfall, was installed with a sprinkler system snow melting device [4], after examining weather conditions and water intake conditions, in order to deal with the various snow problems, with a view to suppressing low adhesion by changing the environmental conditions from icy and snowy to wet. Nevertheless, for projected Shinkansen lines which are not installed with sprinkler system snow melting devices (snow-storing track) and trains which will be running at high speeds not only in icy/snowy conditions but also in areas seeing heavier snowfall than ever before, there are greater concerns regarding low adhesion.

There is already a body of knowledge regarding the use of snow tires and stud-less tires that have special tread patterns [5] for automobiles in icy and snowy (freezing) road conditions. However, opting to change wheels on railway vehicles would not be easy and it is not possible to form tread patterns on a wheel tread like on a road vehicle tire. Furthermore, while some studies have been carried out under limited conditions [6], knowledge about running in icy/snowy rail conditions is scarce both in Japan and overseas.

This paper therefore aims to examine countermeasures against low adhesion under icy/snowy rail conditions (under a snowfall environment), by experimentally investigating the characteristics of adhesion between rails and wheels at low temperatures and developing a new method to increase adhesion in these conditions.

2. Two-cylinder adhesion bench test

We used a wheel-rail high-speed contact fatigue tester to conduct a two-cylinder adhesion bench test that simulates a snowfall environment. Table 1 summarizes the various conditions.

Figure 1 shows the test setup and results. The adhesion formula of wet condition is given by $\mu=13.6/(V+85)$, where V (km/h) is the speed, and this corresponds to a 7-notch service brake ("B7N"). Additionally, the figure also shows the results for each test condition (A–D) and approximation curves that were obtained in the form of $\mu=b/(V+a)$ using the least-squares method.

As the speed increases, the approximation curve shows tendency for the adhesion coefficient to decrease in the order of A>wet>B≥C>D. B and C asymptotically approach the 6-notch service brake ("B6N"), and D asymptotically approaches the 4-notch service brake ("B4N") at high speed. It is speculated that the reduction rates with respect to B7N are approximately 10% for the former (B, C) and approximately 40% for the latter (D), suggesting that adhesion may be lower under icy/snowy rail conditions than under wet rail conditions.

Based on the above, this study investigates a method for increasing adhesion for each wheel with a focus on wheel tread tem-

perature and roughness, which are known as factors that contribute to adhesion [7, 8]. The aim is to enhance the functions of the tread cleaner device and abrasive block ("current use") shown in Fig. 2 as well as improving adhesion performance between rails and wheels in a snowy winter environment.

3. Wheel tread temperature simulation

The purpose of the ceramic injector and abrasive block are to increase wheel tread ("tread") roughness, not to increase the temperature of the tread, however there are various risks due to increases in temperature.

The rim of Shinkansen train wheels are heat treated during manufacturing as a measure against breakage, and the residual stress (200 MPa) in the circumferential direction of the rim is specified.

Table 1 Temperature and intercalary conditions

	A	B	C	D
Rail	20–25°C	←	←	←
Wheel	20–25°C	←	←	<−10°C
Intercalary	Water 25°C 0.4 ℓ/min	Water 5°C 0.4 ℓ/min	Ice and water	Ice and water

*Ice and water: water (5°C, 1.0 ℓ/min) + ice shavings (2 kg/min, 320 kg/cm^3)

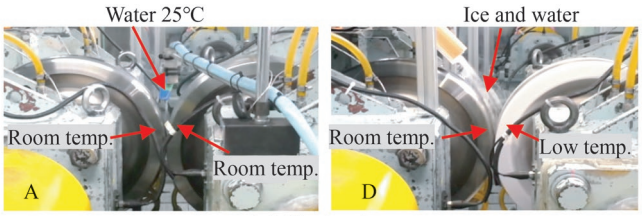

(a) Test setup

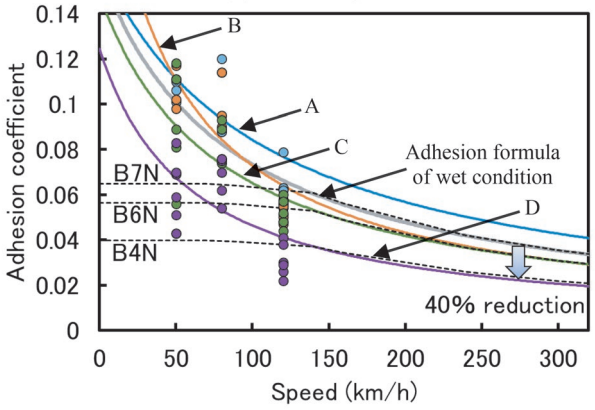

(b) Adhesion coefficient and approximation curve results

Fig. 1 Test setup and results

Fig. 2 Tread cleaner device and abrasive block

Additionally, maintaining the tread shape during high-speed running was an essential feature when developing the 0 series Shinkansen train, so this series has a disk brake system which prevents excessive frictional heat transferring to the tread.

To achieve higher levels of adhesion requires development of a new abrasive block that suppresses rises in tread temperature as much as possible while increasing tread roughness. Therefore, we conducted a simulation on the tread temperature and the stress in the circumferential direction of the rim.

NASTRAN was used as the solver, and the elastic region was analyzed under the conditions described below. For a tread model expressed in two dimensions, three types of input heat ranges (17.5, 35, 70 mm) and the following three input heat patterns were set:

(1): Tread heat input
(2): Tread heat input + wheel plate section 100°C (assumed to be after pneumatic emergency brake)
(3): Tread heat input + wheel load 60 kN + lateral force 48 kN (assuming derailment coefficient of 0.8)

The maximum tread temperatures when the stress in the circumferential direction of the rim changed by 1, 50, and 100 MPa, respectively, were calculated under the condition where the input heat amount reached the maximum value one second after the start of braking and was changed linearly so that it became 0 W/mm^2 in 200 seconds afterwards.

Figure 3 shows the results of the analysis. In the case of heat input pattern (1), the maximum tread temperature when the stress increased by 100 MPa under the 17.5 mm condition was estimated to be 750°C. The maximum tread temperature when the stress increased by 50 MPa under the 35 mm condition was estimated to be 860°C, and this was the condition where the stress was smallest. The maximum tread temperature when the stress increased by 100 MPa under the 70 mm condition was estimated to be 410°C.

In the case of heat input pattern (2), the maximum tread temperature when the stress increased by 100 MPa under the 17.5 mm condition was estimated to be 98°C. The maximum tread temperature when the stress increased by 20 MPa under the 35 mm condition was estimated to be 863°C, and this was the condition where the stress was smallest. The maximum tread temperature when the stress increased by 100 MPa under the 70 mm condition was estimated to be 474°C.

In the case of heat input pattern (3), the maximum tread temperature when the stress increased by 100 MPa under the 17.5 mm condition was estimated to be 756°C. The maximum tread temperature when the stress increased by 100 MPa under the 70 mm condition was estimated to be 412°C. The temperature exceeded 1,000°C under the 35 mm condition, so this was excluded.

Next, we conducted a bench test in order to determine the upper limit of circumferential stress. The bench test was carried out by

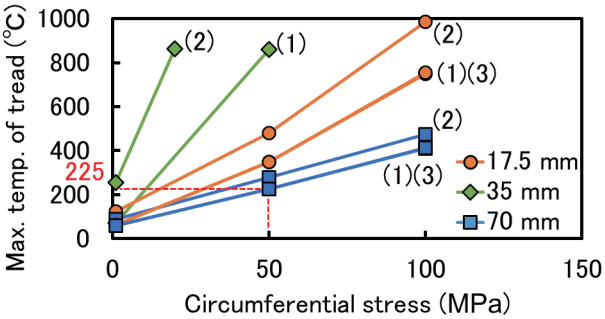

Fig. 3 Analysis results

pneumatic emergency braking with the abrasive block inactive. When assuming that the upper limit value is 50 MPa from the trends in the amount of change during braking and also assuming that the heat input range is 70 mm as the condition for the lowest tread temperature, it was shown that the tread temperature must be kept below a maximum of 225°C, and this was used as the reference value for the tread temperature increase.

4. Development of cast iron block

4.1 Evaluation by bench test

We prototyped cast iron and sintered alloy blocks, and we compared them with a current block (composite) by conducting bench tests using a full-scale wheel (high-speed sliding test, adhesion test at 100 km/h). Figure 4 shows the results of evaluating temperature, tread roughness, and circumferential stress under five initial speed (260, 300, 320, 360, 400 km/h) and two pressing force (750, 1,500 N, current block is 500 N) conditions.

The symbols in the figure (◎, ○, △, ×) represent the test results for levels of convenience, with each representing excellent, good, acceptable, and unacceptable, respectively. We focus on the change in maximum tread temperature, tread roughness, and stress among the evaluation items, and we selected the 750 N of the superior cast iron block ("block A"). The adhesion coefficients using the two-cylinder rolling tester at 100 km/h were 0.14 for the current block and approximately 1.1 times that value, or 0.15, for the block A.

Obtaining a pressing force of 1,500 N requires a new tread cleaner device, which inevitably leads to an increase in weight (9.4 kg compared to the current 7.9 kg). Meanwhile, in the case of approximately 700 N, only a minor change of just adjusting the pressure of the tread cleaner device is needed, and this is easy to install. Therefore, we decided to proceed with development on the assumption that it would be used in combination with the tread cleaner device currently in use.

4.2 Evaluation by running test (no snowy season)

The maximum speed of the adhesion bench test using the two-cylinder rolling tester was about 100 km/h, so evaluating the adhesion characteristic of a Shinkansen train with a speed that exceeds 200 km/h requires conducting a running test that uses an actual vehicle. Therefore, we conducted a running test outside the no snowy season with test block mounted on four wheels of one bogie of the middle car of the test train set. The order of the test was 'current block' and 'block A'.

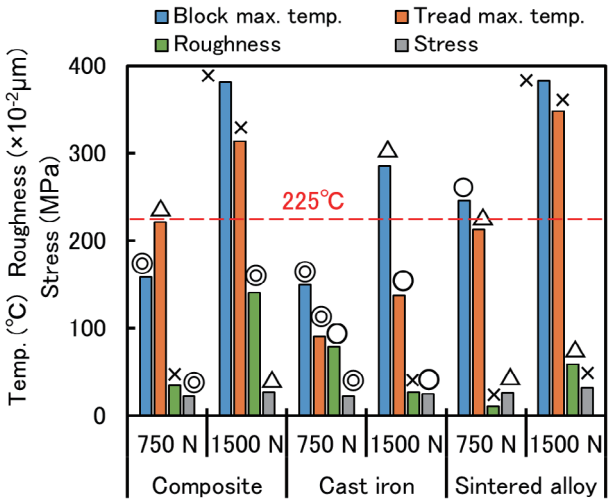

Fig. 4 Comparison results of full-scale bench test

Investigating the adhesion characteristics requires artificially creating low-adhesion conditions between the rails and wheels. Therefore, using research by Chen et al. [8] as a reference, we sprayed water (5°C, 5 ℓ/min/wheel) on one axle as a method for generating frequent large slipping. Furthermore, we proposed a new method for pre-calibrating the relationship between the strain value and torque generated in the caliper bracket using bench test as a method for obtaining an accurate pneumatic braking force (friction force).

The operation of the tread cleaner device was conducted by an external controller, and the control law was the current specification. Thermocouples were embedded at the top and bottom of the test block, and an ultra-compact thermal camera system [9] that could be mounted on the bogie was used to observe the temperature distribution of the tread, which rotates at high speed.

Conventional adhesion tests repeatedly apply a sawtooth wave-like pressure to the brake cylinder of the evaluated axle, while the train is coasting to force it to slip. However, this conventional method is no longer compatible with current vehicle systems and cannot be applied. Therefore, in this test, the braking force of the evaluated car was set high, and the emergency brake was applied. Additionally, deceleration braking (without ceramic injection) was conducted from the initial speed of 260 km/h to 230 km/h. The pressure control valve of the tread cleaner device was set so that the pressing force was 500 N and 700 N.

4.3 Test results

The slipping occurrence rate of the first axle was almost 100% in all conditions. The second axle had a slipping rate of 70–100% for the current block and 0% for block A, with similar trends for the rate of operation of the exhaust valve that loosens the braking force for each trial, so the average braking force of block A was approximately 1.1 times that of the current block.

A comparison of the adhesion coefficient at the lower limit value at speeds of at least 250 km/h on the first axle showed the order of block A (500 N) ≒ block A (700 N) > current block (700 N) ≒ current block (500 N), and the increased adhesion effect of block A was evident.

The tread roughness of the 700 N of block A was the largest at 0.73 μm on average and approximately 1.3 times that of the current block, but there was the concern of not only not reaching the target roughness of 1.0 μm when using ceramic injection, but also about rolling noise due to convex roughness of the cast iron. There were also problems due to the metal material, such as the maximum temperature of the second axle, which did not slip, exceeding 100°C. The tread temperature was approximately 40°C, which was below the reference value.

5. Development of composite block

5.1 Evaluation by bench test

To solve the problems found with block A, namely, capacity to generate tread roughness, noise concerns, and rising block temperature, we proceeded with the development of a composite block

("block B") based on the following concepts:

(1) Strength, capacity to generate tread roughness, composition of scoring iron, and composition of molding conform to current block;

(2) Increase in filling ratio of hard metal, adjustment in amount of resin in binder. Promotion of activation of sliding surface, improved capacity to generate tread roughness;

(3) Improvement of draining performance and adhesion effect due to temperature increase. Improvement of thermal conductivity with metal and fiber materials;

(4) Lighter than block A (2.8 kg), similar to current block.

A comparative evaluation was conducted using a high-speed sliding test, adhesion test, and noise test that simulated a realistic run curve using regenerative braking. The test conditions are given below:

- High-speed sliding test: three times for each condition
  Speed: 300 → 30 km/h, pressing force: 700 N
- Adhesion test (same as Section 4.1): three times for each condition
  Speed: 100 km/h, pressing force: 700 N
- Noise test: forward/reverse rotation only once
  Speed: 260, 360, 400 → 70 km/h, pressing force: 700 N

Figure 5 shows the results of the high-speed sliding test and adhesion test, and Fig. 6 shows the results of the noise test. The block B had block temperature and tread temperature suppressed to approximately 1.4 times and approximately 1.1 times those of the current block, respectively, and had similar value to those of block A. Furthermore, the tread roughness and adhesion coefficient increased to approximately 1.7 times and approximately 1.4 times, respectively, and a high adhesion effect is expected.

The noise was measured at a position 1,500 mm away from the block. The block B was at the same level or lower than the current block and was confirmed to be significantly lower than that of block A.

5.2 Evaluation by running test (snowy season)

In the running test, which evaluates the adhesion performance, the weather during the test period is not necessarily snowy, so artificial water spraying was conducted outside snowy season. This is why there is little knowledge related to adhesion characteristics in winter.

Therefore, in this study, we decided to evaluate the performance when running in a natural snowfall environment. The content of the test was generally the same as the running test conducted in Section 4. However, the low-temperature water spray was set at 5°C and 2 ℓ/min/wheel, and a train stop braking test was conducted. The main conditions were as follows:

- Initial speed: 160, 260, 275, 320 km/h
- Notch: emergency brake, 7-notch service brake
- Pressing force: 500 N, 700 N
- Ceramic injection: none

The results of the test were as follows. Block B tended to have a significantly lower number of slip than the current block, with the 700 N being superior. For the tread roughness, there was no difference according to differences in the pressing force for the current block. Meanwhile, the 700 N was the largest for the block B, with a value approximately 1.4 times that of the current block on average, at 0.83 µm, which was close to the target 1.0 µm.

Figure 7 shows an example of the observation results of the tread temperature distribution using an ultra-compact thermal camera system. In each case, the sliding width (heat-generating part) near the rolling part tended to be wider at 700 N than at 500 N, and

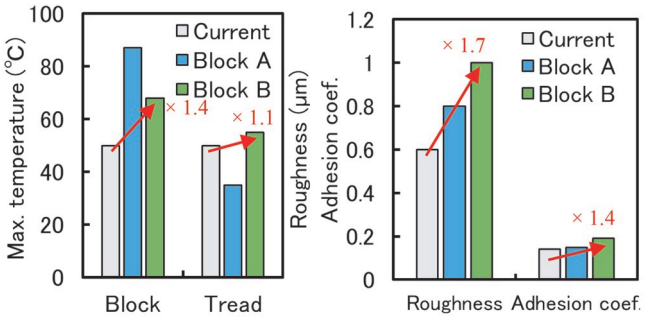

Fig. 5 High-speed sliding test and adhesion test results

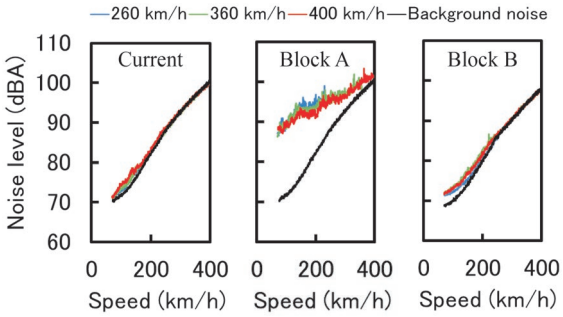

Fig. 6 Noise test results

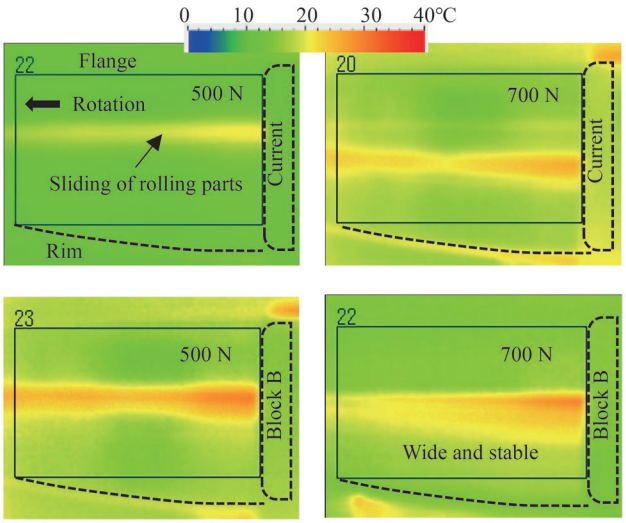

Fig. 7 Observation result of tread temp. (at 300 km/h)

the 700 N of the widest block B was thought to have effectively generated roughness in the rolling part. The tread temperature was approximately 30°C due to the effects of the ice and snow as well as the external air temperature, and the thermal effect on the tread and wheel stress were thought to be small.

This test was a train stop brake, and compared to the adhesion test, which repeats short decelerations, the operation time of the tread cleaner device is longer, and the ATC (Automatic Train Control) brake also works to raise the base temperature of the block. Even when considering these effects, block B exhibited a higher temperature than the current block. Although a significant temperature increase contributes to increased adhesion, there is a concern about the deterioration of wear resistance.

The operation logic of the tread cleaner device is to start (inter-

mittent) operation upon receiving a brake command (all notches) while running above a certain speed ("current pattern"). Therefore, we analyzed the notch frequency of ATC brakes and studied the following notch limits as measures for reducing the wear amount.

・Start operation at B4N or higher ("B4N limit")
・Start operation at B6N or higher ("B6N limit")

Due to the notch limit, the operation time decreased by approximately 10% for the B4N limit and approximately 30% for the B6N limit compared to the current pattern, but the wear amount was about 10 times for the B4N limit and about 4 times for the B6N compared to the current block. Therefore, the 700 N of block B requires a thorough review of its tread cleaner device operating pattern.

5.3 Bench test for wear resistance

Figure 8 shows a diagram of the operating pattern. The current pattern intermittently alternates 'contact and release' in conjunction with the brake command (all notches), and different time parameters are set for each preset speed band. For example, at speeds V1–V2 of the current pattern, intermittent operation is conducted by a combination of ON time T1 and OFF time T2. Therefore, when decelerating across speed bands, two adjacent settings may operate continuously, which results in the operation time becoming longer and affecting wear.

Therefore, as a countermeasure pattern, the speed V3 on the high-speed side was abolished, and the speed bands were split between those for the conventional lines and for the Shinkansen lines. Additionally, a limit up to B6N (operating at B6N or less) was set on the low-speed side with the assumption of entering a station with ATC brakes, and a B7N (operating at B7N or more) was set on the high-speed side with the assumption of insufficient adhesion.

Next, the change in sliding torque was used to determine the boundary between the roughness generation phase (maintaining high torque) and wear phase (sharp decrease in torque) and to find the minimum contacting time T6 for roughness generation, and countermeasure pattern (1) was formulated based on this. The ON times of countermeasure pattern (2) and countermeasure pattern (3) were each approximately 2 and 3 times that of countermeasure pattern (1), respectively. Countermeasure pattern (1) had the shortest overall operation time, and the current pattern had the longest.

Under the conditions shown below, a bench test was conducted using a full-scale wheel, and the levels of tread roughness and wear were compared and evaluated.

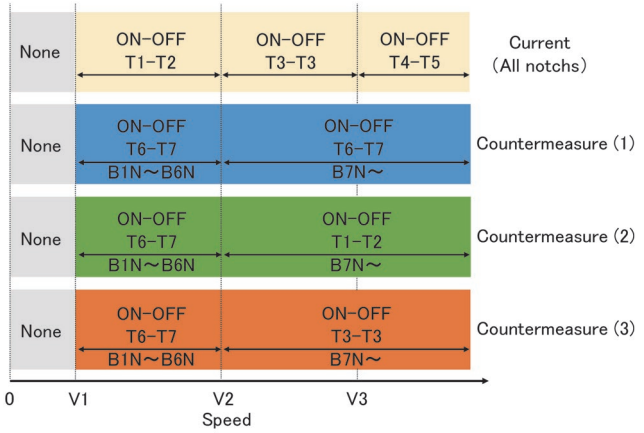

Fig. 8 Diagram of operating pattern

・High-speed sliding test: 10 times each
Speed: 260 → 70 km/h, 360 → 70 km/h
Pressing force: 500 N (current block), 700 N (block B)
Operating pattern: Current pattern
Countermeasure pattern (1)-(3)

The results of the test were as follows. Each pattern maintained a tread roughness of at least 1.2 times more than that of the current pattern. The wear amount increased as the operation time increased and was approximately 2 times for countermeasure pattern (1), approximately 4 times for countermeasure pattern (2), and approximately 6 times for countermeasure pattern (3).

5.4 Verification of countermeasures (snowy season)

We conducted a running test in a natural snowfall environment in order to evaluate the wear countermeasure effect and adhesion performance. The test provisional structure is basically the same as the content implemented in Section 5.2, but the evaluation by bogie unit so far has a different test period for each test model, and strictly speaking, the weather and environmental conditions were not the same.

Therefore, in this running test, we mounted the current block (pressing force: 500 N, current pattern) on one axle and the block B (pressing force: 700 N, countermeasure pattern (1) → countermeasure pattern (2) → countermeasure pattern (3)) on the other axle, and we evaluated both at the same time. Additionally, we decided not to use low-temperature water spraying because the temperature is higher than the ice and snow, and it may suppress the effect of low adhesion. Therefore, we attached a special camera that observes the rail/wheel to the bogie in order to determine the running environment.

Figure 9 shows an example of an image captured by the observation camera while running. It can be seen from the video that the snow and ice have collected forming a dense pack. In other words, a large quantity of ice and snow is supplied and interposed between the rails and the wheels, resulting in a low-adhesion state. The current block tends to exhibit relatively frequent slipping and skidding.

The block B has a stronger re-adhesion tendency than the current block for all patterns, and the slipping occurrence was suppressed by approximately 15–20%.

Figure 10 shows the adhesion coefficient results. Due to space limitations, this paper only describes countermeasure pattern (2), and only the results of the other countermeasure patterns are mentioned. Under a natural snowfall environment, it was found that there were cases where the adhesion tended to be lower than the adhesion formula of wet condition (snow-storing section, external air temperature about −8°C, 20% lower than adhesion formula of wet condition). A comparison with the approximation curves showed that countermeasure pattern (1) and countermeasure pattern (2) were almost the same as the current pattern. For countermeasure

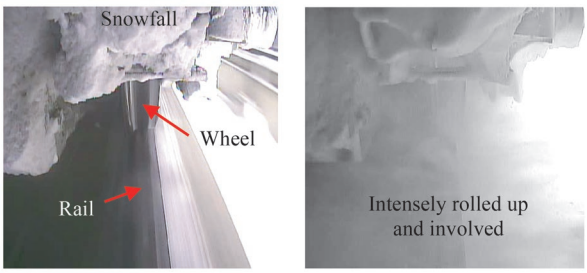

Fig. 9 Rail and wheel when running (at 220 km/h)

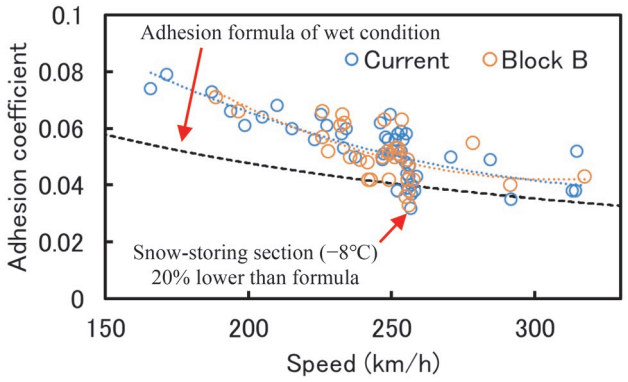

Fig. 10 Adhesion coefficient result (pattern (2))

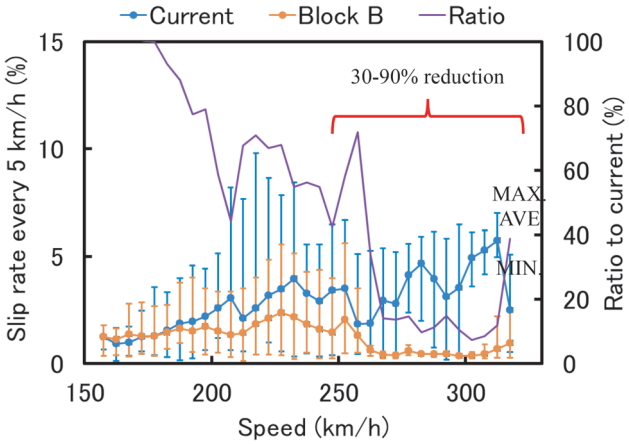

Fig. 11 Slip rate result (pattern (2))

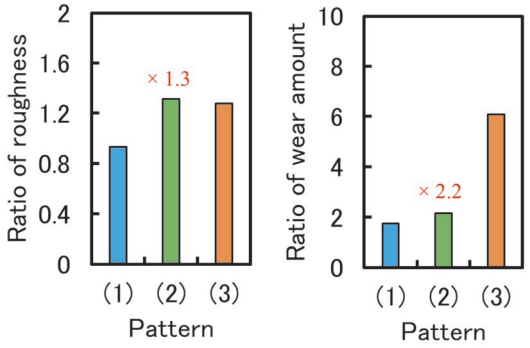

Fig. 12 Tread roughness and wear amount results

pattern (3), block B was slightly superior.

However, as mentioned above, the adhesion coefficient was a set of point data at the start of slipping. In other words, it represents a momentary phenomenon at a single point, and it does not necessarily represent a continuous adhesion phenomenon that changes dynamically. Therefore, we conducted an evaluation with a focus on the slip rate, which is expressed as the ratio of each axle speed to the train speed.

Figure 11 shows the results of countermeasure pattern (2), in which the slip rate is averaged for every 5 km/h speed. Looking at the ratio of the block B to the current block, countermeasure pattern (1) showed a reduction of approximately 30–70%, countermeasure pattern (2) showed a reduction of approximately 30–90%, and countermeasure pattern (3) showed a reduction of approximately 40–80%, and each pattern showed a slipping suppression effect due to block B. Particularly for the high-speed range, the effect tended to be higher for longer operation times. In this way, suppressing the slip rate can reduce the frequency of slipping detection in wheel slide re-adhesion control, suppress the reduction in braking force due to the subsequent loosening operation, and contribute to shortened stopping distance (i.e., higher deceleration).

Figure 12 shows the results of the tread roughness and wear amount compared to the current block. The tread roughness of countermeasure pattern (2) was approximately 1.3 times that of the current block, and it is thought that it could adhere even under icy and snowy conditions. Additionally, the wear amount was approximately 2.2 times larger, which was generally in agreement with the results of the bench test. The block temperature tended to increase as the operation time increased with block B, and countermeasure pattern (3) in particular is thought to have had a direct impact on the wear amount. Meanwhile, the tread temperature showed similar values in both cases, so the thermal effect on the tread and wheel-stress is thought to be small.

Based on the above results, it is thought that countermeasure pattern (2) supplies both functions of adhesion effect and wear resistance.

6. Conclusion

In this study, we developed an easy-to-install composite block with increased adhesion performance under icy and snowy rail conditions (i.e., snowing conditions), where there is a concern that adhesion would be lower than under wet rail conditions. We also proposed a tread cleaner device operating pattern that has both an adhesion effect and wear resistance. In the future, the tread cleaner device control specifications will be adjusted according to the line section and time of year, and countermeasure pattern (2) will be set for lines with heavy snowfall and its periods, and an even shorter operating pattern will be set for all others, which is expected to even out the wear amount and allow for year-round use.

Acknowledgment

We have received major cooperation in the implementation of the running test from associates including Kenichi Kitamura, Shinpei Fujita, and Hiroto Morihiro of the East Japan Railway Company; and Takuya Yamaguchi of the West Japan Railway Company. We would like to take this opportunity to express our sincere gratitude to these individuals.

References

[1] Ohyama, T., *A story about adhesion - Adhesion between wheels and rails and its effective use* -, Rail and Tech Publishing, 2002 (in Japanese).

[2] Ohno, K., "Adhesive injection device (Cerajet) -Part 1-," *RRR*, Vol. 63, No. 1, pp. 36-37, 2006 (in Japanese).

[3] Saga, S., Miyabe, M., Kawamura, J., Sugita, H., and Chikuma, K., "An Evaluation Method of the Braking Performance Using Bogie Traction Force," *Quarterly Report of RTRI*, Vol. 56, No. 4, pp. 256-261, 2015.

[4] Edited by Mochizuki, A., *Technical history of Shinkansen*

trains, Japan Railway Vehicle and Mechanical Engineering Association, 2014 (in Japanese).
[5] Sakai, H., *Tire Engineering*, Grand Prix Publishing, 2002 (in Japanese).
[6] Chen, H., Ido, T., "Adhesion Test of Wheel/Rail under Low Temperature Conditions," *RTRI Report*, Vol. 35, No. 9, pp. 23-28, 2021 (in Japanese).
[7] Ohyama, T., "Abrasive block," *RRR*, Vol. 64, No. 5, pp.38-39, 2007 (in Japanese).
[8] Chen, H., Ban, T., Ishida, M., and Nakahara, T., "Influence Factors on Adhesion between Wheel and Rail under Wet Conditions," *Quarterly Report of RTRI*, Vol. 53, No. 4, pp. 223-230, 2012.
[9] Saga, S., Ikeuchi, K., Ishizaka, K., Handa, K. et al., "Evaluation method of wheel temperature in running railway vehicles," *28th Railway Technology Union Symposium (J-RAIL2021) Collected lecture papers*, No. SS1-4-3, 2021 (in Japanese).

Authors

Shinichi SAGA
Senior Researcher, Braking Systems Laboratory, Vehicle Technology Division
Research Areas: Adhesion, Tribology, Brake Mechanism and Controls

Hua CHEN, Ph.D.
Senior Chief Manager, Railway International Standards Center (Former Head of Track Dynamics Laboratory, Railway Dynamics Division)
Research Areas: Adhesion, Tribology, Track Dynamics, International Standards

Junji MATSUNO
Chief Executive, Ueda Brake Co., Ltd.
Research Areas: Brake Shoe, Abrasive Block

Development and Construction of Soil Reinforcement Method Using Pressurized Injection Materials

Yuki KURAKAMI **Susumu NAKAJIMA**
Foundation & Geotechnical Engineering Laboratory, Structure Technology Division

Masaaki BEPPU
RAITO KOGYO CO., LTD.

Sumio YAZAKI
Integrated Geotechnology Institute Limited

The authors previously developed and proposed a new method called "Lotus anchor" method as a soil reinforcement method. "Lotus Anchor" developed as a soil reinforcement method is a method that obtains high pullout resistance by expanding the reinforcement material using pressurized injection. This paper reports on construction tests conducted during the development process of this method, evaluation of pullout resistance characteristics, examples of subsequent construction, and construction management methods aimed at further improving the efficiency and quality of this method.

***Key words*:** *soil reinforcement, pressurized injection, reinforcement material, pullout test, Lotus anchor*

1. Introduction

The authors developed the "Lotus Anchor Method" (hereafter the "Lotus Anchor") [1] as a pressure injection type soil reinforcement method in 2013. Since then, this method has been used mainly to reinforce old-style retaining walls, embankments, and cuttings, in narrow areas.

The soil reinforcement method is a technology that stabilizes the ground by placing rod-shaped reinforcement materials inside natural slopes, cuttings, and embankments. Figure 1 shows the basic structure of the soil reinforcement method. The reinforcement material consists of a core material and a grout. The general construction procedure for new construction is to bore into ground, insert a rod-shaped tensile core material into the center of the boring, and inject the grout. When excavating the ground, the ground is stabilized by covering the surface with a concrete wall etc., and connecting the reinforcement material and the surface material with a head fixing material.

As a mechanism of soil reinforcement resistance, the surface friction force of the reinforcement which was constructed in the ground is applied as resistance to the structure. Therefore, the thicker and longer the ground reinforcement, the greater the expected resistance. As described later in Chapter 2, soil reinforcement materials are classified according to the diameter of the reinforcement material as shown in Table 1. There are several types of soil reinforcement material. In conventional methods, the grout is generally injected without pressure, so that the boring diameter needs to be the same as the reinforcement diameter.

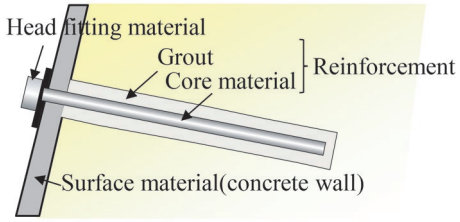

Fig. 1 The basic structure of the reinforcement

In recent years, soil reinforcement methods have also been applied to the reinforcement of existing structures such as retaining walls and bridge abutments. Reinforcement construction for existing structures is subject to spatial and temporal constraints, such as the construction often being done adjacent to operating railway lines in narrow spaces in urban areas. As a result, there are several issues to be solved in terms of construction, such as increased construction costs and longer construction periods.

In order to solve the problems of the conventional method (non-pressure injection), the "Lotus Anchor" developed by the authors as a soil reinforcement method is a method that obtains high pullout resistance by expanding the reinforcement material using pressurized injection. This paper reports on construction tests conducted during the development process, evaluation of pullout resistance characteristics, examples of subsequent construction, and

Table 1 Classification of soil reinforcement method

Classified	Method	Boring			Injection	
		Boring method	Boring diameter(mm)	Reinforcement diameter (mm)	Grout	Injection method
Nailing	Rock bolt	General boring machine	φ 40 to 90	φ 40 to 90	Cement milk	Non-pressure
Micro-piling	Carrot anchor method	Rotary percussion method	φ 170	φ 170		
	Lotus anchor		φ 115	φ 170, φ 230		Pressure
Dowelling	Radish anchor method	Stirring and mixing	φ 300 to 500	φ 300 to 500		Non-pressure

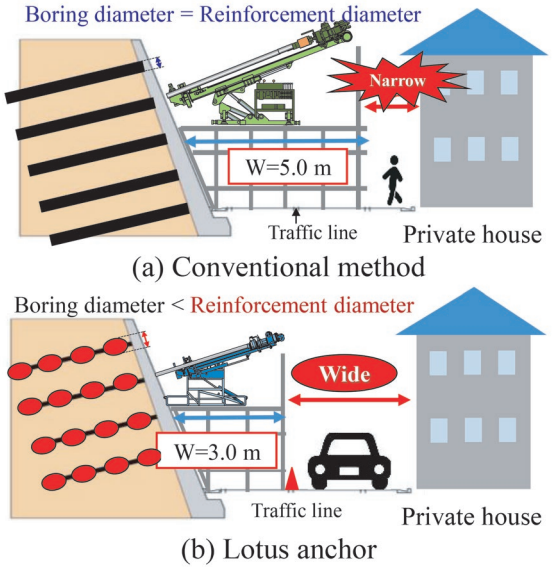

Fig. 2 Comparison of reinforcement methods

construction management methods for further efficiency and quality improvement.

2. Development and overview of soil reinforcement using pressurized injection

2.1 Conventional method characteristics and issues

Soil reinforcements are classified according to the diameter of the reinforcement material: small diameter (about 50 to 100 mm) nailing, medium diameter (about 100 to 300 mm) micro-piling, and large diameter (about 300 to 500 mm) dowelling. Table 1 shows construction methods often used for railway structures, including the Lotus Anchor developed in 2013, using pressurized injection material.

Because nailing is based on rock-bolt technology used in the NATM, which targets hard ground of the mountain, the reinforcement diameter is small. However, since the ground in embankments is softer than ground of mountain, in order to secure the friction resistance force necessary to stabilize an embankment through nailing, the reinforcement material has to be long and numerous.

The "Radish anchor" dowelling method, uses mechanical stirring to mix the ground as cement milk (solidifying material) is injected, while simultaneously placing the core material to construct thick reinforcement with a diameter ranging from 300 to 500 mm. Because the reinforcement diameter is large and the surface area is large, it is particularly effective in reinforcing embankments and collapsible ground where it is difficult to obtain sufficient frictional resistance force. However, the problem of this method is that if the ground is hard or contains large gravel, stirring is becomes insufficient, and construction becomes difficult.

In the "Carrot anchor method" micro-piling method, the ground is first bored, then the bores are replaced with cement milk and a core material is installed in the center to construct a medium-diameter reinforcement material. By borings using a high-output rotary percussion machine, this construction method can be used even on hard ground and ground containing gravel and cobblestones.

In this way, the type of soil reinforcement material is selected depending on the ground and site conditions, but when conventional

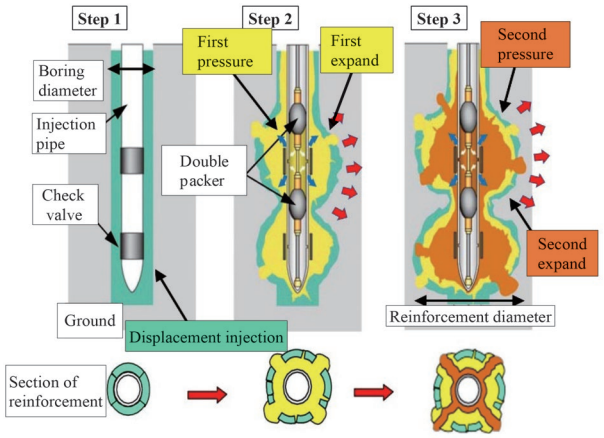

Fig. 3 Construction process

methods are used to reinforce existing structures, the following issues exist:

1) Larger construction machines are required for larger boring diameters, making it difficult to construct in narrow spaces such as urban areas. Generally, a width of approximately 3.5 to 5.0 m is required during construction (Fig. 2 (a)).
2) When reinforcing existing structures such as retaining walls, it is necessary to bore into the concrete wall. If the core boring diameter is large, the preparatory work for core boring will be large-scale, which will account for a large proportion of the construction cost and period.
3) It is necessary to complete the construction of reinforcement material from boring to inserting core material in a single construction period. For example, when there are time constraints, such as when construction is carried out at night between the last train and the first train, the construction period tends to be longer.

To address these issues, we developed "the Lotus Anchor" as a soil reinforcement method using pressurized injection material which can be achieved using small machines and can also expand the reinforcement diameter.

2.2 Soil reinforcement using pressurized injection

This article provides an overview and construction procedure for the Lotus Anchor. Figure 3 shows the construction procedure of the Lotus Anchor. The ground is pre-bored (φ115 mm) using a rotary percussion drill. An injection pipe is inserted into the boring hole and the boring hole is then filled with cement milk (grout) as the injection pipe is withdrawn (STEP 1). As with the Carrot anchor method, by using a rotary percussion drill, construction is possible even on ground containing gravel or large round stones, or on hard ground. In addition, replacement injection can prevent the bored ground from collapsing, so boring and pressurized injection can be performed in separate processes. Next, the replacement injection part is split open with pressurized water, and then grout is injected under pressure using a double pipe double packer to expand the reinforcement material (STEP 2). If a larger reinforcement resistance force is required, it is possible to expand the reinforcement diameter by repeatedly injecting it under pressure (STEP 3). According to the results of the pullout test described below, it is possible to construct reinforcement material with a diameter 2.0 times larger (φ230 mm) in sandy soil and 1.5 times larger (φ170 mm) in cohesive soil for a boring diameter of φ115 mm. Figure 4 shows the side view and cross section of the reinforcement constructed using pressurized in-

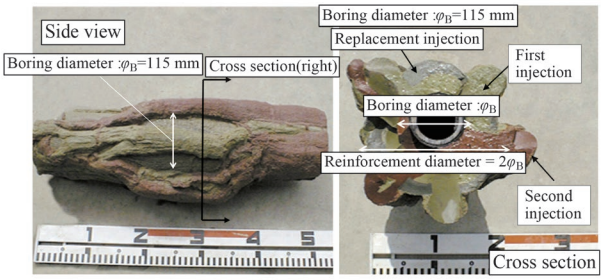

Fig. 4 Side view and cross of the reinforcement

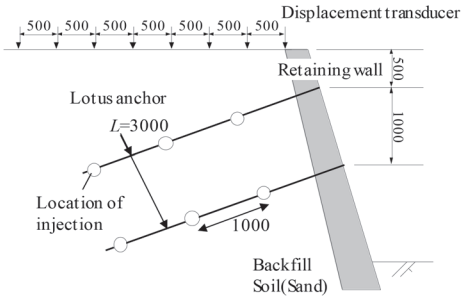

Fig. 5 Overview of construction test (unit in mm)

jection. It can be seen that the reinforcement diameter can be expanded to about twice the boring diameter on average by pressurized injection. The developed method can solve the above-mentioned problems with the following features:

- Because the boring diameter is small, construction can be performed in narrow spaces using a small machine with an occupied width of approximately 2.5 to 3.5 m (Fig. 2 (b)). In particular, if the space is very narrow, construction can be carried out with a minimum width of about 1.0 m by using a portable machine.
- It is possible to reduce the amount of core boring on the concrete wall of an existing structure.
- It is possible to carry out the boring and the construction of reinforcement material by pressure injection in separate processes. Therefore, it is possible to significantly shorten the construction period for construction affected by an operating railway, where there are constraints on the time available for construction.

The Lotus Anchor, which is applied to locations with low overburden pressure and requires evaluation of friction resistance force, has several issues in terms of both design and construction. Therefore, the authors conducted an investigation through construction tests, and report the results in Chapter 3.

3. Establishment of design and construction methods through construction test

3.1 Overview of construction test

Figure 5 shows an overview of the construction test. On the existing leaning wall constructed on sandy earth embankment, 3m-long soil reinforcement material was constructed at the overburden of 0.5 m and 1.5 m. In addition, rock bolts were installed as a comparison target for evaluating the pullout resistance of the reinforcement material.

3.2 Ground upheaval during construction

A preliminary test was conducted to verify the construction management conditions for pressurized injection. The specifications were set to be approximately three times the target reinforcement diameter (φ230 mm) (six times the boring diameter) in accordance with the RSI ground anchor standards [2]. Three injections were made each at a rate of 8 L/min, the upper limit injection pressure was 4 MPa, and the pressurized injection positions were set at a pitch of 1 m. As a result of the three injections, a large upheaval of total of about 26 mm(maximum) was observed. This is because in the standard for RSI ground anchors [2] the anchor body should have an overburden of 5 m or more, whereas the soil reinforcement method targets small overburdens of about 0.5 m.

Based on the results of the preliminary test, in the main test, the pressurized injection volume of grout was reset to a volume equivalent to the target reinforcement diameter (φ230 mm), based on the concept of split injection. In addition to resetting the pressurized injection volume, based on the results of preliminary tests, the control values were set to an injection rate of 2 to 5 L/min and a pressure of 1.5 MPa or less to prevent ground upheaval from occurring. Particularly at the top level where the overburden is small, if a pressurized injection is carried out based on the concept of split injection, there is a risk that the grout will flow out onto the ground surface. Therefore, the injection speed was adjusted to prevent abnormal runoff and ground displacement from exceeding allowable values. In addition, with reference to the railway track displacement limit value, in this test the allowable displacement of the ground was set to within 5 mm. Track loads exist in actual railway structures, but there was no railway track load in this test construction, so the test was conducted under conditions where ground displacement is more likely to occur.

In the test construction, by controlling injection, the maximum amount of upheaval was 4.02 mm and 0.81 mm, at overburden of 0.5 m and 1.5 m, respectively. The results of the construction test confirmed that by controlling injection by setting limits for injection speed and injection pressure, there was little effect on displacement at the track level when the overburden was approximately 1.5 m or more.

3.3 Evaluation of pullout resistance

When a pullout force is applied to the soil reinforcement material constructed using the Lotus Anchor, a resistance force as shown in Fig. 6 occurs. The pullout resistance in design is determined by the minimum value from among (1) the tensile strength of the core material, (2) the friction resistance force between the grout and the ground, (3) the adhesion force of the core material and (4) the adhesion force of the injection pipe. The pullout resistance in design is often determined by (2) the friction resistance force between the grout and the ground. However, because the diameters of reinforcements constructed using the Lotus Anchor are not uniform, it is not clear whether it is possible to evaluate the friction resistance force in the same way as ordinary soil reinforcement materials with uniform diameters.

Therefore, we conducted pullout tests on the reinforcement material constructed during the construction test to confirm the ultimate friction resistance force of the reinforcement material by pressurized injection. Table 2 shows a list of pullout test conditions and results. Here, a non-pressure injection type rock bolt (Case 1) was used for comparison, with the reinforcement diameter set to be the same as the hole diameter of the Lotus anchor. In Cases 2 and 3,

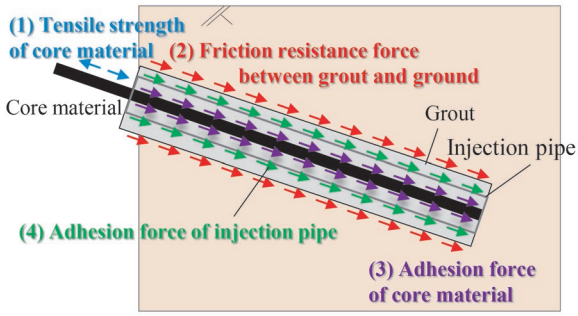

Fig. 6 Resistance force of reinforcement

Table 2 List of pullout test

	Case	Overburden	Target reinforcement diameter (mm)	Ultimate friction resistance (kN)
Rock bolt	1	1.5 m	115 mm	72
Lotus anchor	2	0. 5 m	230 mm	160
	3	1.5 m	230 mm	161

constructed using the Lotus Anchor, the target reinforcement diameter was twice (φ 230 mm) the boring diameter (φ 115 mm).

Based on the ultimate pullout resistance of Case 1, the ultimate pullout resistance of Cases 2 and 3, which received pressurized injections to correspond to twice the boring diameter, is 2.2 times, which is more than double, and it can be considered that the reinforcement diameter is at least twice as large.

Generally, in the design of soil reinforcement methods, the pullout resistance is determined by the frictional resistance between the grout and the ground. The frictional resistance between the grout and the ground is calculated by multiplying the ultimate surface frictional resistance per unit area τ by the surface area of the reinforcement material.

Figure 7 shows the ultimate friction resistance stress degree for each case. In reality, the reinforcement diameter of Lotus Anchor is non-uniform, but this is the result of setting the ultimate friction resistance stress degree τ as the target reinforcement diameter according to the injection amount. In both Cases 2 and 3, the same ultimate friction resistance stress degree as that of the rock bolt (Case 1) was obtained. This suggested that the frictional resistance between the grout and the ground in a Lotus Anchor could be set by the following method: multiplying the surface area set from the target reinforcement diameter according to the injection volume, by the ultimate friction resistance stress degree of the conventional method. Figure 8 shows the relationship between the ultimate friction resistance stress degree and the N value for each soil type. It is noted that the ultimate friction resistance stress degree was calculated using the method described above using the pullout resistance obtained from the pullout test conducted at the construction site. The results of this construction test are also added to the figure.

In addition, the estimated values in the Design Standards for Railway Structures and commentary -Retaining Structures- (hereinafter referred to as the "Retaining Standard") [3] are shown by the dashed lines. Regarding the test results for the Lotus Anchor, as mentioned above, the target reinforcement diameter was set to twice the boring diameter to determine the ultimate friction resistance stress degree. The N value of the sandy ground that was the subject of this test was 4. The ultimate frictional resistance was equal to or larger than the estimated value for the ground with an N value of 10 in Retaining Standard. The above confirmed the validity of calculating the pullout resistance force, also in the Lotus Anchor, by multiplying the ultimate friction resistance stress degree in the conventional method by the surface area calculated from the target reinforcement diameter.

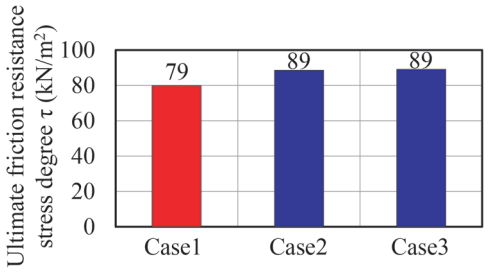

Fig. 7 Comparison of ultimate friction resistance stress degree

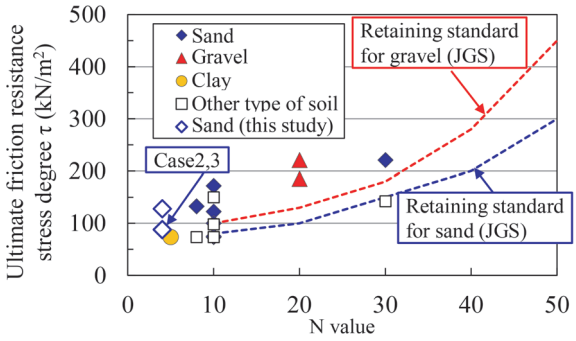

Fig. 8 Relationship between ultimate friction resistance stress degree and N value

4. Application example for reinforcing existing structures

This chapter introduces some examples of the method being applied at railway sites.

The first example is a seismic reinforcement site for a bridge abutment directly under a railway [4]. Figure 9 shows a cross-sectional view of the site. The bridge abutment targeted for reinforcement faces an extremely narrow road with a width of 2.4 meters, so that it difficult to bring in construction machinery. These conditions were taken into account, and the Lotus Anchor was adopted. A core drill was used because this site is very narrow. As shown in Fig. 9, it is necessary to construct three stages of reinforcement material, and the top level has a minimum overburden of approximately 1.0 m, and is constructed directly below the railway tracks. For safety reasons, the top level was constructed with the track closed, and the presence or absence of any heaving was checked. The maximum pressure of the reinforcement material on the top level was 0.8 to 1.6 MPa, which was within the specified range (1.5 to 2.0 MPa), and no track heaving was observed. Since the weight of the soil is heavier in the second and deeper levels than in the top level, it was assumed that track heaving would not occur, so construction was carried out in daytime. The construction was completed safely even in daytime, and we were able to shorten the construction period and reduce costs.

The second example is a reinforcement site for an existing leaning retaining wall [5]. In the original design, the retaining wall was to be reinforced with rod-shaped reinforcements with a diameter of 150 mm. However, constructing the reinforcement with this diameter, would have required a large boring machine, and a con-

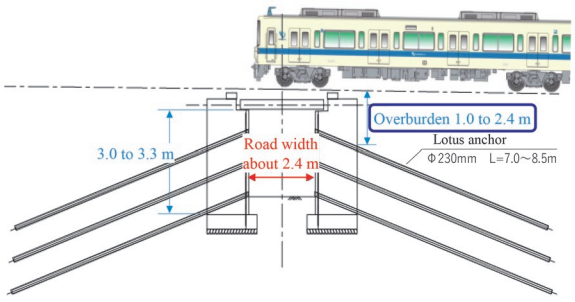

Fig. 9 First application example [4]

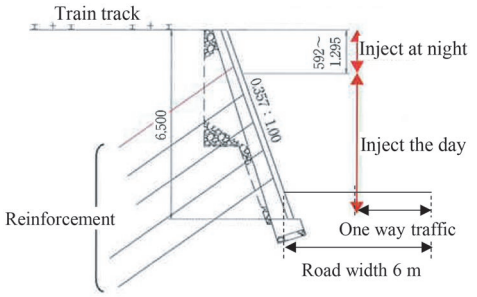

Fig. 10 Second application example [5]

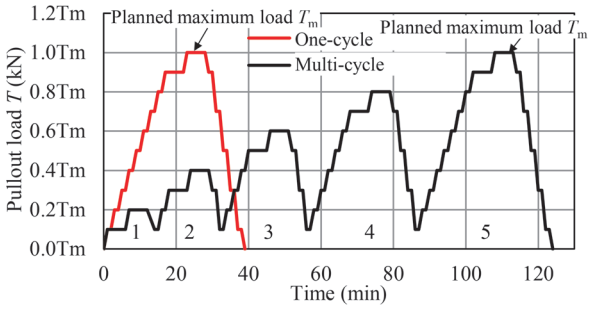

Fig. 11 One-cycle tests and multi-cycle test

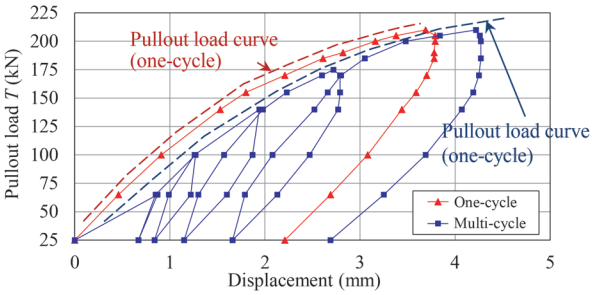

Fig. 12 On-site acceptance test results

struction width of 4.5 to 5.0 m. As shown in Fig. 10, the road width was approximately 6.0 m from the end of the slope. However, since it is necessary to prepare a 3 m wide one-way lane, the width that can be prepared as the construction site width was approximately 3.0 m. Therefore, the Lotus Anchor, which uses a small boring machine and has high boring capacity, was adopted for this site. A spring drill that fits within the width of the construction site was used as the boring machine. Among the five levels of reinforcement material, the top level had overburden of 0.59 to 1.29 m and was constructed directly under the track (Fig. 10). Because there was a concern that track displacement may occur when constructing the top level, the boring was carried out during the day, the pressurized injection was carried out separately at night, to measure the amount of track displacement. The amount of track displacement during pressurized injection was vertical: +0.3 mm to −0.6 mm, horizontal: +1.2 mm to −1.6 mm, both within the control value ±3.5 mm. Based on these results, it was determined that displacement exceeding the control value would not occur in the second and deeper levels during pressurized injection, and boring and pressurized injection were carried out in daytime. In the end, construction was completed safely.

5. Quality confirmation method and points to note during construction

As mentioned in the previous chapter, the Lotus Anchor method was developed in 2013 and has been applied to various sites [6] since then. The construction manual for this method was revised in 2022 [7] incorporating knowledge gained from past construction results regarding points to keep in mind during construction and quality confirmation methods.

5.1 Quality confirmation method

The quality of reinforcement materials is checked through pullout tests. The pullout test consists of a suitability test to check the ultimate friction resistance force and an acceptance test to check the designed pullout resistance. Additionally, testing loading methods are classified into one-cycle tests and multi-cycle tests; the former has the advantage of simplifying the test, while the latter is highly adaptable to repeated loading conditions. Figure 11 shows a conceptual diagram of a one-cycle test and a multi-cycle test. The one-cycle test is a method of applying a pullout load in stages up to the planned maximum load T_m one-cycle at a time to check whether the load will not pull out. On the other hand, the multi-cycle testing is a method in which multiple cycle tests are performed while gradually increasing the maximum load relative to the planned maximum load T_m. It can be seen that the multi-cycle test requires a longer test time than the one-cycle test. In the conventional method, at least 3% of the total number of one-cycle test are to be carried out by the acceptance test.

On the other hand, the old construction manual for the Lotus Anchor [6]) basically calls for conducting multi-cycle tests. This is because in the Lotus Anchor, the reinforcement is enlarged from the diameter of the boring, so it was necessary to carefully confirm the reinforcement diameter expected in the design and the development of the corresponding pullout resistance. However, as mentioned above, the number of construction cases has increased. Therefore, it is thought that more rational quality control will be possible by examining the relationship between pressurized injection volumes and pullout resistance forces and the influence of differences in the number of test cycles.

As part of this effort, we conducted acceptance tests on reinforcement materials constructed on conventional railway embankments. The results of confirming the differences between one-cycle tests and multi-cycle tests are shown in Fig. 12 [8]. In the figure, the curve that includes the maximum value of each cycle is shown as the pullout load curve. The pullout load curves for the one-cycle and multi-cycle tests were similar, and no significant difference was observed in the amount of residual displacement after the tests. In addition, in the multi-cycle test, the amount of displacement was

almost the same within the hysteresis load. This result indicates that it became clear that hysteresis characteristics were such that there was almost no progression. This suggests that a dominant displacement occurs when initial load is applied. From the above results, it is considered that there is no problem in the acceptance test even if a one-cycle test is used for the Lotus Anchor. Based on these results, the revised construction manual [7] changed the principle for an acceptance test to a one-cycle test.

5.2 Points to note during construction

When construction is carried out adjacent to important structures, such as directly beneath the tracks, it is important to carry out measurements and manage the site to prevent track heaving from occurring. To ensure safe construction without heaving the ground, the construction manual stipulates control values. However, since the properties of the ground vary from site to site, it is assumed that fluctuations in injection pressure and upper limit pressure will also vary depending on the ground. Therefore, we added the importance of performing a trial injection first and setting control standards for injection speed and pressure that are appropriate for the ground in question. Furthermore, during pressurized injection, not all of the grout is injected into the ground, so that it may flow out from around the mouth of the injection pipe. In this case, since the required amount of injection may not be secured, there is a risk that the formation of soil reinforcement material will be insufficient. Therefore, we added that when pressurized injection is used, the conditions of the surrounding ground should be measured and managed, and the situation around the injection port should be checked.

6. Conclusions

This paper reports on construction tests conducted during the development process of the Lotus Anchor method, including evaluation of pullout resistance characteristics, examples of subsequent construction, and construction management methods aimed at further improving the efficiency and quality of this method. The following results were obtained:

- By pressurized injection, it is possible to construct reinforcement material with a diameter 1.5 to 2.0 times larger than a boring diameter of 115 mm. Therefore, the number and length of reinforcement material to be installed can be reduced compared to the non-pressure injection method for the same boring diameter.
- By using a small boring machine, construction can be performed in narrow spaces. Since the boring diameter is small, the amount of boring in concrete walls can be reduced when reinforcing retaining walls, bridge abutments, etc.
- Based on test constructions and field experience, it is possible to perform construction with managed split injection when the overburden is 1.5 m. Furthermore, construction can be performed safely even at shallower depths than 1.5 m by controlling the injection speed and injection pressure.
- The construction manual has been revised by adding more rational quality control and suggesting points to keep in mind during construction.

References

[1] Nakajima, S., Ohashi, J., Takahashi, T., Beppu, M., Yokota, K., "Development of "Lotus Anchor" Method, a soil reinforcement method using repeated injection," *Foundation engineering and equipment (Kiso-ko)*, Vol. 41, No. 11, pp. 74-76, 2013 (in Japanese).

[2] RSI Anchor Association, *RSI Ground Anchor Method Design and Construction Manual*, 2021 (in Japanese).

[3] Railway Technical Research Institute, *Design Standards for Railway Structures and Commentary, Earth Retaining Structures*, Maruzen Publishing, 2012 (in Japanese).

[4] Degawa, H., Yamamoto, T., Beppu, M., "An example of seismic reinforcement using the "Lotus Anchor" Method, a repeated injection type soil reinforcement method, directly beneath railway tracks," *Annual Academic Conference of the Japan Society of Civil Engineers*, Vol. 72, pp. 1203-1204, 2017 (in Japanese).

[5] Beppu, M., Nakajima, S., Tamura, Y., "Reinforcement of retaining walls using soil reinforcement materials in narrow areas - Lotus Anchor -," *Foundation engineering and equipment (Kiso-ko)*, Vol. 44, No. 7, pp. 70-72, 2016 (in Japanese).

[6] RRR Construction Method Association, *RRR-Nail Lotus Anchor Method Construction Manual*, 2017 (in Japanese).

[7] RRR Construction Method Association, *RRR-Nail Lotus Anchor Method Construction Manual*, 2022 (in Japanese).

[8] Kurakami, Y., Nishida, H., Yoshida, S., Yano, K., Fujimura, M., Toshito, S., "A study on the quality confirmation method of the Lotus Anchor method," *Geotechnical Engineering Research Conference*, Vol. 56, 13-7-4- 02, 2021 (in Japanese).

Authors

Yuki KURAKAMI, Ph.D.
Assistant Senior Researcher, Foundation & Geotechnical Engineering Laboratory, Structure Technology Division
Research Areas: Geotechnical Engineering

Masaaki BEPPU
RAITO KOGYO CO., LTD.
Research Areas: Geotechnical Engineering

Susumu NAKAJIMA, Ph.D.
Senior Chief Researcher, Foundation & Geotechnical Engineering Laboratory, Structure Technology Division
Research Areas: Geotechnical Engineering

Sumio YAZAKI
Integrated Geotechnology Institute Limited
Research Areas: Geotechnical Engineering

Centrifugal Model Test and Design Method for Temporary Retaining Wall Using Soil Buttress as Displacement Suppression

Takashi USHIDA **Takaki MATSUMARU**
Foundation & Geotechnical Engineering Laboratory, Structures Technology Division

Takashi NAKAYAMA
Tunnel Engineering Laboratory, Structures Technology Division

It is important to suppress the displacement of temporary retaining wall when excavating in urban areas close to existing structures. Soil buttresses have economic advantages compared to struts, such as in large-scale excavation works. On the other hand, a challenge in designing such temporary retaining walls is needed to consider displacement suppression mechanism using methods such as FEM. In this paper, we clarified the displacement suppression mechanism of soil buttresses using centrifuge model tests with excavation. Cutout shaped soil buttresses were proposed based on the test knowledge. In addition, we proposed a design method of temporary retaining walls using soil buttresses to suppress the displacement.

Key words: *temporary retaining wall, soil buttress, displacement calculation, beam-spring model, centrifugal model test*

1. Introduction

Controlling the displacement of temporary earth retaining walls is an essential issue in minimizing the impact of urban excavation works on the surrounding ground and structures. Struts are most commonly used for suppressing displacement. These are steel members installed against earth retaining walls. However, in some excavation work, as the volume of steel (including intermediate piles) increases, economic efficiency decreases.

Soil buttresses (Fig. 1) are another method for suppressing displacement, which are a form of discrete wall-type ground improvement placed adjacent to the retaining wall to locally suppress displacement. This method is expected to be more economical than struts for large excavation works. The beam-spring model (Fig. 2) is the most commonly used design for temporary earth retaining walls [1][2]. In this method, the struts are represented as elastic foundations with the stiffness calculated according to the specifications of the struts. On the other hand, soil buttresses are represented as a stiffening effect of the improved soil. Therefore, only the horizontal improved ratio and depth can be considered. Furthermore, the displacement suppression effect disappears after the yielding of the unimproved ground since the improved and unimproved sections cannot be separated in this method. Thus, as the existing method considers few specifications, finite element analysis is necessary to design a model which covers the geometry and resistance mechanism [3][4].

This paper therefore first reveals the resistance mechanism with a centrifuge model test focusing on the displacement suppression effect according to the shape of the soil buttresses. Secondly, it develops a design method using the Beam-Spring model for temporary retaining walls using the soil buttress as a displacement suppression measure. Finally, the calculation result of the centrifuge model test is shown as an example of the application of the design method.

2. Centrifuge model test with excavation process

2.1 Test conditions

In this study, we used a centrifuge located at the National Institute of Occupational Safety and Health, Japan (JNIOSH) [5] (Fig. 3). The platform has plane dimensions of 1.3 m × 1.1 m, a turning radius of 2.38 m, and a maximum centrifugal acceleration of 100 G.

The centrifuge is equipped with an excavation device shown in Fig. 4 [6], which can excavate the model soil during centrifugal

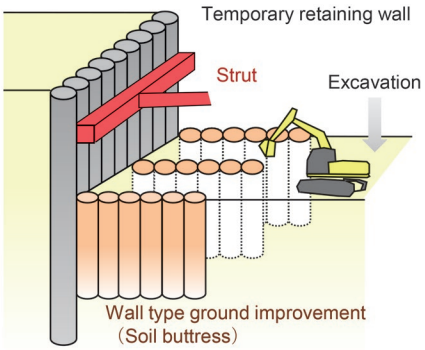

Fig. 1 Excavation work with temporary retaining wall

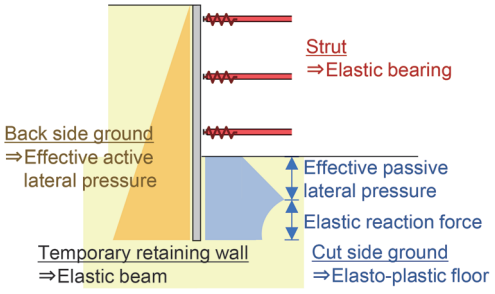

Fig. 2 Beam-spring model

loading. The device consists of an excavating blade, a frame, and a blade controller (real time controller with 3 orthogonal axis).

The overview of the model is shown in Fig. 5. The model ground consists of lower clay, bedding clay (divided into six layers), upper sand and excavated soil (divided into eight layers) and is made by controlling the amount of the input soil and the surface height. In this test, assuming ground conditions likely to cause displacement of the temporary retaining wall, the following materials were used:

Beneath the final excavation: Kaolin clay (mixed with AX kaolin: MC clay = 1:1, unit volume weight 18 kN/m^3, water content 120%, E_{50} = 7,000 kN/m^2 equivalent).

From above the bottom of the final excavation: *Toyoura* sand (unit volume weight 15 kN/m^3, unit water content 120%, E_{50} = 7000 kN/m^2 equivalent). The coefficient of deformation, E_{50}, is an assumed value from triaxial compression tests of confining pressure corresponding to the stress field of the actual dimensions.

The excavated sand was inclined at 45 degrees to facilitate excavation, and the ground water level was set around the final excavation bottom. A drainage layer of compacted *Tohoku* Silica Sand No. 4 was placed at the lowest part of the model ground to drain the pore water generated by consolidation of kaolin clay.

As described below, this test was carried out at 50 G, the final excavation depth of the model was equivalent to 9.0 m in actual size. In general, an unbraced temporary retaining wall is not used under these conditions. However, the model conditions were set to allow displacement to occur easily, as the test focused on the displacement suppression effect of the soil buttress.

The clay layer is pre-consolidated up to 100 kPa using a bellofram cylinder at 1 G and then pre-consolidated by centrifugal force at 50 G. During the centrifugal pre-consolidation, a dummy sand layer for centrifugal consolidation was constructed on top of the clay layer in order to create a stress similar to the test condition. The dummy sand layer was then removed, and the sand layer for the test was constructed.

The retaining wall model was an acrylic plate (t = 10 mm). The thickness was determined by focusing on the bending stiffness (25,000 kN·m^2) at 50 G, assuming a pile-type diaphragm wall (encased steel: H588 × 300 × 12 × 20 @ 600 mm). In addition, to prevent rotational restraint at the bottom edge of the model, it was machined into wedge shape and installed in a V-shaped receiver.

The improvement model (soil buttress model) was made by mixing cement and foam beads (water : cement : foam beads = 1 : 5 : 0.4), and its unit volume weight was matched with that of the bedding clay to prevent settlement or uplift due to density difference. The models were installed after centrifugal pre-consolidation of the clay layer. The model surface was left as cast surface without Teflon sheet or other materials, since it was assumed that the shear resistance occurred at the boundary between the ground and the soil buttress.

During the test, the horizontal displacement of the top of the retaining wall model was measured with two laser displacement transducers. The surface strain on the retaining wall model was measured with strain gauges, and the lateral pressure was measured with small pressure gauges. The strain gauges and small pressure gauges were placed at the same depth on both sides of the retaining wall model at vertical intervals of approximately 40 mm.

In this study, three cases were carried out focusing on the shape of the soil buttress: Case1 was without a soil buttress, and Case2 was with a rectangular soil buttress (D 100 mm × B 160 mm × t 15 mm, this B/D was used in excavation works). In addition, Case3 was with a notched shape soil buttress (removing the area where only a

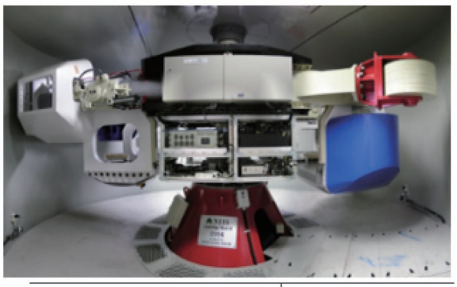

Plane dimensions of platform	1.3 m×1.1 m
Rotating radium	2.38 m
Maximum centrifugal acceleration	100 G

※Specification of static platform

Fig. 3 Centrifuge [5]

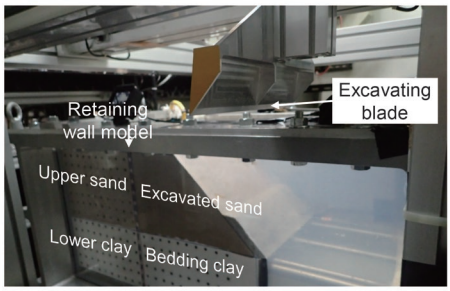

Fig. 4 Excavation device

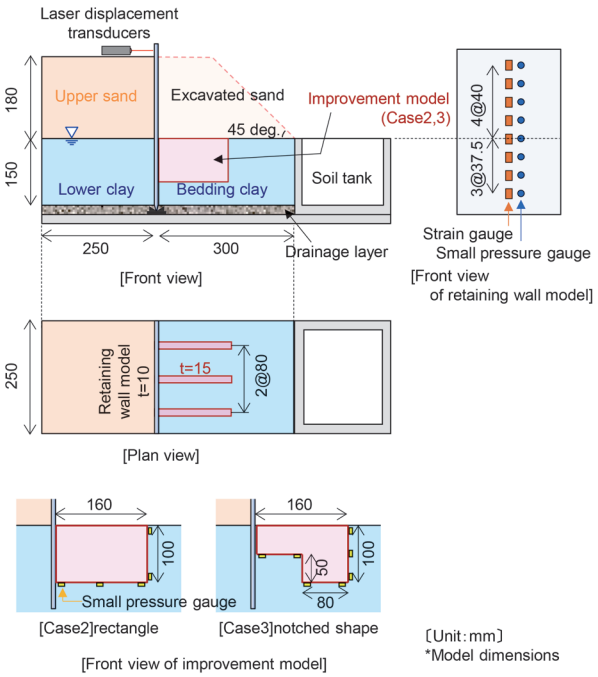

	Improvement model	Vertical size × Horizontal size
Case1	---	---
Case2	Rectangle	100 mm × 160 mm
Case3	Notched shape	100 mm × 160 mm (Notched area: 50 mm × 80 mm)

Fig. 5 Model

small displacement suppression effect is expected from the rectangular soil buttress, from the result of Case2)

The time history of the centrifugal acceleration in Case2 is shown in Fig. 6. The effective turning radius is set to 2.14 m (for letting that the centrifugal load would be applied 50G at the final excavation bottom) and the angular acceleration to 0.02 rad/sec^2.

2.2 Test result

2.2.1 Displacement and bending moment of the retaining wall model

The displacement and bending moment distribution of the retaining wall model after the final excavation are shown in Fig. 7. In the following, the measured values are converted to actual dimensions. The displacement of the retaining wall model after excavation is larger than on the upper side (Fig. 7(a)). This is the same trend as that of common unbraced temporary retaining walls.

The displacement distribution of the retaining wall model shown in Fig. 7(b) is calculated by following steps.

(1) calculating the curvature from the increase in surface strain from before excavation of the retaining wall model based on Bernoulli-Euler theory.

(2) fitting the displacement with following boundary conditions.

a) the calculated displacement of the top of the model is equal to the measured displacement by laser displacement transducers.

b) the calculated displacement of the bottom of the model is zero.

The calculated displacement distribution shows the same trend as the test result shown in Fig. 7(a).

The displacements at the top of the retaining wall model and at the bottom of the final excavation after excavation are shown in Fig. 8. The displacements in Case2 which used the rectangular improvement model resulted in 35%, 65% less displacement, respectively, than those in Case1 which did not use the improvement model. In addition, in Case3, where improvement model with economical shape based on the results of Case2 were used, the displacements were reduced by 26% and 42%, respectively, compared to Case2. These results suggest that the selection of soil buttress shapes according to the required displacement suppression effect and the design method for evaluating various shapes can lead to more economical excavation works.

The bending moment distribution shown in Fig. 7(c) is calculated by following steps.

(1) calculating the bending strain from the increase in surface strain from before excavation of the retaining wall model based on Bernoulli-Euler theory.

(2) multiplying the bending stiffness of the retaining wall model by the bending strain distribution calculated with following boundary conditions

a) the bending strain at the top of the retaining wall model is zero.

b) the bending strain at the bottom of the retaining wall model is zero.

The calculated bending moment around the final excavation bottom is a large negative value. This follows the same trend as common unbraced retaining walls. The bending moment of the wall model around the bottom in Cases 2 and 3 is smaller than in Case1. It is therefore suggested that the passive resistance increased at the depth where the improvement model was installed.

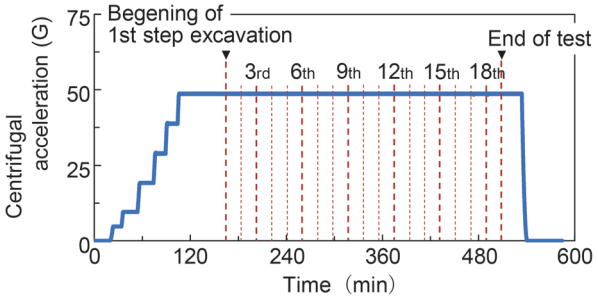

Fig. 6 Time history of centrifugal acceleration (Case2)

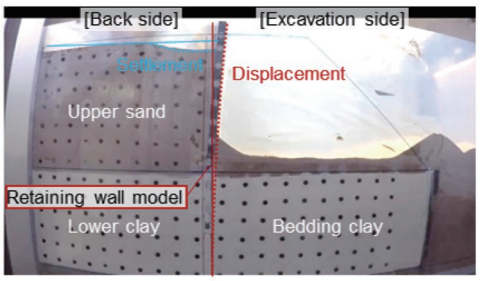

(a) Model after the final excavation (Case1)

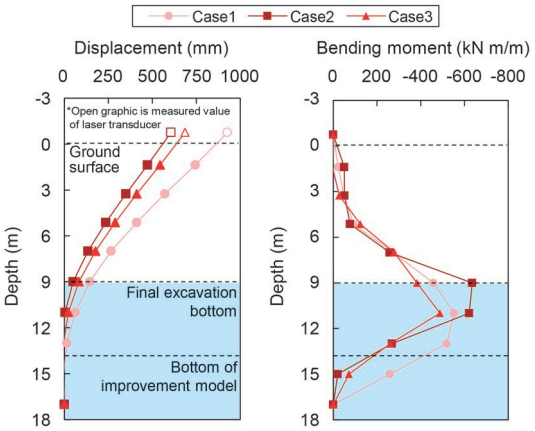

(b) Displacement (c) Bending moment

Fig. 7 Time history of centrifugal acceleration (Case2)

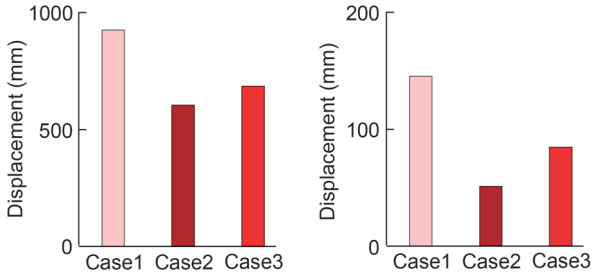

(a) Top (b) Final excavation bottom

Fig. 8 Displacement of the retaining wall model after final excavation

2.2.2 Subgrade reaction distribution and resistance mechanism of improvement model

The subgrade reaction distribution during excavation in Cases 2 and 3 is shown in Fig. 9. The subgrade reaction at the bottom is corrected for the deduction in the overburden load (weight of excavated sand) due to excavation. The large subgrade reaction suggests that the interaction between the improvement model and the ground is large, and the displacement suppression effect is large in the area where the subgrade reaction is large.

In both Cases 2 and 3, the bottom subgrade reaction increased in the first half of the excavation compared to that before the excavation, suggesting that the bottom of the improvement model has a greater displacement suppression effect. However, in Case2 with the rectangular improvement model, the bottom subgrade reaction on the side of the retaining wall model is about 70% of that on the opposite side, suggesting that the displacement suppression effect is relatively small. In the latter half of the excavation, the bottom subgrade reaction decreased while the tip subgrade reaction increased, suggesting that the tip of the improvement model has a greater displacement suppression effect. This suggests that the displacement suppression effect is different for each part of the improvement model and the stage of excavation.

The displacement suppression mechanism of the improvement model estimated by the subgrade reaction is shown in Fig. 10. In both Cases 2 and 3, the improvement model displaces in the horizonal mode in the first half of excavation, with an additional rotational mode in the latter half of excavation. Also, the lateral pressure of the retaining wall model decreases with excavation, suggesting that the improvement model bears some of the lateral pressure. These indicate that the improvement model has an effective displacement suppression effect.

2.3 Summary of section

This centrifugal model test focuses on the displacement suppression effect depending on the shape of the improvement model. The results show that the effects are different depending on the shape even if the installation depth is the same. These different effects cannot be calculated by the existing design method where soil buttresses are expressed by a mathematical model depending on only the improvement ratio, when dealing with the composite ground. This result suggests that a design method that calculates the displacement suppression effect of the soil buttress depending on the shape based on the resistance mechanism, promotes the economy of excavation works.

The results of these test suggest the following facts.

(1) The displacement suppression effect is exerted by the subgrade reaction at the bottom and tip of the improvement model.

(2) The resistance force may be overestimated by calculating if the entire of the bottom and tip face is effective.

In addition, the estimation of the displacement suppression effect caused by the frictional resistance force of the improvement model is a future task.

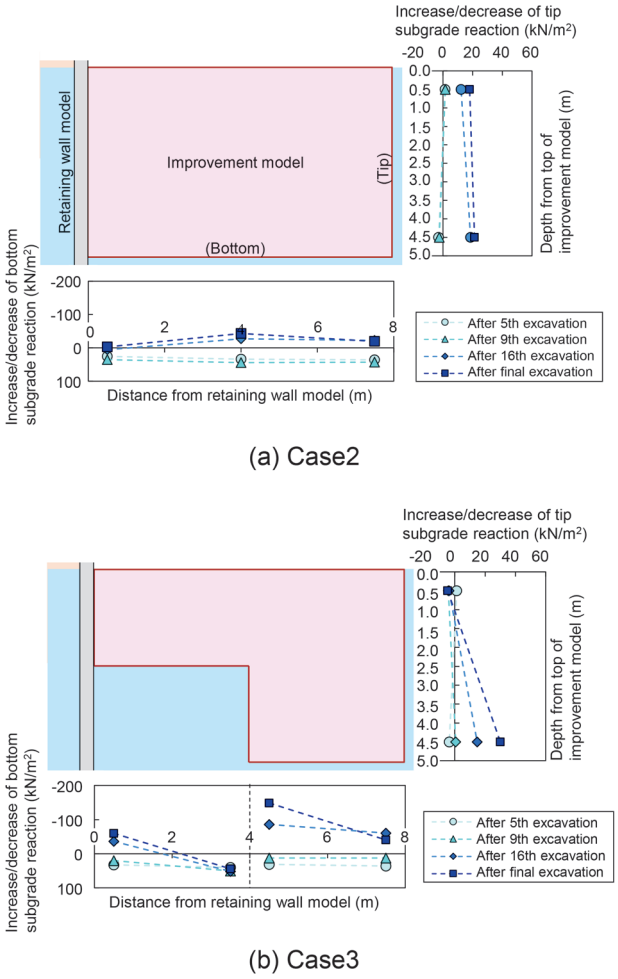

Fig. 9 Subgrade reaction of improvement model

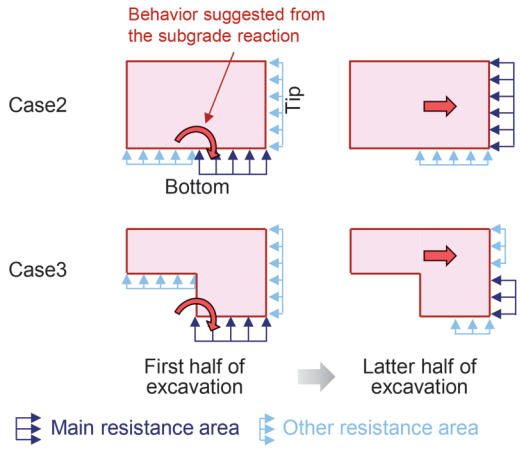

Fig. 10 Displacement suppression mechanism of improvement model

3. Design method of temporary retaining wall using soil buttresses

3.1 Subgrade reaction characteristics of soil buttress

This chapter presents a method for calculating the ground resistance characteristics of a soil buttress based on its shape for the beam-spring model. The concept of the proposed method based on the beam-spring model is shown in Fig. 11. Since the strut is modeled as an elastic spring in the beam-spring model, the soil buttress is modeled as an elastic bed. The elastic bed can be converted into nodal elastic springs and is therefore easy to handle.

The concept of calculating the coefficient of subgrade reaction

of a soil buttress is shown in Fig. 12. In the beam-spring model, the balance of lateral loads is calculated. It is therefore necessary to convert the vertical subgrade reaction at the bottom of the improvement (hereinafter referred to as "bottom resistance") into the horizontal subgrade reaction at the tip of the improvement (hereinafter referred to as "tip resistance").

The following equation is proposed to calculate the coefficient of subgrade reaction, k_h', which is used to calculate the stiffness of the elastic bed, taking into account the shape of the improvement and the ratio between the vertical and the horizontal coefficient of subgrade reaction.

$$k_h' = a\,B'/D\,k_h = (B'/D)\,k_v \quad (1)$$

where B' is the effective width, D is the height, k_h is the horizontal coefficient of subgrade reaction, and a is the ratio between the horizontal coefficient of subgrade reaction k_h and the vertical one k_v ($= k_v/k_h$).

The effective width B' is assumed to have the intersection of the bottom and the perpendicular through the center of gravity as the center of rotation with reference to the previous study [7].

In the proposed method, the bottom resistance is taken into account in the stiffness of the elastic bed, assuming that the tip resistance is included in the resistance of the ground. Also, this method calculates the retaining wall displacement without the suppression effect of the friction force at the improvement of the side surface. In addition, this method assumes that the improvement is not damaged.

3.2 Trial calculations of the centrifugal model test

The trial calculations of the centrifugal model test shown in chapter 2 is carried out. The purpose of this calculation is to show the process and to confirm the accuracy of the estimation of the displacement suppression effect of the soil buttress by the proposed method.

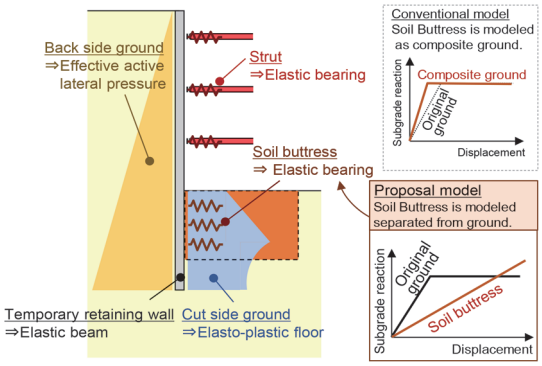

Fig. 11 Concept of proposed method

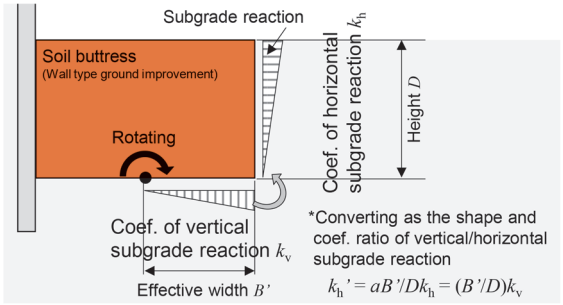

Fig. 12 Concept of calculating for coefficient of subgrade reaction of soil buttress

Therefore, firstly, the soil properties are adjusted so that the displacement of the retaining wall model is equivalent to that in Case1 without the improvement model. Secondly, the stiffness of the elastic floor expressed by a mathematical model of the improvement model in Cases 2 and 3 is calculated by the method shown in Fig. 13. Since the calculated effective width B' of the economically shaped improvement model in Case3 is smaller than the rectangular one in Case2, the displacement suppression effect depending on the shape is estimated by this method.

Focusing on the displacement of the retaining wall model at the final excavation bottom, the trial calculation results by the proposed method and the results of the centrifugal model test are shown in Fig. 14. It shows that the displacement given by proposed method is larger than the test result, and indicates a trend showing that the displacement of the retaining wall is suppressed as B'/D increases.

4. Conclusions

This paper first shows that the displacement suppression effect depending on the shape of the soil buttress is shown by a centrifugal model test. Secondly, it proposes a design method that can calculate this effect and reports on a trial calculation using the method.

The next challenge will be to achieve displacement suppression with the side surfaces of a soil buttress.

Acknowledgment

The authors would like to express their sincere gratitude to Nobutaka HIRAOKA Dr. Eng., Naotaka KIKKAWA Dr. Eng. (National Institute of Occupational Safety and Health, Japan), Prof. Kazuya ITOH (Tokyo City University) for their guidance and teachings.

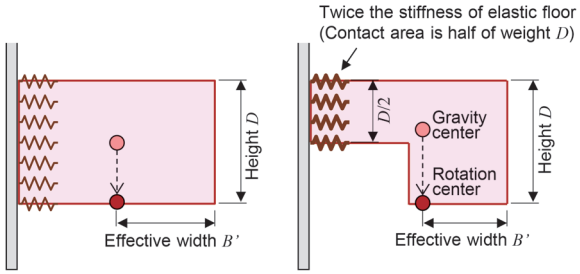

Fig .13 Modeling of improvement model

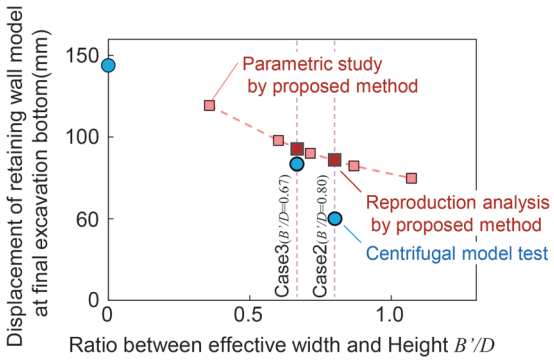

Fig. 14 Trial calculation results by the proposed method

References

[1] Railway Technical Research Institute, *Design Standards for Railway Structures and Commentary [cut and cover tunnel]*, Maruzen, 2021. (in Japanese).

[2] Japan Society of Civil Engineers, *Standard specifications for tunneling-2016: cut-and-cover tunnels*, 2016. (in Japanese).

[3] Takada, N., Oka, F., Kimoto, S. and Higo, K., "Investigation on Deformation Effect of Temporary Retaining Wall and Deformation," *Abstract of 2010 JSCE annual meeting*, Vol. 65, pp. 669-670, 2010. (in Japanese).

[4] Takada, N., Shimono, K., Oka, F., Kimoto, S. and Higo, K., "Deformation Analysis for Excavation Work at Osaka clay layer by Elasto-Viscoplastic Finite Element Method," *Abstract of 2011 JSCE annual meeting*, Vol. 66, pp. 503-504, 2011. (in Japanese).

[5] Ito, K., Tamate, S., Toyosawa, Y. and Horii, N., "Development of NIIS-Mark II Centrifuge," *Research Reports of the National Institute of Industrial Safety*, NIIS-RR-05, 2006. (in Japanese).

[6] Ito, K., Hayashi, T., Kikkawa, N., Hiraoka, N. and Konami, T., "Excavation of Slope Reinforced Temporary by Soil Nailing Using In-flight Excavator in Centrifuge," *Journal of JSCE C*, Vol. 75, No. 1, pp. 103-114, 2019. (in Japanese).

[7] Sato, E., Aoki, M. and Maruoka, M., "Evaluation of Prevention Effect on Earth Retaining Wall Displacement by Buttress," *Journal of Structural and construction Engineering (Transactions of AIJ)*, No. 611, pp. 79-86, 2007. (in Japanese).

Authors

Takashi USHIDA, Dr.Eng.
Senior Researcher, Foundation & Geotechnical Engineering Laboratory, Structures Technology Division
Research Areas: Tunnel Engineering

Takaki MATSUMARU, Dr.Eng.
Senior Researcher, Foundation & Geotechnical Engineering Laboratory, Structures Technology Division
Research Areas: Geotechnical Engineering

Takashi NAKAYAMA, Dr.Eng.
Senior Researcher, Tunnel Engineering Laboratory, Structures Technology Division
Research Areas: Tunnel Engineering

Natural Frequency Identification Method for Substructures in Railway Bridges and Viaducts

Kazunori WADA **Kimitoshi SAKAI**
Structural Dynamics and Response Control Laboratory, Center for Railway Earthquake Engineering Research

We have proposed a method for identifying the natural frequency of single structures from data obtained by measuring the vibration of railway bridges and viaducts. With this method, the natural frequency of a single structure can be theoretically calculated using undamped natural frequencies and the natural modes of whole structures. The eigenvalue analysis shows that the natural frequency of a single structure can be identified by the proposed method.

Key words: *substructure, natural frequency, identification, railway bridges and viaducts*

1. Introduction

Railway bridges and viaducts are composed of groups of continuous substructures via superstructures and bearings. Therefore, vibration characteristics such as natural frequencies obtained from vibration measurements are the values of entire structures as whole systems, including the influence of vibrations of adjacent structures. This is clear from the comparison of actual measurements of single bridge piers and the entire structure of a road bridge [1], and the actual measurements and analytical studies of the coupling of railway structure groups [2].

The vibration characteristics of entire structures obtained by vibration measurement have been used to diagnose their health. Impact and vibration testing [3, 4] has been used for many years, especially in the field of railways. This is a method for evaluating the health of a single substructure by applying impact vibration to a target structure of a bridge or viaduct and evaluating the natural frequency of the entire structure from the obtained waveform. Impact and vibration testing is an effective non-destructive inspection method because damage to the substructure and deterioration of stability cause a decrease in the natural frequency of the entire structure. However, depending on the difference between adjacent structures, the effect of local substructure damage on changes in the natural frequency of the entire structure can be limited, and there may be cases where the characteristics of the substructure alone cannot be clearly evaluated. Therefore, if it is possible to directly evaluate the natural frequency of a substructure, it may be possible to judge the health of an entire structure more accurately.

The process of identifying the vibration characteristics of an entire structure and the rigidity of a substructure as a single unit based on the measurement results is called as system identification. System identification is roughly divided into two categories: identification of the modal parameters [5] of the structure such as natural frequencies, damping constants, and mode shapes, and identification of the physical quantities [6-10] that constitute the structure such as mass, stiffness, and damping. This paper focuses on the latter. Methods for identifying physical parameters include methods that identify them in the time domain and methods that identify them in the frequency domain, and various studies have been conducted in the fields of civil engineering and architecture. Examples of time-domain identification methods include research using neural networks [6] and a method of identification using the least-squares method from seismic observation records [7]. On the other hand, test examples of frequency domain identification methods include a study based on the solution of a weighted stiffness sum minimum design problem under the constraint of the first-order eigenvalue [8], a theoretical study for a model of a viscous damping model [9], and a method using the static limit of the transfer function [10]. All of these studies are based on multi-layered structures assuming architectural structures or single-degree-of-freedom models assuming civil engineering structures. A group of continuous bridges and viaducts such as railways has multiple mass points that connect with the ground as described later, and the governing equations are more complicated than in previous studies. However, research to identify physical parameters for the problem has not been sufficiently carried out so far.

We have therefore developed a method for identifying the natural frequency of a substructure [11], which is directly related to the rigidity of the substructure. In this method, a group of bridges and viaducts (Fig. 1(a)), in which multiple superstructures and substructures are connected via superstructures and bearings, is represented by a spring mass model (Fig. 1 (b)), and vibration measurement data is used. The proposed method is an identification method in the frequency domain derived from a theoretical study targeting the free vibration problem. If this method is established, it may be possible to judge the health of the substructure more directly and accurately than the judgment index of the impact and vibration test [3, 4] by using the natural frequency of the substructure. This method is expected to be applied when the health of the substructure is suspected to have deteriorated, for example, due to an earthquake or scouring of a river pier. This paper describes the theoretical development of the method for identifying the natural frequency of substructures and the verification of its validity through numerical analysis.

2. Proposal of natural frequency identification method for a substructure

The theoretical development described in this chapter is performed under the following preconditions:

- Groups of bridges and viaducts behave elastically;
- Frequency dependence of stiffness is not considered;
- Damping has proportional attenuation type characteristics such as Rayleigh attenuation;
- The model boundary is a free end considering half of the superstructure mass outside the model range. This is based on the idea of the design vibration unit [12].

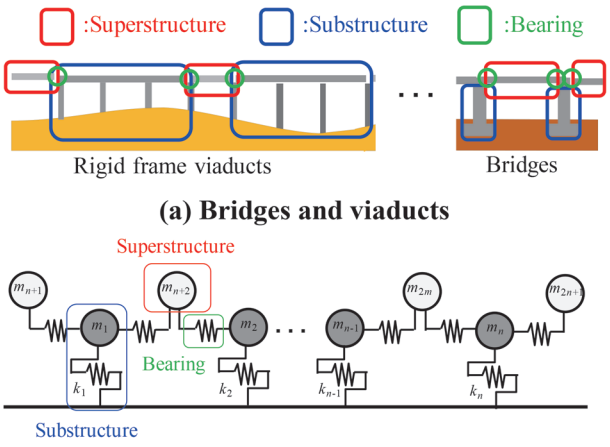

Fig. 1 Image of bridges and viaducts and multi-degrees-of-freedom spring mass model

2.1 Single substructure case

2.1.1 Undamped system

Consider a three-degrees-of-freedom system of a substructure with a superstructure at the start and end points behaving in a free vibration manner (Fig. 2). Let m_1 be the mass of the substructure, k_1 be the stiffness, m_2 be the mass of the superstructure at the start point, k_{12} be the coupled spring stiffness through the bearing, m_3 be the mass of the superstructure at the end point, k_{13} be the coupled spring stiffness through the bearing, and x_1 to x_3 be the displacement waveform of the vibration of each mass point. Here, the masses m_1 to m_3 can be calculated according to the mass that contributes to the vibration after the total mass has been determined from the design documents. This is calculated based on the concept of equivalent mass [13]. In addition, the displacement waveforms x_1 to x_3 can be obtained by performing vibration measurement and obtaining them with a displacement meter, or by obtaining their differential form using a velocimeter or an accelerometer. We consider the problem of identifying the stiffnesses k_1, k_{12}, and k_{13} under this condition.

$$M_3\ddot{X}_3+K_3X_3=0 \tag{1a}$$

$$\boldsymbol{X}_3=\begin{Bmatrix}x_1\\x_2\\x_3\end{Bmatrix},\ \boldsymbol{M}_3=\begin{bmatrix}m_1&0&0\\0&m_2&0\\0&0&m_3\end{bmatrix} \tag{1b}$$

$$\boldsymbol{K}_3=\begin{bmatrix}k_1+k_{12}+k_{13}&-k_{12}&-k_{13}\\-k_{12}&k_{12}&0\\-k_{13}&0&k_{13}\end{bmatrix} \tag{1c}$$

Using the amplitudes r_1 to r_3 of each displacement, the natural circular frequency ω, and the phase angle ϕ, the general solution of the above equation is as follows.

$$\boldsymbol{X}_3=\begin{Bmatrix}r_1\\r_2\\r_3\end{Bmatrix}e^{\pm i(\omega t+\phi)} \tag{2}$$

Substituting equation (2) into equation (1a) and considering the conditions that hold for any time, the following equation holds.

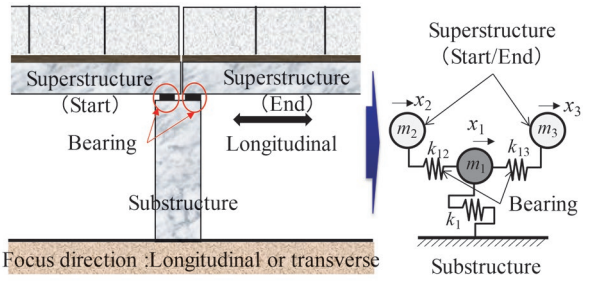

Fig. 2 Free vibration problem of a single substructure

$$(\boldsymbol{K}_3-\omega^2\boldsymbol{M}_3)\begin{Bmatrix}r_1\\r_2\\r_3\end{Bmatrix}=\begin{Bmatrix}0\\0\\0\end{Bmatrix} \tag{3}$$

Here, $\omega=\omega_j$ (j=1, 2, 3, j-th natural circular frequency) can be obtained from the necessary and sufficient conditions for equation (3) to have a non-trivial solution.

$$k_{12}=\frac{m_2\omega^2R_2}{R_2-1},\ R_2=\frac{r_2}{r_1} \tag{4}$$

Rearranging the third line of equation (3) in exactly the same way, the following equation holds.

$$k_{13}=\frac{m_3\omega^2R_3}{R_3-1},\ R_3=\frac{r_3}{r_1} \tag{5}$$

Here, R_2 and R_3 represent the amplitude of the superstructure when the amplitude of the substructure is 1.

Furthermore, substituting equations (4) and (5) into the first line of equation (3) and arranging them, the following equation holds.

$$k_1=(m_1+R_2m_2+R_3m_3)\omega^2 \tag{6}$$

Here, consider the following two extreme examples to understand the meaning of the above equation.

- $k_{12}=k_{13}=0$
- $k_{12}=k_{13}=\infty$

When $k_{12}=k_{13}=0$, it can be seen that $r_2=r_3=0$ because $R_2=R_3=0$ from equations (4) and (5). This is a situation in which the superstructure is not displaced and has no effect on the substructure, which is equivalent to a situation in which the superstructure is not placed. At this time, $k_1=m_1\omega^2$ is obtained from equation (6), and it can be seen that the system is reduced to a single-degree-of-freedom system consisting only of substructure stiffness and mass. On the other hand, when $k_{12}=k_{13}=\infty$, $R_2=R_3=1$, that is, $r_1=r_2=r_3$ can be said from equations (4) and (5). This is a situation in which the superstructure and substructure are completely integrated, and corresponds to the way of handling in the design vibration unit. At this time, $k_1=(m_1+m_2+m_3)\omega^2$ is obtained from equation (6), resulting in a single-degree-of-freedom system with the addition of the superstructure mass.

2.1.2 Damped system

When damping is taken into account, a damping term proportional to velocity is added with the same sign as the restoring force term. Therefore, the equation of motion is as follows:

$$\boldsymbol{M}_3\ddot{\boldsymbol{X}}_3+\boldsymbol{C}_3\ddot{\boldsymbol{X}}_3+\boldsymbol{K}_3\boldsymbol{X}_3=0 \tag{7a}$$

$$\boldsymbol{C_3}=\begin{bmatrix} c_1+c_{12}+c_{13} & -c_{12} & -c_{13} \\ -c_{12} & c_{12} & 0 \\ -c_{13} & 0 & c_{13} \end{bmatrix} \tag{7b}$$

In this paper, we deal with proportional damping, where the eigenmodes are the same real numbers as in the undamped system. At this time, the above general solution becomes the following equation:

$$\boldsymbol{X_3}=\begin{Bmatrix} r_1 \\ r_2 \\ r_3 \end{Bmatrix} e^{\lambda t \pm i\phi},\ \lambda=-\sigma \pm i\omega_D \tag{8}$$

where λ is the eigenvalue, which is represented by the damped natural circular frequency ω_D and the modal damping constant σ of the entire system.

Substituting equation (8) into equation (7a) and considering the conditions that hold for any time, the following equation holds:

$$(\lambda^2\boldsymbol{M_3}+\lambda\boldsymbol{C_3}+\boldsymbol{K_3})=\begin{Bmatrix} r_1 \\ r_2 \\ r_3 \end{Bmatrix}=\begin{Bmatrix} 0 \\ 0 \\ 0 \end{Bmatrix} \tag{9}$$

Focusing on the second line of equation (9), we can obtain the following equation after setting $R_2=r_2/r_1$

$$(-c_{12}\lambda-k_{12})+(m_2\lambda^2+c_{12}\lambda+k_{12})R_2=0 \tag{10}$$

By dividing the above equation into real and imaginary parts, the following equation is obtained:

$$\begin{aligned}&[(R_2-1)k_{12}-(R_2-1)\sigma c_{12}+R_2m_2(\sigma^2-\omega_D^2)]\\&\quad+i\{\pm(R_2-1)\omega_D c_{12}\mp 2m_2\sigma\omega_D R_2\}=0\end{aligned} \tag{11}$$

Real part = imaginary part = 0 is necessary for the above equation to hold, so the following equation holds:

$$\begin{bmatrix} R_2-1 & -\sigma(R_2-1) \\ 0 & \omega_D(R_2-1) \end{bmatrix}\begin{Bmatrix} k_{12} \\ c_{12} \end{Bmatrix}=m_2R_2\begin{Bmatrix} \omega_D^2-\sigma^2 \\ 2\sigma\omega_D \end{Bmatrix} \tag{12}$$

By solving the above simultaneous equations, the coupled spring stiffness k_{12} and damping coefficient c_{12} are obtained by the following equations:

$$\begin{Bmatrix} k_{12} \\ c_{12} \end{Bmatrix}=\frac{m_2R_2}{R_2-1}\begin{Bmatrix} \omega_D^2+\sigma^2 \\ 2\sigma \end{Bmatrix} \tag{13}$$

Also, since the same calculation can be performed for the third line of equation (9), the coupled spring stiffness k_{13} and the damping coefficient c_{13} can be obtained.

$$\begin{Bmatrix} k_{13} \\ c_{13} \end{Bmatrix}=\frac{m_3R_3}{R_3-1}\begin{Bmatrix} \omega_D^2+\sigma^2 \\ 2\sigma \end{Bmatrix},\ R_3=\frac{r_3}{r_1} \tag{14}$$

Next, focusing on the first line of equation (9) and applying the conditions of real part = 0 and imaginary part = 0, the following equation is obtained:

$$\begin{Bmatrix} k_1 \\ c_1 \end{Bmatrix}=(m_1+R_2m_2+R_3m_3)\begin{Bmatrix} \omega_D^2+\sigma^2 \\ 2\sigma \end{Bmatrix} \tag{15}$$

Here, since the damping matrix is assumed to be of the proportional damping type, the damped natural circular frequency ω_D and the modal damping constant σ can be expressed by the following equation using the undamped natural circular frequency ω and the damping constant h

$$\sigma=h\omega,\ \omega_D=\omega\sqrt{1-h^2} \tag{16}$$

By substituting the above equations for equations (13) to (15), the following equations are obtained:

$$\begin{Bmatrix} k_1 \\ c_1 \end{Bmatrix}=(m_1+R_2m_2+R_3m_3)\begin{Bmatrix} \omega^2 \\ 2h\omega \end{Bmatrix} \tag{17}$$

$$\begin{Bmatrix} k_{12} \\ c_{12} \end{Bmatrix}=\frac{m_2R_2}{R_2-1}\begin{Bmatrix} \omega^2 \\ 2h\omega \end{Bmatrix} \tag{18}$$

$$\begin{Bmatrix} k_{13} \\ c_{13} \end{Bmatrix}=\frac{m_3R_3}{R_3-1}\begin{Bmatrix} \omega^2 \\ 2h\omega \end{Bmatrix} \tag{19}$$

It can be seen that k_1, k_{12}, and k_{13} match the undamped solutions (equations (4) to (6)). That is, if the undamped natural circular frequency is used, the solution of the damped vibration problem can be expressed by the same equation as the undamped vibration problem. Note that k_1 in equation (17) has the same form as the stiffness calculation formula for the multi-layered shear spring mass model shown in Reference 8.

2.2 Cases of two or more substructures

Consider the damped free vibration problem in which two substructures are connected via a superstructure and bearings (Fig. 3). The equation of motion for this problem is as follows:

$$\boldsymbol{M_5}\ddot{\boldsymbol{X}}_5+\boldsymbol{C_5}\dot{\boldsymbol{X}}_5+\boldsymbol{K_5}\boldsymbol{X_5}=0 \tag{20}$$

The general solution of the above equation can be expressed in the following form, similar to equation (8):

$$\boldsymbol{X_5}=\begin{Bmatrix} r_1 \\ r_2 \\ r_3 \\ r_4 \\ r_5 \end{Bmatrix} e^{\lambda t \pm i\phi},\ \lambda=-\sigma \pm i\omega_D \tag{21}$$

By substituting the above harmonic vibration solution for the equation of motion and arranging it, the following equation is obtained:

$$\sum_{i=1}^{2}(\lambda C_i+\Omega_i^2)M_iR_i=-\lambda^2\sum_{i=1}^{5}M_iR_i \tag{22}$$

Here, j is the subscript of the substructure of interest (here, 1), and the following formula is defined:

$$C_i=\frac{c_i}{m_i},\ \Omega_i^2=\frac{k_i}{m_i},\ M_i=\frac{m_i}{m_j},\ R_i=\frac{r_i}{r_j} \tag{23}$$

Note that Ω_i corresponds to the natural circular frequency of substructure i. Applying the condition of real part = imaginary part = 0 to equation (22), the following equation is obtained:

$$\sum_{i=1}^{2}\Omega_i^2M_iR_i=\omega^2\sum_{i=1}^{5}M_iR_i \tag{24}$$

$$\sum_{i=1}^{2}C_iM_iR_i=2\sigma\sum_{i=1}^{5}M_iR_i \tag{25}$$

Here, ω is the undamped natural circular frequency. If we check

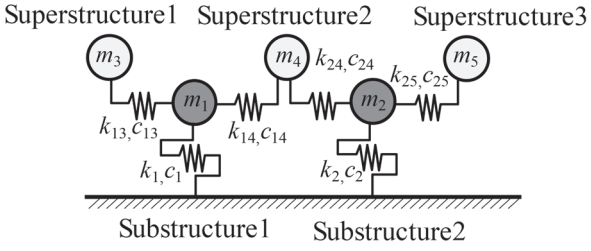

Fig. 3 Free vibration problem of two substructures

equation (24), we can see that Ω_1 and Ω_2 are represented by one equation. In this paper, since the frequency dependence of stiffness is not taken into consideration, Ω_1 and Ω_2 can be uniquely obtained by substituting the two types of undamped natural circular frequency ω and the eigenmode vector. Incidentally, although it is not the subject of this paper, if the modal damping constant σ_i corresponding to each eigenmode can be calculated, it is also possible to calculate the physical quantity C_i related to each damping coefficient from equation (25).

In the spring mass model (Fig. 1(b)), which generally consists of n substructures, the same argument as above can be made, so that the following equation can be obtained in the same way as equation (24).

$$\sum_{i=1}^{n} \Omega_i^2 M_i R_{ji} = \omega_j^2 \sum_{i=1}^{2n+1} M_i R_{ji} \tag{26}$$

For the convenience of the discussion below, we added a subscript to indicate that equation (26) relates to the j-th mode. Since there are n unknowns Ω_i (i=1,2,...n), Ω_i can be uniquely determined if there are n pairs of undamped natural circular frequencies ω_j and eigenmodes R_{ji}.

Considering that R_{11}=M_1=1 when n=1, equation (26) coincides with equation (17) for one substructure, so this expression can be said to be general.

2.3 Use of natural frequency identification method for substructure

The deterioration of health due to damage to a substructure and deterioration of stability mean a decrease in the rigidity of the substructure, that is, a decrease in the natural circular frequency of the substructure itself in the spring-mass model. Therefore, it may be possible to judge the health of a substructure more directly and accurately by using the natural frequency of the substructure than by using the judgment index of the impact and vibration test [3, 4].

As a specific application example of the proposed method, the health diagnosis procedure using the natural frequency of a single substructure is presented here:

- Understand the initial value F_0 of the natural frequency of the substructure. For new structures, the most accurate values are obtained when vibration measurements are performed without the superstructure under construction. For existing structures, vibration measurements are performed at several locations, including the substructure and superstructure to calculate the natural frequency and natural mode of the entire system. Using equation (26), the natural frequency of the substructure can be identified.
- If the health of the substructure is suspected to have deteriorated due to an earthquake or scouring at a river pier, measure the vibration again and identify the natural frequency F of the substructure from equation (26).
- Compare F with F_0, and if there is a significant change such as a decrease in F compared with F_0, it is determined that the health of the substructure has deteriorated.

The above assumes a health diagnosis in the event of an abnormality, but it is also possible to detect the secular change in the natural frequency of the substructure, such as health monitoring. Methods for calculating the natural frequency and natural mode of the entire system from the vibration measurement results include methods using the Fourier amplitude ratio and Fourier phase difference at the dominant frequency, and methods using the Frequency Domain Decomposition method [14].

2.4 Precautions for use with actual railway bridges and viaducts

2.4.1 Reference points for M_i and R_{ji}

As can be seen from the forms of equations (23) and (26), any mass point can be used as a reference for the mass ratio M_i and the eigenmode R_{ji}. The mass ratio can be evaluated according to the mass that contributes to the vibration based on the actual amount obtained from the design documents.

2.4.2 Calculation of undamped natural circular frequency

Strictly speaking, the dominant frequency obtained by Fourier transforming the waveform that can be obtained by actual measurement should match the damped natural frequency. However, the required physical quantity from equation (26) is the undamped natural circular frequency, so its calculation is described below.

Taking the 1st-order mode as an example, the difference $\Delta\omega_1$ between the damped 1st-order natural circular frequency and the undamped 1st-order natural circular frequency is given by the following equation:

$$\Delta\omega_1 = \omega_1 - \omega_{D1} = (1 - \sqrt{1 - h^2})\,\omega_1 \tag{27}$$

When described in terms of frequency, the following equation is obtained:

$$\Delta f_1 = (1 - \sqrt{1 - h^2})\,\frac{f_1}{2\pi} \tag{28}$$

Here, the damping constant h is usually in the range of a few % to 20%, and the natural frequency f_1 is in the range of a few Hz to 10 Hz.

Next, assuming that the actual measurement time is t_N(s), the frequency step size Δf obtained by Fourier transform of the recorded waveform is given by the following equation:

$$\Delta f = \frac{1}{t_N} \tag{29}$$

In normal vibration measurement, the measurement time t_N(s) for a block of Fourier transforms is about several tens of seconds, and the sampling frequency is about 100 to 1,000 Hz. Table 1 shows examples of Δf_1 and Δf. In the table, N is the number of data and f_s is the sampling frequency. In order to know the approximate range of values that can be taken, calculations were made under conditions where Δf_1 and Δf were relatively small and relatively large. Here, the waveform processing assumes the use of fast Fourier transform, so the measurement time is such that the number of data N=f_s×t_N is a power of 2. From this table, it can be seen that Δf_1 and Δf finally become the same order when a structure with a damping constant of 20% and an undamped natural frequency of 10 Hz is measured at a sampling frequency of 1,000 Hz for 65.536 s. These are conditions where Δf_1 is relatively large and Δf is relatively small. Therefore, it can be seen that the difference between the damped natural frequency and the undamped natural frequency is very small and cannot be distinguished by the step size obtained with normal measurement accuracy. In other words, in practice, it can be said that the dominant frequency of the Fourier amplitude spectrum can be determined as the undamped natural frequency as it is.

2.4.3 Calculation of eigenmodes

Taking the case of two substructures as an example, substitut-

Table 1 Examples of Δf_1 and Δf

Example	h	f_1(Hz)	Δf_1(Hz)	f_s(Hz)	N	t_N(s)	Δf(Hz)
1	3%	0.5	3.6×10^{-5}	1000	65536	65.536	1.5×10^{-2}
2	20%	10	3.2×10^{-2}	100	1024	10.24	9.8×10^{-2}

ing the j-th mode and k-th mode values into equation (26) yields the following equation:

$$\begin{bmatrix} 1 & M_2R_{j2} \\ 1 & M_2R_{k2} \end{bmatrix} \begin{Bmatrix} \Omega_1^2 \\ \Omega_2^2 \end{Bmatrix} = \begin{Bmatrix} \omega_j^2(1 + M_2R_{j2} + M_3R_{j3} + M_4R_{j4} + M_5R_{j5}) \\ \omega_k^2(1 + M_2R_{k2} + M_3R_{k3} + M_4R_{k4} + M_5R_{k5}) \end{Bmatrix} \quad (30)$$

Here, the fact that $R_{j1}=R_{k1}=M_1=1$ is used from the definition of equation (23).

In order to solve this simultaneous equation uniquely, the determinant on the left side = $M_2(R_{k2}-R_{j2}) \neq 0$ is a necessary and sufficient condition. This means that the amplitude ratios of substructure 1 and substructure 2 are different in the k-th mode and the j-th mode. In general, a similar argument can be made in the case of n substructures. As a result, unless n modes with different mode shapes are selected when focusing only on the substructure, Equation (30) cannot be solved uniquely, and the natural frequency of the substructure cannot be calculated.

3. Validation of the method based on numerical analysis

In this chapter, the validity of the method proposed in Chapter 2 based on the theoretical development is verified by numerical analysis. Specifically, taking the case of one substructure and the case of three substructures as examples, the proposed method is applied based on the natural frequency and natural mode obtained from numerical analysis to identify the natural frequency of the single substructure. Then, it is compared with the correct value, which is the set value of the analysis model. In addition, the set values of the numerical analysis model dealt with in this chapter include a range that differs from the specifications of the actual railway bridges and viaducts. For example, the natural frequencies of the substructure and the bearing are set in a very close range, but the natural frequency of the bearing is actually assumed to be sufficiently higher than that of the substructure. In addition, although the maximum damping constant is set at 40%, the damping constant that is always exerted is actually around a few percent, and considering the influence of nonlinearity during earthquakes, it is thought to be around 30%. The reason for this setting is that the purpose of this chapter is to verify the validity of the proposed method. The validity of the proposed method is also verified separately assuming actual measurements on an actual bridge [15].

3.1 Single substructure case

For the case of a single substructure, a linear impact vibration analysis was performed, and the effectiveness of the method was verified by calculating the natural frequency of the single substructure using the proposed method (Fig. 4). Table 2 shows the study cases. The mass of the substructure was standardized at 1 ton, and the mass ratio $M_i=m_i/m_1$ to mass point i was varied. In addition, the stiffness of the superstructure-bearing spring and the substructure spring was set by setting the natural frequency F_i of each unit and converting it to $k_i=4\pi^2 m_i F_i^2$. The damping matrix was calculated as stiffness-proportional damping, and the damping constant h was set for the first-order mode of the entire structure. As the impact excitation, a force of 1 kN at time 0.001 s and 0 at other times was applied to mass point 1. The time step was 0.001s and the analysis was performed for 60s. When analyzing the analysis results, it is necessary to exclude the effect of the forced vibration state immediately after the impact, so we focused on the waveform after 5 seconds.

Figure 5 shows the results of Cases 1-3 and 1-5 as examples of the response displacement waveform, the Fourier amplitude spectrum of the response displacement, and the Fourier amplitude spectrum ratio. Here, the Fourier amplitude spectrum is calculated from the attenuation waveform from the point of maximum response displacement after 5 seconds. From this figure, it can be seen that each case oscillates in the first-order mode of the entire system, and that the oscillation waveform transitions on the envelope curve of the set damping constant. Considering these results as actual measurement data, the dominant frequency, damping constant, and Fourier amplitude ratio at that frequency are known. The natural frequency F_1 of the substructure unit to be identified is 2.0 Hz, but it can be seen that this information cannot be determined from the

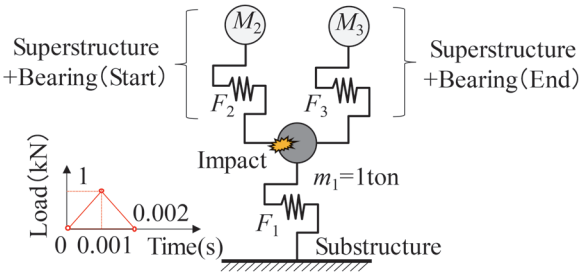

Fig. 4 Image of impact vibration analysis

Table. 2 List of considered cases

Case	M_2	M_3	F_1(Hz)	F_2(Hz)	F_3(Hz)	h
1-1	1	1	2.0	2.0	2.0	0.05
1-2	2	3	2.0	2.0	2.0	0.05
1-3	2	3	2.0	3.3	1.25	0.05
1-4	2	3	2.0	3.3	1.25	0.1
1-5	2	3	2.0	3.3	1.25	0.3
1-6	2	3	2.0	3.3	1.25	0.5

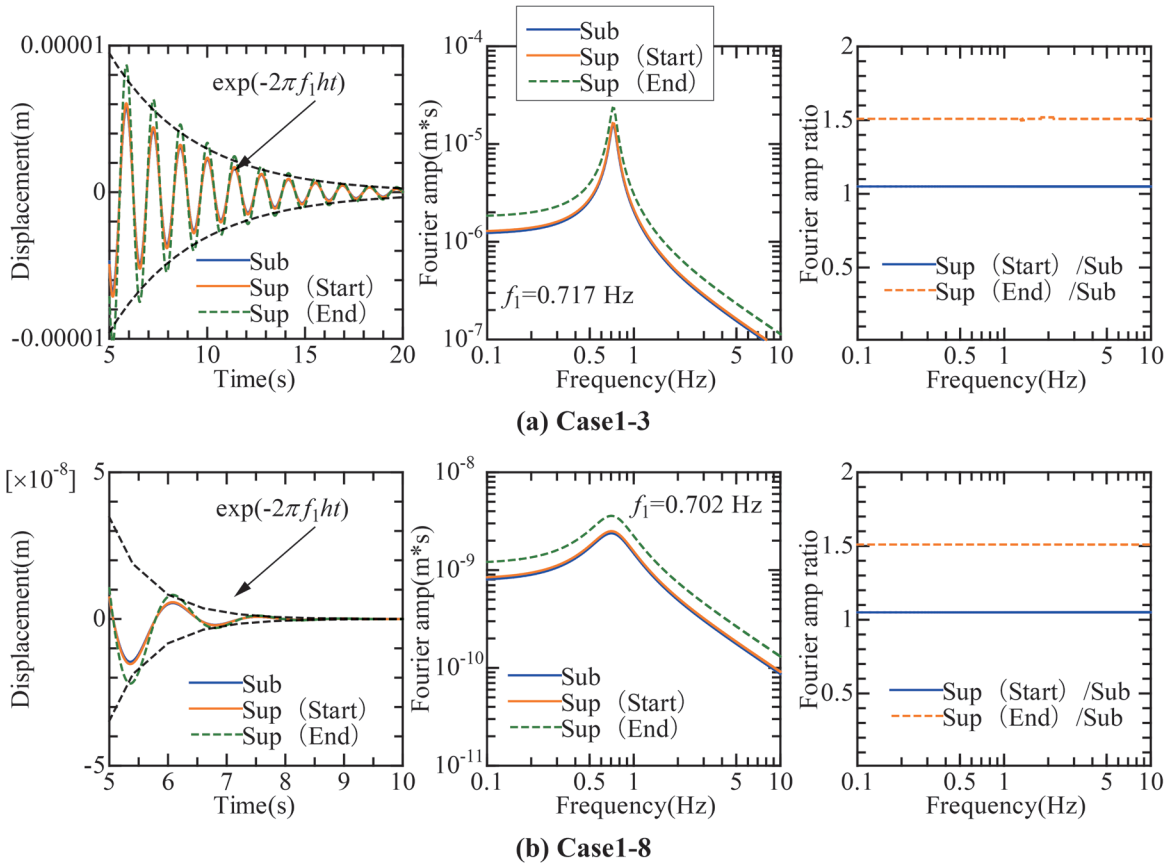

Fig. 5 Response analysis result example (left: displacement waveform, center: Fourier amplitude, right: Fourier amplitude ratio)

Fourier amplitude spectrum.

Table 3 shows the damped natural frequency f_{d1} and undamped natural frequency f_1 obtained from the complex eigenvalue analysis of Cases 1-1 to 1-6, and the dominant frequency f obtained from the Fourier amplitude spectrum of the response waveform. In addition, F (Hz) and F_d (Hz) are shown as the natural frequency converted from the natural circular frequency calculated by Equation (26) from the dominant frequency, damping constant, and Fourier amplitude spectrum ratio. Here, F (Hz) is the result of the calculation assuming that the dominant frequency obtained is the undamped natural frequency, and F_d (Hz) is the result of the calculation assuming that the dominant frequency obtained is the damped natural frequency. Figure 6 shows the relationship between the damping constant and F (Hz) or F_d (Hz). In addition to the cases in Table 2, Fig. 6 also shows the results under the same conditions as Cases 1-3 to 1-6 with damping constants of 1%, 3%, 20%, and 40%. From this table and this figure, in Cases 1-1 to 1-3 with a damping constant of 5%, f_1 and f_{d1} are almost the same, and the correct value of 2.0 Hz can be identified with high accuracy for both F (Hz) and F_d (Hz). However, as the damping constant increases, the accuracy of identifying the natural frequency of the substructure tends to decline, and the deviation is particularly large if the calculation method does not consider damping. This is because f_1 and f_{d1} diverge as the damping constant increases in Cases 1-3 to 1-6 (Table 3). However, if the damping constant is up to about 30%, even the non-attenuation calculation method can estimate the result that is sufficiently close to the correct value of 2.0 Hz. A damping constant of 30% can be said to be a relatively large value considering the reference value of 15 to 30% for the damping constant given to the ground spring described in Design Standards for Railway Structures and Commentary (Seismic Design) [12], so it can be said that there is no problem in calculating the dominant frequency as the undamped natural frequency in practice.

Table 3 Natural frequency of the entire system and single substructure (one substructure)

Case	f_1(Hz)	f_{d1}(Hz)	f(Hz)	F(Hz)	F_d(Hz)
1-1	1.035	1.034	1.038	2.004	2.007
1-2	0.764	0.763	0.763	1.997	2.000
1-3	0.725	0.724	0.717	1.979	1.982
1-4	0.725	0.721	0.717	1.979	1.989
1-5	0.725	0.691	0.702	1.937	2.031
1-6	0.725	0.628	0.626	1.727	1.994

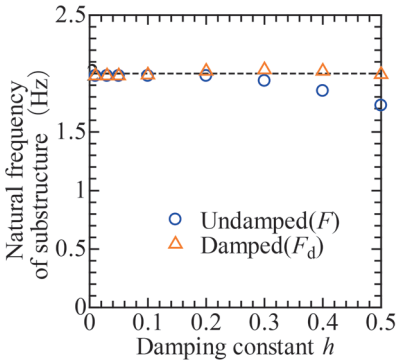

Fig. 6 Relationship between damping constant and natural frequency of substructure identified

3.2 Cases of two or more substructures

If there are two or more substructures, high-order modes of the entire system are required, so it is difficult to excite high-order modes in impact vibration analysis. Since the purpose of this study is to numerically verify the validity of equation (26), the validity is verified by eigenvalue analysis instead of using the results of impact excitation as in the previous section. In the case of real structures, the natural frequency and natural mode of the entire system can be obtained by applying the FDD method [14] based on the results of microtremor observation [16]. Table 4 shows the parameters of the spring mass model considered in this paper. Three cases were set for a seven-degrees-of-freedom model with three substructures (Fig. 7). The method of setting the mass and stiffness is the same as in the previous section. Since the undamped eigenfrequency and eigenmode required for calculation can be obtained by real eigenvalue analysis, damping is not set in this model.

Next, Table 5 shows the 1st to 3rd natural frequencies f and effective mass ratios of Cases 2-1 to 2-3, and Fig. 8 shows the eigenmode diagram of Case 2-3. Looking at the above mode diagram, it can be seen that the amplitude ratios of the substructures 1 to 3 are all different for the 1st to 3rd modes. By using these, it may be possible to calculate the natural frequency of the substructure. It can be seen that the natural frequency of the substructure cannot be determined from the natural frequency of each mode.

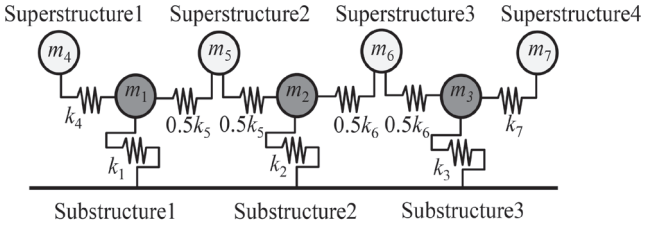

Fig. 7 Verification analysis model

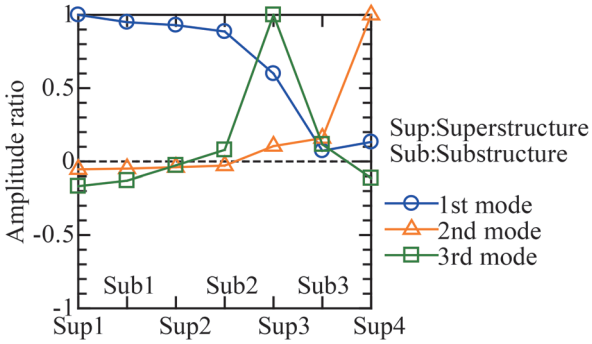

Fig. 8 Natural mode (Case3)

Figure 9 shows the natural frequency of the substructure calculated by Equation (26) using the 1st to 3rd modes of each case. The figure also shows the correct values of the model and that the natural frequency of each case and each substructure can be calculated accurately. From the above, it has been shown that the natural frequency of the substructure can be calculated by the proposed method when the natural frequency and natural mode of several whole systems can be obtained in a group of bridges and viaducts.

4. Conclusions

In this paper, we developed a method to identify the natural frequency of the substructure which is directly related to the rigidity of the substructure. In this method, a group of bridges and viaducts, in which several superstructures and substructures are connected via

Table 4 Verification analysis case

Case	M_2	M_3	M_4	M_5	M_6	M_7	F_1(Hz)	F_2(Hz)	F_3(Hz)	F_4(Hz)	F_5(Hz)	F_6(Hz)	F_7(Hz)
1	1.00	1.00	1.00	1.00	1.00	1.00	2.00	2.00	2.00	2.00	2.00	2.00	2.00
2	1.50	2.00	2.50	0.50	0.75	1.25	2.00	2.00	2.00	2.00	2.00	2.00	2.00
3	1.50	2.00	2.50	0.50	0.75	1.25	2.00	1.20	3.33	5.00	10.00	2.50	1.67

Table 5 Result of eigenvalue analysis

Case	Mode	Natural frequency (Hz)	Effective mass ratio
1	1st	1.15	0.96
	2nd	1.27	0.00
	3rd	1.71	0.01
2	1st	0.99	0.47
	2nd	1.34	0.43
	3rd	1.72	0.03
3	1st	1.12	0.71
	2nd	1.53	0.16
	3rd	2.37	0.02

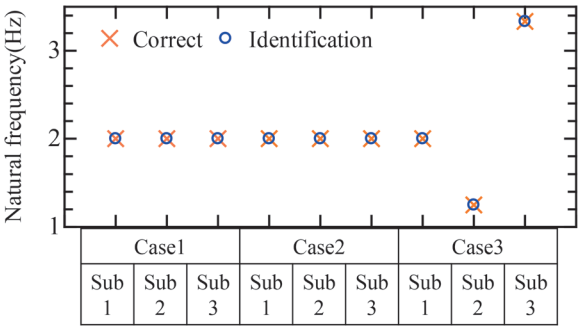

Fig. 9 Identification of natural frequency for a substructure

superstructures and bearings, is represented by a spring mass model, and vibration measurement data is used. The validity of the identification method was then verified by numerical analysis. The findings obtained in this paper are as follows:

- In a system of *n* substructures, it is theoretically proved that the natural frequency of each substructure can be calculated using *n* undamped natural frequencies and natural modes of the whole system.
- In order to verify the validity of the theoretical formula obtained as a general solution, the proposed method was applied based on the results of linear impact vibration analysis and eigenvalue analysis for the cases of one substructure and three substructures. The result shows that the natural frequency of the substructure can be identified with high accuracy.
- If the damping constant is within the range assumed for railway bridges and viaducts, the dominant frequency of the response waveform and the undamped natural frequency are almost the same. Therefore, in practice, the proposed method can be applied using the dominant frequency of the response waveform.

In addition, although not described here due to space limitations, we separately performed an evaluation of the impact on the identification accuracy when the data contains errors and a validity check of the proposed method assuming actual measurements on a real bridge.

References

[1] Nakajima, A., Nakano, K. and Nakamura, S., "Vibrational property of independent piers and completed bridge by using microtremor measurement," *Journal of Structural Engineering*, Vol. 56A, pp. 305-314, 2010 (in Japanese).

[2] Tokunaga, M., Sogabe, M., Tanimura, H. and Ono, K., "Method for evaluating equivalent natural period with microtremor measurement," *Proceedings of JSCE* A1, Vol. 71, No. 1, pp. 72-86, 2015 (in Japanese).

[3] Nishimura, A. and Tanamura, S., "A study on integrity assessment of railway bridge foundation," *RTRI Report*, Vol. 3, No. 8, pp. 41-49, 1989 (in Japanese).

[4] Nishimura, A., "A study on integrity assessment of railway rigid frame bridge," *RTRI Report*, Vol. 4, No. 9, pp. 14-21, 1990 (in Japanese).

[5] Saito, T., "System identification of a high-rise building applying multi-input-multi-output ARX model of modal analysis," *J. Struct. Constr. Eng., AIJ*, No. 508, pp. 47-54, 1998 (in Japanese).

[6] Sato, T. and Kikukawa, M., "A linear algorithm to identify the non-linear structural system equations," *Proceedings of JSCE*, No. 584/I-42, pp. 175-184, 1998 (in Japanese).

[7] Ikeda, Y. and Hanafusa, H., "Direct identification of stiffness for flexural-shear building model based on earthquake observation," *J. Struct. Constr. Eng., AIJ*, Vol. 79, No. 705, pp. 1601-1611, 2014 (in Japanese).

[8] Nakamura, T. and Yamane, T., "Optimum design and earthquake response constrained design of elastic shear buildings," *Earthquake Engineering and Structural Dynamics*, Vol. 14, pp. 797-815, 1986.

[9] Udwadia, F. E., Sharma, D. K. and Shah, P. C., "Uniqueness of Damping and Stiffness Distributions in the Identification of Soil and Structural Systems," *Journal of Applied Mechanics*, ASME, Vo. 45, pp. 181-187, 1978.

[10] Nakamura, M., Takewaki, I., Yasui, Y. and Uetani, K., "Simultaneous identification of stiffness and damping of building structures using limited earthquake records," *J. Struct. Constr. Eng., AIJ*, No. 528, pp. 75-82, 2000 (in Japanese).

[11] Wada, K. and Sakai, K., "Natural frequency identification method for a substructure in bridges and viaducts," *Proceedings of JSCE* A2, Vol. 77, No. 2, I_25-I_34, 2021 (in Japanese).

[12] Railway Technical Research Institute, *Design Standards for Railway Structures and Commentary (Seismic Design)*, Maruzen, 2012 (in Japanese).

[13] Railway Technical Research Institute, *Design Standards for Railway Structures and Commentary (Seismic Design)*, Maruzen, 1999 (in Japanese).

[14] Brincker, R., Zhang, L. and Anderson, P., "Modal identification from ambient response using frequency domain decomposition," *Proceedings of 18th International Modal Analysis Conference*, San Antonio, Texas, pp. 625-630, 2000.

[15] Wada, K. and Sakai, K., "Verification of natural frequency identification method for a substructure in railway bridges and viaducts," *Journal of railway engineering*, *JSCE*, Vol. 27, 2023 (in Japanese).

[16] Chen, P. Y., Iiyama, K., Morikawa, H., Sakai, K., and Kitamura, H., "A study on modal characteristic of elevated bridge in different construction stage," *The 39th JSCE Earthquake Engineering Symposium*, 2019.

Authors

Kazunori WADA, M.Eng.
Assistant Senior Researcher, Structural Dynamics and Response Control Laboratory, Center for Railway Earthquake Engineering Research
Research Areas: Earthquake Engineering

Kimitoshi SAKAI, Dr.Eng.
Senior Chief Researcher, Head of Structural Dynamics and Response Control Laboratory, Center for Railway Earthquake Engineering Research
Research Areas: Earthquake Engineering

Numerical Analysis of Local Scour Around Piers Based on 3D Movements of Sediment Particles

Hidenori ISHII **Kohei MUROTANI** **Koji NAKADE**
Computational Mechanics Laboratory, Railway Dynamics Division

This paper describes a numerical model developed to simulate the flow and scour around bridge piers. The flow is modeled by large eddy simulation. The morphological change of riverbeds is calculated by coupling sediment transport with models for sediment pick-up and deposition. The sediment transport is calculated by 3D momentum equations of sediment particles. Sediment pick-up and deposition are modeled by stochastic models for the purpose of reducing computational demand. The numerical model was applied to the local scour around a vertical cylinder pile under clear water condition. The results agreed well with experimental data, except for the shape of the downstream riverbed. It is concluded that this model can evaluate local scour on the upstream side of piers considering 3D movements of sediment particles.

Keywords**:** *local scouring, river pier, scour analysis, coupled analysis, LES*

1. Introduction

Recent years have seen frequent large-scale floods due to intensifying rainfall caused by changes in global-scale meteorological conditions. Such large-scale flooding has resulted in the scouring of the areas around river-bridge piers, which can cause damage such as subsidence and tilting of bridge piers [1, 2]. Many railway river bridges were built in the pre- and post-war periods, and further damage to railway river bridges is expected over time, creating a need for the development of rational scouring depth prediction methods and scouring prevention measures.

Many studies have been conducted on riverbed deformation analysis around hydraulic structures due to its importance in terms of disaster prevention. In recent years, there has been progress in the development of riverbed deformation analysis using three-dimensional fluid computations.

Roulund et al. [3] calculated the flow field using the k-ω SST model in the turbulence model, where they conducted riverbed deformation analysis around a circular pile using the riverbed deformation model based on the bed load formula and sediment transport continuity equation, which take into account the effect of the riverbed slope. Baykal et al. [4] used the model of Roulund et al. [3] with a suspended load movement model in order to analyze the riverbed deformation around a circular cylinder. Their results showed that the scouring depth was approximately double that in the model that considered the suspended load movement.

Nagata et al. [5] combined bed load movement computation using a two-dimensional equation of motion and a stochastic model for sediment pick-up and deposition to propose a riverbed deformation analysis method. Nagata et al. [5] used this method to analyze riverbed deformation around a circular cylinder and reproduced the characteristics of the scouring hole shape obtained in experiments. Ota et al. [6] incorporated a stochastic model for the transition process from bed load to suspended load in the analysis method to propose a riverbed deformation analysis method that considers the sediment entrainment to the suspended load, and this was applied to the scouring upstream of structures in the transverse direction of the river. The results of these analyses generally reproduced the characteristics of the scouring shape but tended to underestimate the maximum scouring depth. Ota et al. [6] stated that the effect of local flow needed to be considered when setting the coefficients of the transition model to suspended load in order to address the underestimation of the maximum scouring depth.

A characteristic of the above-mentioned riverbed deformation analysis [3-6] is that sediment movement related to riverbed deformation is treated separately between bed load and suspended load. Bed load movement is treated as a movement in two dimensions in a thin layer near the riverbed surface, and suspended load movement is either ignored or treated as an advection-diffusion phenomenon.

Meanwhile, Sekine et al. [7] used a three-dimensional equation of motion to compute the bed load and suspended load movement collectively, and they conducted a study to systematically evaluate their characteristics. In their results, they clarified that there were types of motion that were different from the conventional classification depending on the range of the tractive force, and they indicated the limitations of the conventional theory.

A future goal of the riverbed deformation analysis constructed in this study is to be able to conduct scouring analysis under conditions where multiple structures are impacted and under conditions where there are scouring countermeasures such as foot protection blocks. Sediment movement is expected to be more three-dimensional under such conditions, with movement having frequent transitions between bed load and suspended load. It is difficult to say that conventional computations that distinguish between bed load and suspended load movement can sufficiently express the three-dimensional sediment movement in which there are frequent transitions in the movement patterns. Therefore, we adopted the LES turbulence model, which excels in reproducing the unsteady vortex structure in the water flow, in this study for the flow computation; and we developed a riverbed deformation analysis method similar to Sekine et al. [7] that collectively computes the bed load movement and suspended load movement using a three-dimensional equation of motion. For sediment pick-up and deposition, we adopted a stochastic model similar to that in Nagata et al. [5] in order to reduce the computational cost and to enable the analysis of long-term phenomena in a realistic computational time. With this method, we expect to be able to reflect the movement of sediment on the actual grain size scale in riverbed deformation computations with a computational amount that can be applied to three-dimensional flow fields such as around bridge piers without using the coarse-graining method. As the first step in verifying the validity of this method, we conducted a reproduction analysis of a scouring experiment [8] around a single circular pile conducted under static scouring conditions without sediment movement in an undisturbed area upstream of the pier.

2. Analysis method

In this study, we constructed a riverbed deformation analysis method that couples fluid computations using the LES turbulence model and riverbed deformation computations based on three-dimensional sediment movement. In this section, we describe in detail the methods of fluid computation and riverbed deformation computation.

2.1 Fluid computation

For the fluid computation, we used an air flow simulator [9], where non-equidistant rectangular grids are set using the finite difference method, and which is being developed by the Railway Technical Research Institute. The Navier-Stokes equation for incompressible fluids is the basic equation. A three-dimensional Cartesian coordinate system is used as the coordinate system, here the x direction is the downstream direction, y direction is the transverse direction of the river, and z direction is the vertical direction. Turbulence computations were conducted with LES. When the representative velocity was set as U, characteristic length set to L, water density set to ρ_l, kinematic viscosity coefficient set to v, and the Reynolds number $Re = UL/v$, then the basic equations of the dimensionless LES are as shown in (1) and (2):

$$\frac{\partial u_j}{\partial x_j} = 0 \tag{1}$$

$$\frac{\partial u_i}{\partial t} + \frac{\partial u_i u_j}{\partial x_j} = -\frac{\partial p}{\partial x_i} + \frac{1}{Re}\frac{\partial^2 u_i}{\partial x_j \partial x_j} - \frac{\partial \tau_{ij}}{\partial x_j} + G_i \tag{2}$$

where $u_i = (u, v, w)$ is the dimensionless grid-scale velocity, p is the dimensionless pressure, and G_i is the dimensionless gravitational acceleration term. τ_{ij} is the residual stress in the flow with coarse grains as a result of the spatial filter, and it is modeled in the LES computation as a sub-grid scale model (SGS model). The SGS model used the coherent structural Smagorinsky model. Time progression was done using the Adams-Bashforth method with third-order accuracy, and spatial differences were done using the central difference method with second-order accuracy. The cylindrical pile and riverbed shapes were expressed using the voxel method, which discriminates between fluids and solids in units of computational grids. The Froude number Fr for the reproduction analysis was small at 0.143 (computed from average flow velocity U_0=0.171 m/s and average water depth h_0=0.146 m), so it was assumed that the effect of water height difference was small, and rigid lid conditions were applied for the water surface. Slip conditions were applied to the sides of the analysis domain, and non-slip conditions were applied to the solid wall surfaces. Additionally, the grain size of the riverbed material that is subject to reproduction analysis is small and the non-dimensional roughness height is within a range that can be treated as a smooth surface, so the riverbed surface was assumed to be a smooth surface with no slip.

2.2 Riverbed deformation computation

The riverbed deformation computation in this study involves the computation of sediment movement by a three-dimensional equation of motion of point masses, and this is combined with a stochastic model for sediment pick-up and deposition of the bed load in order to compute the riverbed deformation amount.

2.2.1 Sediment pick-up

The sediment pick-up amount is calculated by the following equation using the pick-up rate p_s:

$$V_p = \frac{A_3 d}{A_2} p_s S_P \tag{3}$$

where V_p is the volume of removed sediment from the computational grid per unit time, d is the riverbed material grain size, A_2 and A_3 are the two-dimensional and three-dimensional shape coefficients (=π/4, π/6), and S_p is the area of the computational grid at the departure point. The pick-up rate p_s was calculated by the Nakagawa-Tsujimoto-Murakami equation [10], which is a pick-up probability equation using the dimensionless shear stress and local riverbed slope.

The dimensionless shear stress τ_* of the riverbed bottom was calculated with the following equation using the dynamic pressure gradient in the riverbed vicinity, referencing Marsooli et al. [11], after considering the fact that the dynamic pressure gradient exerts a pressure gradient force on the riverbed sediment:

$$\tau_* = \frac{|\tau_b|}{(\rho_s - \rho_l) g d} \tag{4a}$$

$$\tau_{b,j} = \mu \frac{u_{b,j}}{dz} - \frac{A_3 d}{A_2}\frac{\partial p_d}{\partial \vec{e}_{b,j}} \tag{4b}$$

where τ_* is the dimensionless shear stress, ρ_s is the sediment particle density, $\vec{e}_{b,j}$ is the unit vector parallel to the local riverbed surface on the $x-z$ and $y-z$ planes, $\tau_{b,j}$ is the corrected shear stress in the j-direction, $u_{b,j}$ is the j-direction component of the flow velocity parallel to the local bed surface at the velocity evaluation point of the cell closest to the bed, μ is the viscosity coefficient, dz is the distance from the riverbed surface to the cell closest to the riverbed, and p_d is the dynamic pressure at the cell nearest the riverbed.

2.2.2 Sediment movement

A tracked particle with information on the pick-up amount is generated on the riverbed surface of the computational cell, and the movement path is computed. The method by Nagata et al. [5] and Ota et al. [6] used two-dimensional equations of motion to compute the movement paths of the tracked particles, and the movement path of the bed load was reflected in the riverbed deformation analysis. Meanwhile, in this method, we computed the movement of the tracking particles as three-dimensional motion, which enabled us to reflect the movement paths of not only the bed load but also the suspended load in the riverbed deformation analysis. The following equation was used for the equation of motion of the tracked particles, as in Sekine et al. [7]:

$$\begin{aligned}\rho_l\left(\frac{\rho_s}{\rho_l} + C_M\right) A_3 d^3 \frac{d\vec{u}_p}{dt} &= \rho_l\left(\frac{\rho_s}{\rho_l} - 1\right) A_3 d^3 \vec{g} \\ &+ \frac{1}{2}\rho_l C_D A_2 d^2 |\vec{u} - \vec{u}_p| (\vec{u} - \vec{u}_p) \\ &+ \rho_l (1 + C_M) A_3 d^3 \frac{d\vec{u}}{dt} \\ &+ \frac{1}{2}\rho_l C_L A_2 d^2 \left[|\vec{u}_{r,xy}|_T^2 - |\vec{u}_{r,xy}|_B^2\right] \vec{e}\end{aligned} \tag{5}$$

where $\vec{u}_p = (u_p, v_p, w_p)$ is the moving velocity vector of the tracked particle, $\vec{u} = (u, v, w)$ is the water velocity vector, $\vec{u}_r = (u_r, v_r, w_r)$ is the

relative velocity vector, $\vec{g}$ is the gravitational acceleration vector, $\vec{e}$ is the unit vector of the component, (0,0,1) C_M is the added mass coefficient (=0.5), C_D is the drag coefficient, and C_L is the lift coefficient (=0.2). The drag coefficient C_D was evaluated by the following equation using the particle Reynolds number $Re_p = |\vec{u}_r|d/\nu$:

$$C_D = \frac{24}{Re_p} + \frac{3}{\sqrt{Re_p}} + 0.34 \tag{6}$$

The fourth term on the right side of (5) indicates the lift force due to the velocity gradient around the sediment particle, $\vec{u}_{r,xy}$ is the relative velocity vector $\vec{u}_{r,xy} = (u_r, v_r, 0)$) where the vertical direction component is removed, and the subscripts T and B refer to the top and bottom points of the sphere, respectively.

When the tracked particles approach the vicinity of the riverbed surface, the simulated riverbed particles are placed on the riverbed along with the movement path of the tracked particles, and when the tracked particles collided with the riverbed particles, the inelastic collision process was computed, and the velocity of the tracked particles following collision was computed. When arranging the simulated riverbed particles, we referenced the study by Sekine and Kikkawa [12] to arrange the simulated riverbed particles so that the height distribution of the simulated riverbed particles around the mean riverbed surface follows a normal distribution with a standard deviation $\sigma_z = d/3$.

The movement path computation does not consider the impact of interference between tracked particles or the impact of sediment concentration on each coefficient. We state here that the extent to which these factors impact the results of the phenomena subject to analysis in this study is still subject to debate.

2.2.3 Determination of transition to suspended load

Ota et al. [6] determined the transition from a bed load to suspended load based on a stochastic model. Meanwhile, in this method, we defined the bed load layer thickness based on the study by Sekine et al. [13] on the maximum jumping height of the bed load, and we determined the transition from bed load to suspended load based on the three-dimensional motion of the tracked particles. The bed load layer thickness T obtained from the maximum jumping height of the bed load is computed by the following equation:

$$T = (1 + h_s)\, d, \qquad h_s = A_b \left(\frac{\tau_*}{\tau_{*c}} - 1 \right)^m \tag{7a,b}$$

where τ_{*c} is the dimensionless critical shear stress. Additionally, A_b, m is a constant value, and we adopted the values of 1.42 and 0.64, which were proposed by Sekine et al. [13].

We determined a transition to suspended load when the tracked particle moved to the outside of the bed load layer. The deposition computation by the bed load deposition probability model described in the next section was not conducted for tracked particles that have transitioned to suspended load. We continued to conduct computations based on the equation of motion described in the previous section even after the transition to suspended load, and we assumed that the entire sediment quantity was deposited at the point when it re-attached to the riverbed surface.

2.2.4 Computation of bed load sediment deposition amount

When the sediment pick-up amount at computation point j is set as $V_{p(j)}$, then the deposition amount $V_{d(j,n)}$ per unit time at the position n steps after departure of the tracked particle departing from this point is obtained by the following equation:

$$V_{d(j,n)} = V_{p(j)}\, f_s(S_{(n)})\, \Delta s \tag{8a}$$

$$f_s(S_{(n)}) = \frac{1}{\lambda} \exp\left(-\frac{S_{(n)}}{\lambda} \right) \tag{8b}$$

$$S_{(n)} = \sum_{i=0}^{n} \Delta t\, |\vec{u}_{p(i)}| \tag{8c}$$

where $V_{p(j)}$ is the pick-up amount (initial volume), $f_s(S_{(n)})$ is the probability density function of the step length, $S_{(n)}$ is the cumulative movement distance of the particles, λ is the average step length, $\vec{u}_{p(i)}$ is the velocity vector of the tracked particle at the i^{th} step, and Δt is the time step size. The average step length λ is calculated by the Einstein equation [14], which takes into account the variation in lift force.

This method involves the computation of the deposition amount on the movement path of the tracked particle, so the computed position of the deposition amount does not match the computation grid points. Therefore, the sediment deposition amount was distributed by weighting the distance to the computational grid center points near the tracked particles.

Tracking was terminated when the deposition amount $V_{d(j,n)}$ per unit time evaluated in (8) and the sediment volume of the tracked particle were less than the volume of one sediment grain of the riverbed material (= $\pi d^3/6$).

2.2.5 Riverbed height deformation computation

The temporal change in riverbed height was obtained by the following equation using the sediment pick-up amount and deposition amount per unit time:

$$\frac{\partial Z_b}{\partial t} = \frac{A_1 A_2}{A_3} \frac{(V_d - V_p - V_s)}{S_d} \tag{9}$$

where Z_b is the riverbed height, A_1 is the one-dimensional sediment grain shape factor (=1.0), V_s is the sliding-induced movement amount, and S_d is the vertically projected area of the computational grid.

Local scouring phenomena in the vicinity of structures involves the formation of slopes with steep riverbed gradients in scouring holes as scouring in the vicinity of the structures progresses. When the local riverbed gradient θ_b exceeds the critical gradient angle θ_{bc}, then this results in slide failure (so-called "sliding") of the riverbed slope sediment. Therefore, in this study, the slope failure model of Sekine [15] was used to compute the sediment movement amount V_s when $\theta_b > \theta_{bc}$. The angle of repose of sand in water was used for θ_{bc}. It was assumed that the movement of sediment due to sliding was instantaneous, and the sliding-induced sediment movement amount V_s was added to the pick-up amount V_p of the computational grid where the sliding occurs.

3. Application of analysis method

3.1 Computation case

We conducted a reproduction analysis of the scouring experiment around a cylindrical pile conducted by Umeda et al. [8] in order to verify the validity of this method. Figure 1 shows an overview of the experiment by Umeda et al. [8]. The experiment was conducted in a water channel with a length of 12 m, width of 0.4 m, depth of 0.4 m, and gradient of 1/1000. A 1.65-m long movable bed was set up in the middle of the water channel, and sediment was spread to a

thickness of 0.135 m. The front and rear of the movable bed were raised with acrylic plates so that they would be level with the sand surface. We installed a plastic cylindrical model with a diameter of D = 32 mm in the center of the movable bed. We used sediment with properties of d_{50}=0.139 mm, d_{60}/d_{10}=1.78, and specific gravity of 2.65 for the sediment in the movable bed. Water was flowed upstream at a rate of Q =9.985 L/s, with an average water depth h_0 of 0.146 m and average flow velocity U_0 of 0.171 m/s. The Froude number Fr was 0.143, and the Reynolds number Re_c with respect to the cylindrical pile diameter was 4560. The experiment was carried out under clear water condition. Water was allowed to flow for 620 minutes.

The analysis conditions are shown below. After we confirmed that the positions of the inflow and outflow boundaries did not significantly impact the flow computation, we set an area with a length of 4.65 m, width of 0.4 m, and height of 0.281 m, shown in the red frame in Fig. 1, as the analysis area. The minimum grid near the riverbed in the vicinity of the cylindrical pile was set as a cube with a side length of 1.0 mm, and we set unequally spaced grids with 750 grids in the x direction (downward flow direction), 260 grids in the y direction (transverse direction), and 128 grids in the z direction (vertical direction). The origin of the $x-y$ coordinates was the position of the center of the cylindrical pile model, and the initial riverbed surface was set as z =0.0 m. The inflow boundary was fixed at U_0=0.171 m/s, and the outflow boundary was set as the convective outflow condition. The time step was set as a dimensionless time interval Δt =0.0002 (real time equivalent Δt_{real}=0.00117 s). First, we only conducted fluid computation with the initial value set to a uniform flow, and once a flow was sufficiently developed, we started the coupled computation of the fluid computation and riverbed deformation computation. The sediment constituting the movable bed was set as particles with a uniform size of d =0.139 mm, and the dimensionless critical shear stress τ_{*c} was computed by Iwagaki's empirical equation [16]. The paper by Umeda et al. [8] did not include information on the underwater angle of repose, so the underwater angle of repose was estimated as 32° based on the shape of the scouring hole after the experiment, and this was reflected in the analysis conditions.

Using this method to generate tracked particles at all steps and tracking them is extremely difficult in terms of computational time and computer memory constraints. Therefore, in this study, we decided to generate tracked particles every 100 steps (real time equivalent of every 0.117 s). The tracked particle movement / deposition and riverbed deformation computation were conducted alternately with fluid computation at each step. Tracking was stopped and the particle deleted when the tracked particle moved out of the movable bed area in Fig. 1.

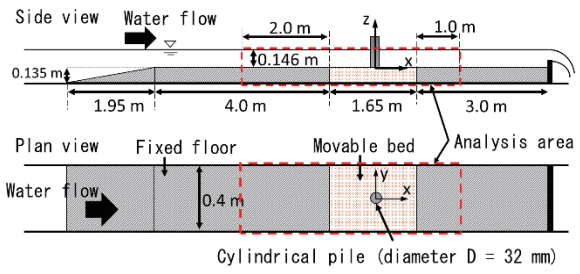

Fig. 1 Experiment overview diagram

3.2 Computational results

Figure 2 shows the analysis results of the flow velocity distribution and streamlines of the longitudinal cross-section (on the water channel centerline) on the upstream side of the cylindrical pile at 600 minutes of water flow. The color contour of the flow velocity distribution is dimensionless at an average flow velocity of 0.171 m/s on the upstream side. From Fig. 2a–b, a horseshoe-shaped vortex was formed, and the flow velocity on the riverbed surface increased, with many pick-ups seen in this area. Meanwhile, in Fig. 2b–c, the flow velocity at the riverbed surface was small, so there were few pick-ups, and there was sliding according to the underwater angle of repose as the hole made by scouring expanded.

Figure 3 shows a comparison of the experimental results and analysis results of the riverbed surface displacement after 620 minutes of water flow. The upper half of Fig. 3 shows the experimental results, and the lower half shows the analysis results. The left side of Fig. 3 shows the upstream side, and the right side shows the downstream side. The scouring hole in the analysis results has an inverted conical shape that is similar to the experimental results shown in Umeda et al. [8], and the scouring depth was a maximum from the cylindrical pile upstream shoulder to near the cylindrical pile front surface. The analysis results agreed well with the experimental results for the scouring range on the upstream side of the cylindrical pile as well. Meanwhile, on the downstream side of the scouring hole, though there was the temporary formation of a deposition area, the turbulent flow behind the cylindrical pile picked up the sediment grains and moved them downstream, and a deposition area seen in

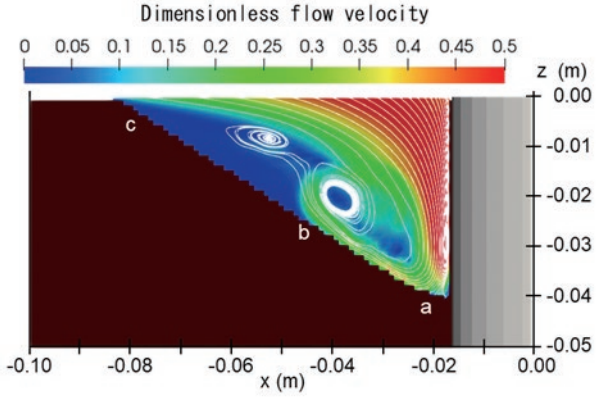

Fig. 2 Flow velocity distribution and streamlines in longitudinal cross-section of cylindrical pile at 600 minutes of water flow

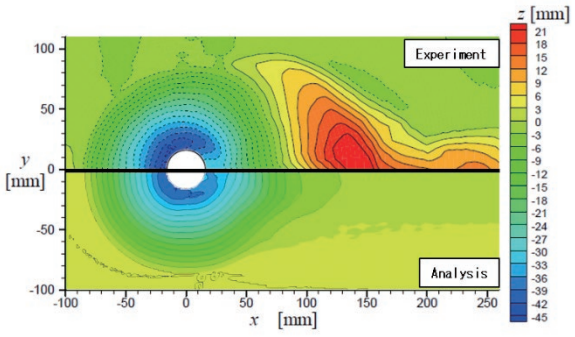

Fig. 3 Comparison of experimental results [8] (top) and analysis results (bottom) of riverbed surface displacement after 620 minutes of water flow

the experiment was not reproduced as a result. This is thought to be due to the lack of reproducibility of the flow field in the wake of the cylindrical pile. The lack of consideration of the turbulence field around the structure in the average step length equation in the deposition model may also be a factor behind this error. The lack of consideration of the impacts of interference between tracked particles and sediment concentration on the sediment movement path computations may also have been a factor. However, although the deposition area was not reproduced, the extent of the scouring, which is important in bridge pier stability computation, was well reproduced, and it is thought that useful results were obtained from this method.

Figure 4 shows the change in scouring depth over time. (a) shows the scouring depth at the cylindrical pile front surface, and (b) shows the scouring depth at the cylindrical pile upstream shoulder. The black squares show the experimental results, and the red lines show the analysis results. The analysis results reproduced the increasing trend in scouring depth for both the cylindrical pile front surface and shoulder well, and the error in scouring depth at around 600 minutes of water flow was within 10% for both the front surface and shoulder.

Figure 5 shows the five-second trajectory of the tracked particles that were picked up at the cylindrical pile front surface (position a in Fig. 5) at 100 minutes of water flow. Blue and green show the tracked particle bed load and suspended load states, respectively. The tracked particles that were picked up at the cylindrical pile front surface moved upstream while repeatedly coming into contact with the riverbed (Fig. 5a–b). The tracked particles transitioned to suspended load by being lifted by the upward flow of the horseshoe vortex halfway up the slope on the upstream side (Fig. 5b–c) and moved downstream from the transition position as suspended load under the influence of water flow (Fig. 5c–f). This type of sediment movement at the cylindrical pile front surface was also reported in the experiments by Umeda et al. [8], and we were able to reproduce the characteristics of the experimentally observed three-dimensional sediment movement with the present method.

Figure 6(a) shows the sediment pick-up amount (cumulative value) for 10 minutes from 100 minutes of water flow, (b) shows the amount that transitioned to suspended load (cumulative value), and Fig. 7 shows the vertical direction component (time-averaged value) of the dimensionless flow velocity at the cell closest to the riverbed. In Figs. 6 and 7, the white lines indicate the positions where the riverbed surface is z = 0.0 m. As shown in Fig. 6(a), sediment pick-up was often observed at the cylindrical pile upstream shoulder and in the middle of the scouring hole. The radial distribution is thought to be sediment pick-up due to the sliding model. Figure 6(b) shows that there were many transitions from the cylindrical pile upstream shoulder to the cylindrical pile side. There was also an area with a large transition volume distributed concentrically from the middle of the scouring hole to the outer edge. When considering the particle trajectories in Fig. 5 and the vertical flow velocity distribution in Fig. 7, it is expected that the sediment particles moving on the scouring hole slope are lifted by the upward flow near the bottom and transition to suspended load.

4. Conclusion

In this study, we constructed a riverbed deformation analysis method that integrates bed load and suspended load for computa-

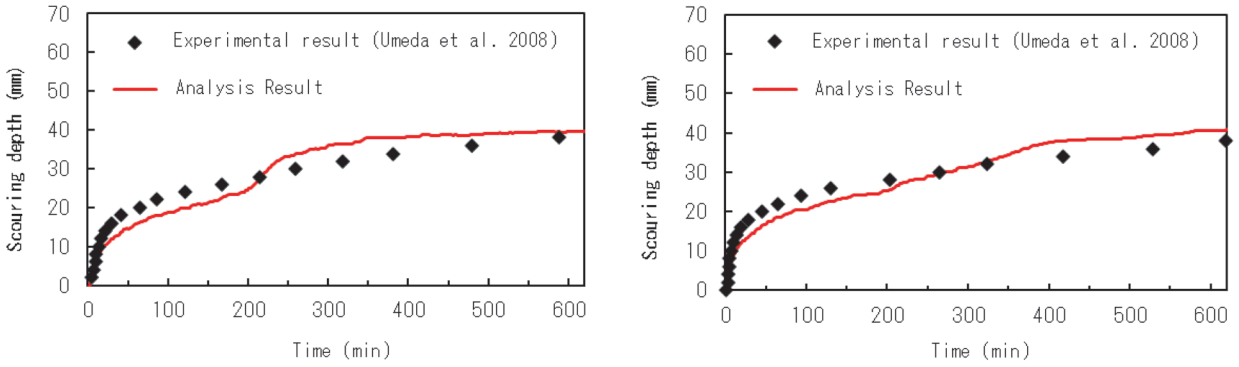

(a) Cylindrical pile upstream front surface (x= -0.017 m, y= 0.000 m)

(b) Cylindrical pile upstream shoulder (x= -0.012 m, y= 0.012 m)

Fig. 4 Temporal change in scouring depth

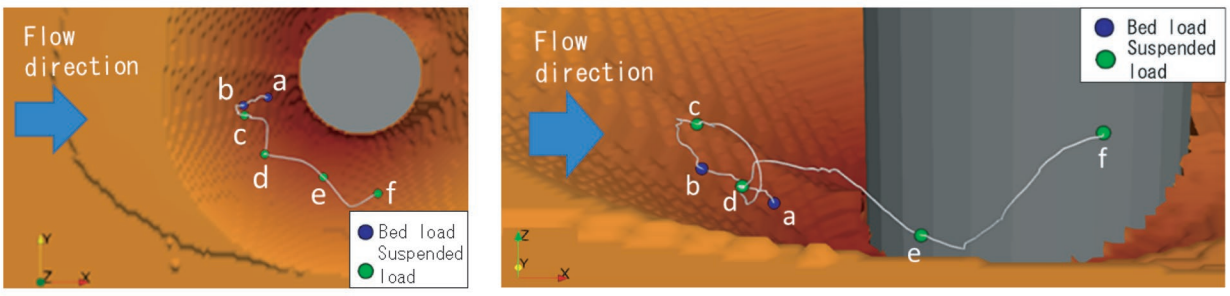

(a) From upper side of cylindrical pile

(b) From side of cylindrical pile

Fig. 5 Trajectory of sediment particles picked up from cylindrical pile front surface

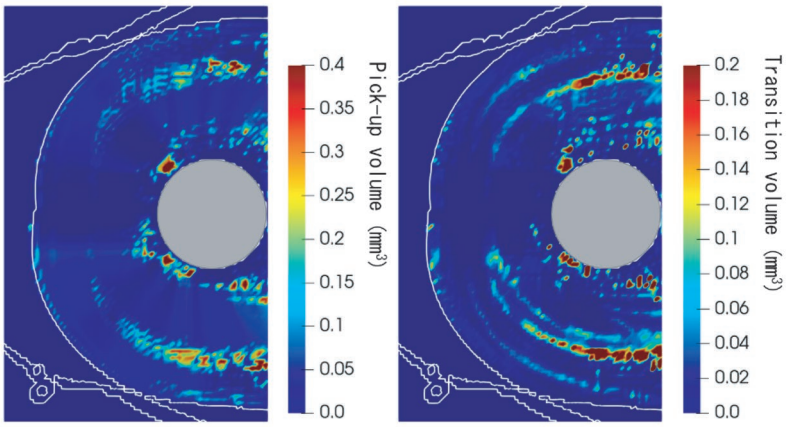

(a) Sediment pick-up amount

(b) Amount transitioning to suspended load

Fig. 6 Sediment pick-up amount / amount transitioning to suspended load (cumulative value)

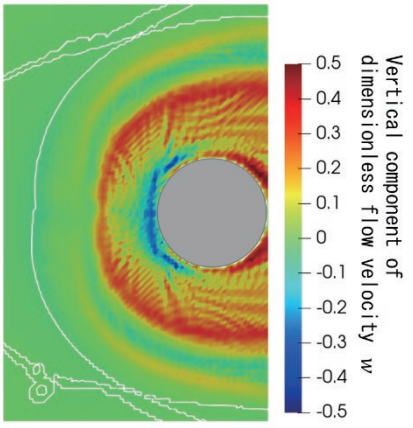

Fig. 7 Vertical component of dimensionless flow velocity at cell closest to riverbed (time-averaged value)

tions using a three-dimensional equation of motion. As the first step of the verification of the validity of our method, we conducted a reproduction analysis of a scouring experiment around a cylindrical pile [8].

The riverbed displacement in the analysis result was different from that in the experimental result in that the former did not exhibit a deposition area downstream of the scouring hole, but the scouring hole shape and scouring extent were in good agreement. Regarding the temporal change in scouring depth, the increasing tendency of the scouring depth was accurately reproduced. Regarding the movement of sediment particles at the cylindrical pile front surface as well, we qualitatively confirmed that the experimentally observed three-dimensional sediment movement was reproduced by our method. It was concluded from the above results that it was possible to evaluate local scouring with consideration of three-dimensional sediment movement using our method. As a result, it is expected that this could be applied to more complex conditions, such as when scouring countermeasures are present. Confirmation of the reproducibility of the flow field in the wake of the cylindrical pile and the refinement of the deposition model are thought to be tasks for future study.

This paper is a re-organization of Reference 17.

References

[1] Japan Transport Safety Board, Nankai Electric Railway Co., Ltd., Nankai Line, Train derailment accident (occurred on October 22, 2017), *Railway accident investigation report explanatory material*, http://www.mlit.go.jp/jtsb/railway/p-pdf/RA2019-1-2-p.pdf (Accessed: April 28, 2022) (in Japanese).

[2] Hino City, Summary report on response to Typhoon No. 19 in 2019 (final report), https://www.city.hino.lg.jp/_res/projects/default_project/_page_/001/015/018/syuseigaiyou.pdf (Accessed: April 28, 2022) (in Japanese).

[3] Roulund, A., Sumer, B. M., Fredsøe, J., and Michelsen, J., "Numerical and experimental investigation of flow and scour around a circular pile," *J. Fluid Mech*., Vol. 534, pp. 351-401, 2005.

[4] Baykal, C., Sumer, B. M., Fuhrman, D. R., Jacobsen, N. G. and Fredsøe, J., "Numerical investigation of flow and scour around a vertical circular cylinder," *Phil. Trans. Roy. Soc. A*, Vol. 373, Issue 2033, Article no. 20140104, 2015.

[5] Nagata, N., Hosoda, T., Nakato, T., and Muramoto, Y., "Three-dimensional numerical model for flow and bed deformation around river hydraulic structures," *J. Hydraul. Eng*., Vol. 131(12), pp. 1074-1087, 2005.

[6] Ota, K., Sato, T., and Nakagawa, H., "3D numerical model of sediment transport considering transition from bed-load motion to suspension—Application to a scour upstream of a cross-river structure—," *J. JSCE*, Vol. 4, pp. 173-180, 2016. pp. 23-32, 1996.

[7] Sekine, M., Ogawada, D., and Satake, Y., "Study on the transportation process of bed material load," *Journal of the Japan Society of Civil Engineers*, No. 545/II-36, pp. 23-32, 1996 (in Japanese).

[8] Umeda, S., Yamazaki, T., and Ishida, H., "Time evolution of scour and deposition around a cylindrical pier in steady flow," *Proc. of 4th Int. Conf. on Scour and Erosion*, pp. 140-146, 2008.

[9] Nakade, K., Ido, A., and Kajishima, T., "Meandering airflows beneath the underbody of a train model including bogie (LES of large-scale flow structure around real-shaped train model)," *Transactions of the Japan Society of Mechanical Engineers*, Vol. 87, No. 894, 2021 (in Japanese).

[10] Nakagawa, H., Tsujimoto, T., and Murakami, S., "Non-equilibrium bed load transport process on a side slope," *Proceedings of the Japanese Conference on Hydraulics*, pp. 561-566, 1985 (in Japanese).

[11] Marsooli, R. and Wu, W., "Three-dimensional numerical modeling of dam-break flows with sediment transport over movable beds," *J. Hydraul. Eng*., Vol. 141(1), 04014066, 2015.

[12] Sekine, M. and Kikkawa, H., "Rest mechanism of the transported particles as bed-load, *Journal of the Japan Society of Civil Engineers*," No. 399/II-10, pp. 105-112, 1988 (in Japanese).

[13] Sekine, M. and Kikkawa, H., "Mechanics of saltating grains," *J. Hydraulic Engineering, ASCE 118*, pp. 536-558, 1992.

[14] Einstein, H. A., "Formulas for the transportation of bed load," *Trans. ASCE*., No. 2140, pp. 561-597, 1942.

[15] Sekine, M., "Numerical simulation of braided river with the aid of slope-collapse model," Proceedings of Hydraulic Engineering, Vol. 47, pp. 637-642, 2003 (in Japanese).

[16] Iwagaki, Y., "Hydrodynamical study on critical shear stress,"

Transactions of the Japan Society of Civil Engineers, Vol. 41, pp. 1-21, 1956 (in Japanese).
[17] Ishii, H., Murotani, K., and Nakade, K., "Numerical model of local scour around pier based on the 3D analysis of sediment particle motion," *Journal of the Japan Society of Civil Engineers Ser. B1 (Hydraulic Engineering)*, Vol. 78, No. 2, pp. I_1021-I_1026, 2022 (in Japanese).

Authors

Hidenori ISHII
Researcher, Computational Mechanics Laboratory, Railway Dynamics Division
Research Areas: Computational Mechanics

Koji NAKADE, Ph.D.
Senior Chief Researcher, Head of Computational Mechanics Laboratory, Railway Dynamics Division
Research Areas: Fluid Mechanics, Computational Fluid Dynamics

Kohei MUROTANI, Ph.D.
Senior Researcher, Computational Mechanics Laboratory, Railway Dynamics Division
Research Areas: Computational Mechanics

Wooden Sleeper Deterioration Evaluation System Using Image Analysis of Video

Yosuke TSUBOKAWA **So KATO**
Track Geometry & Maintenance Laboratory, Track Technology Division

Nozomi NAGAMINE **Wataru GODA** **Riho MAEDA**
Image Analysis Laboratory, Information and Communication Technology Division

Kensuke ITOI
Track Geometry & Maintenance Laboratory, Track Technology Division (Former)

This paper describes the development of a low-cost, simple system for inspecting wooden sleepers using images taken with a forward-facing handheld camera placed at the front of a train. This system is expected to save labor for inspecting track facilities. The system uses deep learning to classify the deterioration of wooden sleepers from images. In this paper, we report the outline of the system: classification accuracy, and verification results to see if the progress of deterioration can be assessed.

***Key words*:** *wooden sleeper inspection, forward view images, image processing, deep learning*

1. Introduction

Track maintenance engineers manage wooden sleepers laid on tracks and determine their degree of deterioration by visual inspection or hammer test. In the case of successive wooden sleepers poorly fastened to the rails, the track gauge may expand due to lateral pressure when a train passes, potentially causing a derailment accident. The inspection of wooden sleepers is therefore an essential part of track inspections. Due to the large number of wooden sleepers, wooden sleeper inspection is more labor intensive than other types of inspection such as for track irregularity or turnouts. In addition, recent years have seen a growing shortage of track maintenance engineers, creating a need to develop inspection methods that are more efficient and do not depend on individual expertise. However, if the sleeper inspection is to be systematized, a simple and low-cost inspection method is required so that it can be introduced to local railways as well.

This paper therefore proposes an inspection method which employs inexpensive equipment and systems, and involves installing a handheld camera at the front of a train and automatically categorizing the degree of deterioration of wooden sleepers from the recorded images [1]. This method uses a commercially available handheld camera with an image resolution of 4K (8.29 million pixels) or higher. In addition, the proposed method uses deep learning to determine the degree of deterioration of wooden sleepers, allowing inspections to be carried out independent of the skills of track maintenance engineers.

In this paper, we give an overview of the wooden sleepers deterioration evaluation system and report the accuracy of the algorithm used in the system. We also discuss whether this system can monitor progression in wooden sleeper deterioration.

2. Wooden sleeper deterioration evaluation system

2.1 Overview of wooden sleeper deterioration evaluation system

The wooden sleeper deterioration evaluation system uses images taken from the front of a train to evaluate the degree of deterioration of wooden sleepers (Fig.1).

The flow chart in Fig. 2 illustrates how the algorithm in this system evaluates wooden sleeper deterioration. First, we perform a projective transformation on the image in front of the train (forward view images) to create a pseudo-underfloor image. Next, a mathematical model to evaluate wooden sleeper deterioration, which has been pre-trained using deep learning, is used to extract wooden sleepers from the pseudo-underfloor image and determine their degree of deterioration. The purpose of creating a pseudo-underfloor image is to prevent the non-uniform aspect ratio of wooden sleepers in forward view images from affecting the accuracy of extracting wooden sleepers and determining the degree of deterioration using deep learning. We also calculate the number of pixels the object moves between frames to determine the train's running speed and distance traveled, and link the kilometerage information to the extracted wooden sleepers. We then output the pseudo-underfloor image, noting the extracted location of the wooden sleepers and the category of the degree of deterioration. We also detect rail joints from the pseudo-underfloor image, and use clustering to accurately identify the number of rails present in the captured image and the number of sleepers attached to each rail. This produces a sleeper management form for each rail.

2.2 Capturing forward facing images from the driver's cab

We installed a handheld camera in the driver's cab at an overhead angle to capture forward facing images from the train (Fig. 3). Table 1 shows the main specifications of the handheld camera used. If the camera has a resolution of 4K or higher, images can be processed and used to detect deterioration through this system. In addition, we confirmed that no sleepers were missed when recording happened at standard frame rate of 30fps when the train was operating at conventional-line running speed.

2.3 Creating a pseudo-underfloor image using projective transformation

In forward view images, objects become thinner from the front

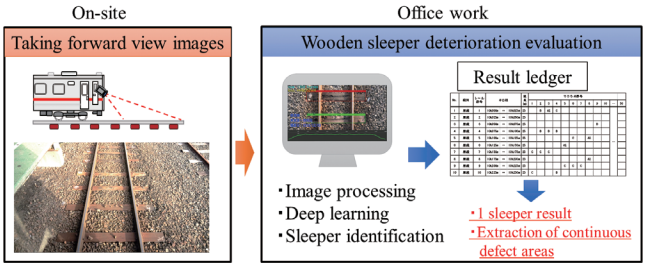

Fig. 1 Wooden sleeper deterioration evaluation system

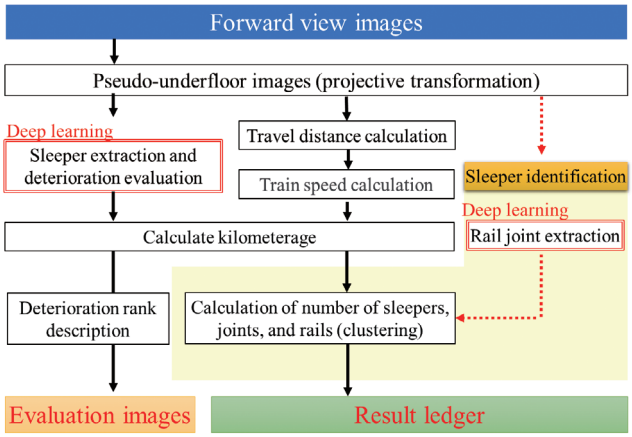

Fig. 2 Flow chart of algorithm to evaluate wooden sleeper deterioration

Fig. 3 Camera installation status

Table. 1 Main specifications of handheld cameras

Camera	Focus length	Effective number of pixels
FDR-AX50	7.5 m	8.29 million pixels

to the back of the image and appear trapezoidal. Therefore, we use projective transformation to convert the forward view image into an image which appears to have been taken from directly above. Figure 4 shows an example of the result of the projective transformation. The projective transformation process calculates the four coordinate points of a trapezoidal area (abcd) in the forward view image to the four coordinate points of a rectangle (abc'd') corresponding to the aspect ratio of the actual sleeper. The size of the image after conversion is 1,920 × 800 pixels, and it is an image that reflects an area approximately the size of two sleepers.

2.4 Kilometerage estimation [2]

Railway facilities are maintained and managed on the basis of kilometer points corresponding to the position of installations. For

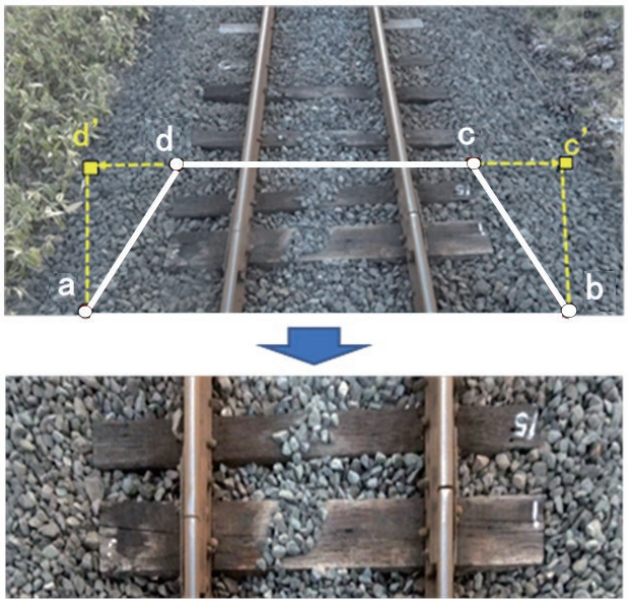

Fig. 4 Pseudo-underfloor image by a projective transformation

example, data measured by track inspection cars are corrected by detecting fixed points at assigned kilometer distances along railway tracks. In image analysis, a similar approach can be used to detect fixed points and assign kilometer distances to each frame. In this study, however, the aim is to achieve this using only handheld cameras. Therefore, we estimate the kilometer point directly from the forward view images.

The kilometerage data are generated using the speed of train movement calculated by image analysis from between the two images. Optical flow is used to calculate the velocity vectors for all pixels in the images. The moving speed [pixel / frame] of the train in each frame takes the most frequent value of the speed vectors from which outliers have been removed.

The pixel movement speed in each frame is accumulated to create the distance data for each pixel. When the distance at the start of the video is 0, the distance the pixel moves at frame t is found by integrating the speed from 0 to t. Since the integration results include errors, the kilometerage and travel distance at the time of the start of shooting are used to adjust the distance in pixels to the image frame and create kilometerage data for the image frame.

2.5 Wooden sleeper deterioration evaluation using deep learning

We extract wooden sleepers and determine the degree of deterioration using a deterioration degree determination model that is pre-trained using deep learning on the pseudo-underfloor image.

2.5.1 Development of training data

To develop the deterioration evaluation model, we use VoTT (Visual Object Tagging Tool) provided by Microsoft to create training data by tagging areas based on the shape and degree of deterioration of the wooden sleepers. Figure 5 shows the standard for evaluating the degree of deterioration of wooden sleepers. Defective sleepers are classified A1 to B, minor damage is classified C, and good sleepers are classified D. In addition, if the surface of the

sleeper is hidden or buried by a lot of ballast or grass, and the degree of deterioration cannot be determined properly from the image, it is marked as undetermined (no classification is made). Besides, PC sleepers are determined as independent categories, thus classification of sleepers is 7 categories. Categories A1 to B indicate that the sleepers are in poor condition. Based on normal management, A1 category sleepers should be replaced as soon as possible. If there are 3 successive category A2 sleepers, these should be replaced as soon as possible. Category B sleepers should be monitored over time. Figure 6 shows an example of training data created using VoTT.

2.5.2 Data augmentation [3]

Deep learning enables high accuracy classification through training from a large amount of image data. However, many of the pseudo-underfloor images obtained so far are of well-maintained sleepers, and there was a shortage of training data for degraded sleepers. Acquiring training data for degraded sleepers involves capturing photographs on various sections and is labor-intensive. The lack of training data can be considered one of the factors to a decrease in accuracy of degraded sleeper assessment. Therefore, we needed to efficiently obtain training data for defective sleepers.

Consequently, we performed two types of image processing on the images that serve as training data (referred to as "original images") to augment the training data. The first method was image color tone processing. As shown in Fig. 7, four images with different levels of "brightness" and "contrast" were created from the original images. When processing the color tones, variations of ±60% were applied to the brightness and light-dark ratios to account for environmental changes that may occur during actual capturing, such as the influence of weather and the movement of the sun. The second was noise addition. As shown in Fig. 8, we used two noise processing techniques. One was to assume the white noise that occurs during shooting, and to determine the RGB values and positions using random numbers we generated 1,000 dots for each original image. The other method was to take into account the blurring of images that can occur due to train vibrations or low brightness when shooting and used smoothing processing using an averaging filter to blur the images.

2.5.3 Development of deterioration evaluation model

We performed a total of 6 types of image processing, and thus managed to increase existing data for A1 category sleepers approximately 4 fold, approximately 5 fold for category A2 and B sleepers and one and half times for category C sleepers. Table 2 shows the number of sleepers tagged in existing original images (approximately 100,000 images) and the number of sleepers tagged in the expanded number of images (approximately 100,000 images). As a result, we used approximately 200,000 images and attached 370,000 tags to construct the deterioration evaluation model.

A deterioration evaluation model was created using a deep learning technique on the training data. For deep learning, we used YOLOX as the network architecture. YOLOX is a method that simultaneously performs object detection and identification in deep learning. When applied to input images, YOLOX's identifier provides outputs including object category, category class confidence (probability), horizontal position, vertical position, width, and height.

2.6 Identification of sleepers

The same sleepers and rail joints are visible in several frames in the pseudo-underfloor image converted from forward view images,

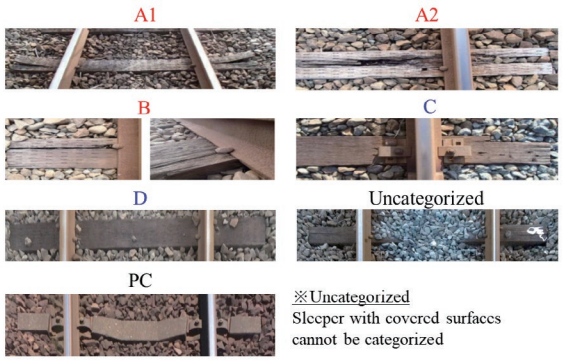

Fig. 5 Wooden sleeper deterioration evaluation standard

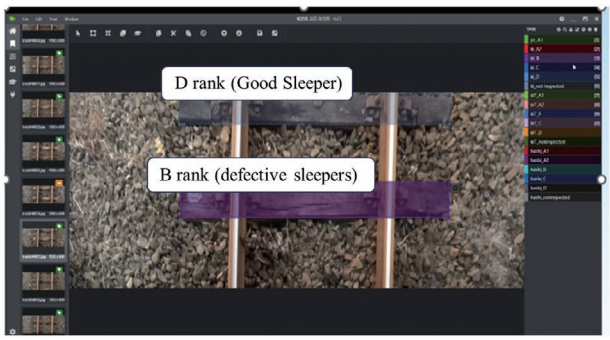

Fig. 6 Training data created using VoTT

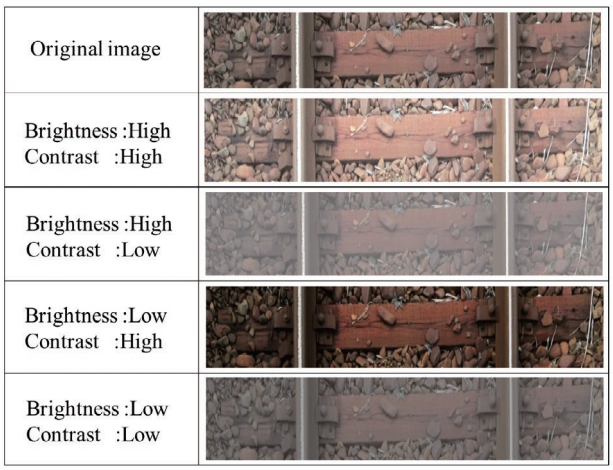

Fig. 7 Data augmentation (color processing)

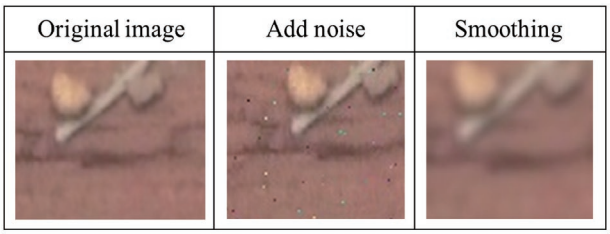

Fig. 8 Data augmentation (noise processing)

so it is necessary to identify them as being the same. When assigning kilometers to several frames, those that are close together can be considered to be the same sleeper or rail joint. We therefore used the shortest distance method, which is a type of cluster analysis method, to group the sleepers. The number of groups obtained corresponds to the number of sleepers and rail joints on the track. The threshold for the shortest distance between sleepers and rail joints to be either be grouped as the same sleeper/joint or considered separate was set at 20 cm from the width of the sleeper for sleepers and 1 m to 2 m for rail joints. To categorize the level of sleeper deterioration, the sleeper with the most advanced level of deterioration within the cluster was adopted for identification, ensuring a conservative approach for safety assessment.

3. Accuracy verification of deterioration evaluation

3.1 Evaluation method of classification accuracy

We evaluated the accuracy of this algorithm using two methods. In the first method, the evaluation was performed by comparing the classification results of track maintenance engineers who visually checked the pseudo-underfloor image (image classification results) with the classification results of the algorithm (system classification results). In the second method, the evaluation was performed by comparing the system classification results with the results determined visually and acoustically by track maintenance engineers on-site (on-site inspection results).

3.2 Evaluating classification accuracy (comparison with image classification results)

For the 16,033 sleepers detected using this algorithm, the image classification results were used as the correct values and compared with the system classification results. Figure 9 shows an example of the system classification results, and Table 3 shows the agreement rate of the classification for each degree of deterioration of the wooden sleepers. The agreement rate for the degree of deterioration of the wooden sleepers was 88.6% for category C, and over 90% for category D and B to category A. In addition, the rate was 72.1% for unclassified cases and 98.5% for PC sleepers. Furthermore, regarding sleeper detection accuracy, the system detected 16,033 sleepers out of a total of 16,111 (detection rate 99.5%), indicating that sleepers could be detected with a high probability. Figure 10 shows the ratio of system classification results to image classification results. The ratio of defective sleepers (categories A2 and B) to non-defective sleepers (categories C and D) was approximately 7%.

Fig. 9 Detection of wooden sleepers and deterioration evaluation results

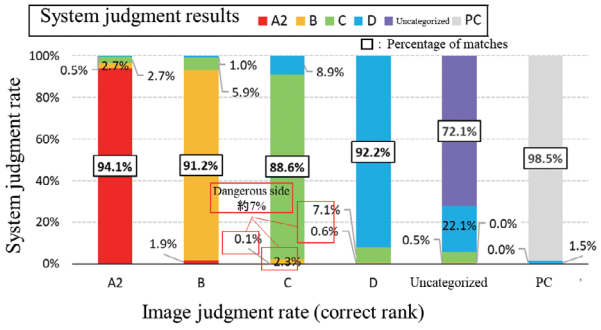

Fig. 10 Proportion of system classification results to image classification results

3.3 Evaluation method of classification accuracy (comparison with on-site inspection results) [4]

For the 695 sleepers detected using this algorithm, the on-site inspection results were used as the correct values and compared with the system classification results. This means that consistency with the current sleeper inspection was verified. Table 4 shows the rate of system classifications which matched the correct classifications for "A2 and B" as "defective sleepers" and "C and D" as "non-defective sleepers."

The match rate was 53% for category A2, 86% for category B, 0% for category C, and 78% for category D. In the images used for

Table. 2 Number of tagged sleepers

Rank	Number of tags for original image	Number of tags for expanded images	Total number of tags
A1	12	49	61
A2	3,754	17,575	21,329
B	12,719	55,801	68,520
C	33,364	45,415	78,779
D	103,552	60,484	164,036
Uncategorized	2,138	10,674	12,812
PC	23,450	—	23,450
Number of Training images	Original image	Expand image	Total image
Total images	178,989	189,998	368,987

Table. 3 Accuracy of wooden sleeper deterioration classification

	A2	B	C	D	Uncategoraized	PC
Image judgement	404	1,292	3,387	10,476	208	266
System judgement	380	1,178	3,001	9,662	150	262
Match rate	94.1%	91.2%	88.6%	92.2%	72.1%	98.5%

Table. 4 Accuracy of classification by level of deterioration

Rank	A2	B	C	D
On-site inspection	119	133	26	417
System judgement	63	115	0	325
Match rate	53%	86%	0%	78%
On-site inspection	252		443	
System judgement	249		328	
Correct answer rate	99%		74%	

verification, there was a lot of visible damage on the sleeper surfaces, so a high percentage of category C sleepers were classified as category A2 or category B.

Compared with the match rate in the image classification results in Table 3, the match rate with the on-site inspection results was low for all categories. The reason for this is thought to be because damage that is difficult to classify on images can be detected during on-site inspections by performing a hammer test.

The correct answer rate for defective sleepers was 99%, and the correct answer rate for non-defective sleepers was 74%. It is therefore considered that there is sufficient accuracy in determining whether the sleeper is defective or not. Figure 11 shows the ratio of the system classification results to the on-site inspection results. The percentage of the on-site inspection results that the system classified as dangerous was 47% for category A2, 2% for category B, and 8% for category C. Since the percentage of category A2 sleepers being classified as non-defective sleepers was 1%, the probability of misjudging defective sleepers (categories A2 and B) as non-defective sleepers (categories C and D) is low.

3.4 Analysis of variation in evaluation results [5]

We used the images of 218 sleepers to confirm the dispersion between the image classification results and the system classification results. Figure 12 shows the image classification results and the system classification results for each deterioration category. We can confirm that there is variation in both classification results. Regarding category C, the image classification results show less variation than the system classification results. The reason for this is that while the system classifies images based on limited training data, image classification allows more detailed images to be checked for damage that is difficult to categorize.

Next, we analyzed variation in correct answer rates between the two classification results. For example, for a category B sleeper, if it was classified as category B in both image categorization and system classification, the score will be 0, if it is classified as category A2, it will be +1, if it is classified to be a category C, it will be −1, and if it is classified as category D, the score is −2. The histogram in Fig. 13 shows the scores for all sleepers. The shape of both histograms is similar, indicating that the system results follow the same tendency as the results from image categorization.

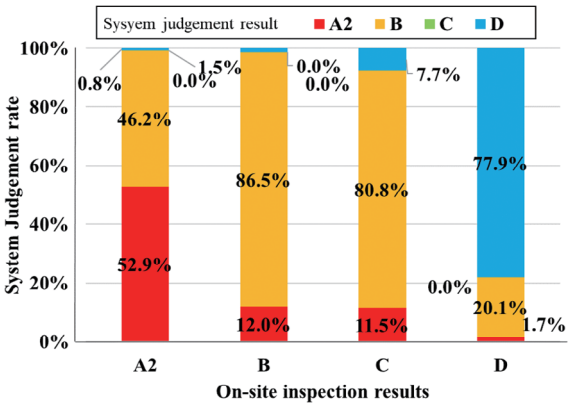

Fig. 11 Proportion of system classification results to on-site inspection results

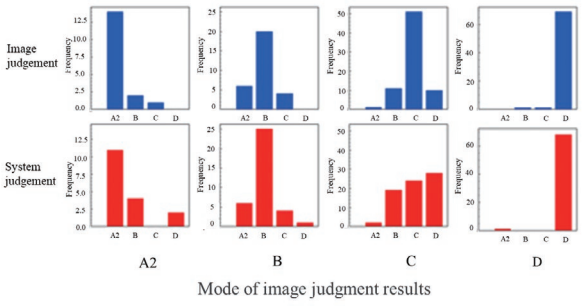

Fig. 12 Distribution of image classification results and system classification results

4. Examination evaluation of progress in deterioration

We compared the results of the 2021 and 2022 field inspections to confirm whether or not the deterioration level of the 128 wooden sleepers had also progressed based on the system classification results.

Figure 14 shows the progression in the degree of deterioration from on-site inspection results and system classification results, while Table 5 shows the percentage of agreement between on-site inspection results and system classification results. Table 5 also shows the year-on-year percentage changes in deterioration based on the system classification results.

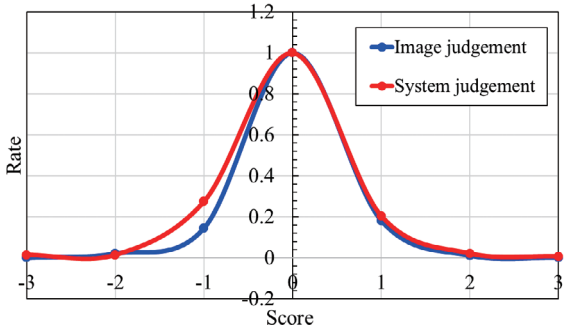

Fig. 13 Distribution of classification result scores

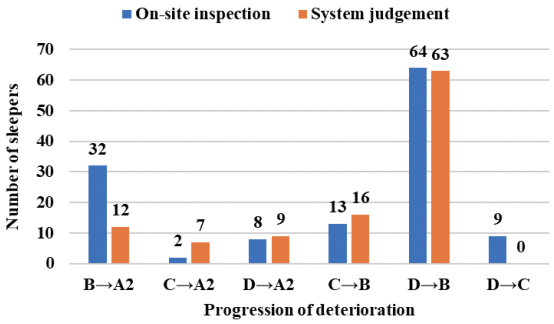

Fig. 14 Number of deterioration progression

Table. 5 Match rate by type of deterioration progression

Progression of deterioration	B→A2	C→A2	D→A2	C→B	D→B	D→C
On-site inspecton	32	2	8	13	64	9
System judgement	10	1	3	9	56	0
Match rate	31%	50%	38%	69%	88%	0%
On-site inspecton	128					
System judgement	107					
percentage progressed	83%					

There was approximately 70-90% agreement on the progress ion from C or category D to defective sleeper category B, and approximately 30-50% agreement on the progression from each category to category A2. In addition, the percentage of sleepers which had moved up a category in level of deterioration was 83%. This system therefore has the potential to recognize progression of deterioration in sleepers with an accuracy of approximately 80%.

5. Summary and future work

This paper describes the development of a low-cost system that evaluates the degree of deterioration of wooden sleepers from images taken with a handheld camera from the front of a train. We verified the classification accuracy of this system and found the following:

- Comparing the image classification results visually classified by track maintenance engineers with the system classification results of this algorithm, it was confirmed that the classification accuracy of this system was over 90%.
- Comparing the on-site inspection results by track maintenance engineers with the system classification results, it was confirmed that this system can classify defective sleepers (categories A2 and B) with 99% accuracy.
- Analyzing the dispersion between image classification results and system classification results, it was confirmed that the system classification results had the same variation as the image classification results.
- As a result of verifying the ability of this system to detect the progression of deterioration of wooden sleepers, we were able to identify approximately 80% of the sleepers whose deterioration had progressed based on data from on-site inspection.

This system makes it possible to detect defective sleepers with a high degree of accuracy and also efficiently track progression the degree of deterioration of wooden sleepers. In future, we will study how to apply this system to the inspection of wooden sleepers and aim to put it into practical use.

References

[1] Itoi, K., Tsubokawa, Y., Nagamine, N., Goda, W., Ohba, H., Kato, S., "Development of an algorithm for determining the degree of deterioration of wooden sleepers using images in front of trains," *76th Annual Conference of the Japan Society of Civil Engineers*, 2021 (in Japanese).

[2] Goda, W., Nagamine, N., Mukojima, H., Itoi, K., Tsubokawa, Y., Kato, S., "Kilometer distance estimation by optical flow using images in front of the train," *TER = The Papers of the Technical Meeting on* "*Transportation and Electric Railway*," IEE Japan 2021, 2021 (in Japanese).

[3] Itoi, K., Nagamine, N., Goda, W., Tsubokawa, Y., Kato, S., "Improving the accuracy of wooden sleeper inspection methods using images in front of trains," *J-RAIL2021*, 2021 (in Japanese).

[4] Kato, S., Tsubokawa, Y., Nagamine, N., Goda, W., Maeda, R., Yamazaki, M., Itoi, K., "Evaluation of the degree of deterioration over time using a wooden sleeper deterioration evaluation system," *J- RAIL2022*, 2022 (in Japanese).

[5] Maeda, R., Nagamine, N., Goda, W., Tsubokawa, Y., Kato, S., "Development of an AI system for determining the degree of deterioration of wooden sleepers using images in front of trains," *J-RAIL2022*, 2022 (in Japanese).

Authors

Yosuke TSUBOKAWA
Senior Chief Researcher, Head of Track Geometry and Maintenance Laboratory, Track Technology Division
Research Areas: Track Measuring, Track Maintenance

So KATO
Researcher, Track Geometry and Maintenance Laboratory, Track Technology Division
Research Areas: Track Measuring

Nozomi NAGAMINE, Ph.D
Senior Chief Researcher, Head of Image Analysis Laboratory, Information and Communication Technology Division
Research Areas: Computer Vision, Image Processing, Signaling Systems

Wataru GODA
Researcher, Image Analysis Laboratory, Information and Communication Technology Division
Research Areas: Computer Vision, Image Processing

Riho MAEDA
Researcher, Image Analysis Laboratory, Information and Communication Technology Division
Research Areas: Computer Vision, Image Processing

Kensuke ITOI
Researcher, Track Geometry and Maintenance Laboratory, Track Technology Division (Former)
Research Areas: Track Measuring

Development and Performance Evaluation of Rail Fastening System Using Non-metallic Materials for Main Members

Atsushi MATSUO **Tadashi DESHIMARU**
Track Structures & Components Laboratory, Track Technology Division

Yoshihiro MASUDA **Minoru SUZUKI**
Vibration-Isolating Materials Laboratory, Materials Technology Division

Rail fastening systems are generally designed to provide a certain level of electrical insulation to prevent rail current from leaking through the supporting track components to the earth. Despite this, some cases have been reported where, in some installation environments, the electrical insulation of rail fastening systems has deteriorated, resulting in transport disruptions caused by incidents such as ground faults and short circuits. Thus, we studied the applicability of resin materials to rail fastening members to prevent the reduction of the electrical insulation. Based on the results of this study, we produced a prototype of a rail fastening system using resin members and evaluated its performance. The performance evaluation of the prototype confirms that the prototype has the sufficient performance to be installed on a conventional rail track.

***Key words*:** *rail fastening system, CFRP, FRTP, GFRP, electrical insulation*

1. Introduction

Rail fastening systems are among the track components fastening rails onto rail supporting components, such as rail sleepers and slabs. They are required to provide electrical insulation between rails and supporting components to prevent signal currents and return rail currents from leaking to rail supporting components.

Surface contamination due to dust deposits, especially in wet conditions, can be cause of insulation performance deterioration of rail fastening systems. The insulation deterioration sometimes leads earth faults, which may sometimes result in a track fire or smoke accident on steel bridges and so on.

To address these issues, fastening systems are required to have sufficient electrical insulation performance even in wet and dusty environments.

In general, principal members of rail fastening systems, such as rail clips, baseplates and lateral support blocks, subject to railway vehicle loads through the rail, are made from metallic material because they are better in terms of durability, ease of production and cost.

For reasons of cost, the use of non-metallic materials, however, is limited to use on members which require electrical insulation. Thus, applying non-metallic material to main components of rail fastening systems is expected to improve electrical insulation performance.

However, there are few cases where non-metallic materials are used as the main members of rail fastening systems. As a result, there is so far almost no knowledge on structural optimization considering load application and the evaluation process of external factors. In this study, the authors conducted a feasibility study on using non-metallic materials for the main members of rail fastening systems to drastically reduce the risk of transport disruption caused by the electrical insulation performance deterioration of fastening systems.

Based on the feasibility study results, the authors also conducted a trial production of rail fastening systems made with non-metallic members. Electrical insulation performance tests and fatigue life resistance tests were performed using the prototype rail fastening device.

2. Members of the rail fastening system

2.1 Selection of rail fastening system type

The "Direct eight fastening system," D8, was selected as a rail fastening system using non-metallic members, since it is generally applied for slab tracks in Japan. Figure 1 shows the composition of this rail fastening (D8).

The D8 is a structure that bears the railway vehicle loads by means of steel rail clips and baseplates, and ensures electrical insulation between the rail and the bearing by a non-metallic insulating plate.

This study aims to replace steel rail clips and baseplates with non-metallic members, among the members shown in Fig. 1.

2.2 Performance requirement of the members

While the use of non-metallic materials for components can be expected to improve electrical insulation, the strength of the members may decrease. Therefore, the target performance was set for non-metallic rail clips and baseplates respectively, as shown in Table 1.

The reasons for setting the performance targets set for each are as follows:

(1) Rail clip

The rail clips applied non-metallic material should have the strength equivalent to steel enough to resist the rail tilting and without excessive uplift stiffness.

When the uplift stiffness increases, the spring's ability to follow the vertical displacement of the rail tends to decrease. This is why the performance target was set to realize spring characteristics equivalent to those of conventional metal materials.

(2) Baseplate

Baseplates are a large component in rail fastening systems. The use of non-metallic materials therefore makes it possible to integrate the insulation function of baseplate shims, reducing the number of members in the fastening system.

However, use of non-metallic materials for the baseplate may

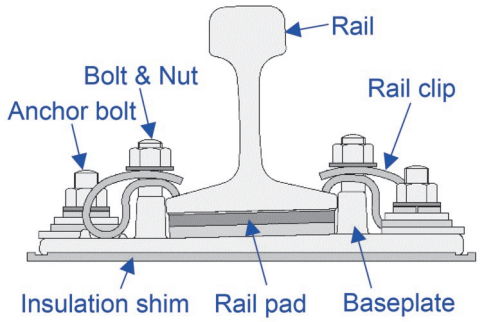

Fig. 1 Type direct 8 (D8) fastening system

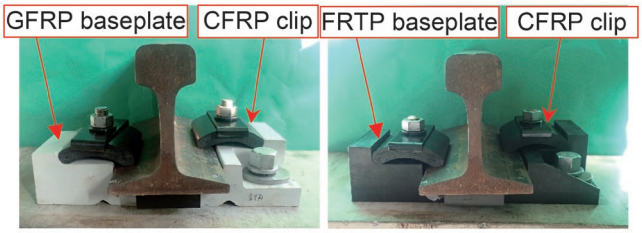

Fig. 2 Prototype of proposed structure

lead to a reduction in loading capacity against lateral loads.

Considering these issues, the target performance was set to ensure that materials used and their shape achieved sufficient strength for lateral load.

2.3 Selection of non-metallic materials applied

The non-metallic materials used for the rail clip and baseplate were selected considering the target performance shown in Table 1.

Fiber-reinforced plastic, FRP, was selected since it has the same strength as metal material.

Considering the feasibility of the target performance, we selected three kinds of material shown below among FRPs.

- Carbon fiber reinforced plastics, CFRPs;
- Glass fiber reinforced plastic, GFRPs;
- Chopped carbon fiber reinforced thermoplastic, FRTPs.

Although the electrical insulation property of CFRPs is relatively inferior to the other FRPs, it is superior to metal materials. Considering the feasibility of uplift stiffness, we finally selected CFRPs as the materials for the rail clip and examined them.

For the baseplates, GFRPs and FRTPs were both selected from the viewpoint of mechanical strength.

3. Applicability examination of non-metallic materials

3.1 Proposal and manufacture of rail fastening assembly using non-metallic materials

To examine suitability, we proposed a rail fastening assembly using materials selected in Chapter 2.3 and manufactured a prototype. The proposed design of each member is shown in Fig. 2.

The rail clip made with CFRP was designed to fit a bolt-on fastening assembly. The cross-section of the clip is a flat plate with a curved edge, so that the rail fastening position of the clip can be changed in response to the change in the vertical position of the rail.

Table 1 Target components and applied materials

Target components	Target performance	Material
Rail clip	Spring constant equivalent to steel	CFRP
Baseplate	Loading capacity equivalent to existing rail fastening	GFRP
		FRTP

Table 2 Material composition of proposed components

Component	CFRP spring clip	GFRP baseplate	FRTP baseplate
Resin	Epoxy resin	Vinyl ester resin	Polyamide
Fiber	Carbon (prepreg)	Glass (fabric)	Carbon (chopped)
Manufacturing method	Press molding	Hand lay-up	Injection molding

The baseplate made of GFRPs and FRTPs is designed considering the compatibility with the existing D8 described in section 2.1, such as the position of bolt holes for fastening the baseplate to a rail supporter. The volume of the baseplates is increased compared with that of D8 made of steel to increase electrical insulation and strength against horizontal loads. The functional integration of members of the fastening assembly by improving the electrical insulation of the baseplate means that it is possible to reduce the number of members.

Table 2 shows the configuration of the proposed fastening assembly. Figure 3 shows the members of the prototype fastening assembly. The molding method was as follows:

(1) CFRP fastening spring (Fig. 3(a), Fig. 3 (b))

Pre-preg which is made from carbon fiber textiles and an epoxy resin is laminated to form a reinforcing structure with carbon fibers oriented in the longitudinal direction of the rail, perpendicular to the rail, and in the ±45° direction thereof.

(2) GFRP baseplate (Fig. 3 (c), Fig. 3 (d))

Epoxy resin-impregnated glass fiber fabrics are laminated and compression molded. To provide loading capacity, the shoulder section has a structure in which the reinforcing fibers in the cross-section are bent upward by 90°.

(3) FRTP baseplate (Fig. 3(e) and Fig. 3 (f))

This is made by injection molding, in which heated molten resin is injected into a mold. The bottom is lattice-shaped to reduce the effects of strain caused by the slow cooling process, compared with the case of a solid structure.

3.2 Prototype strength test of designed members

Following the material strength test, performance tests are conducted to explore the feasibility.

(1) CFRP rail clip

The test is conducted to obtain the uplift stiffness of prototype rail clips.

Figure 4(a) shows the test setup. Following the rail fastening process using rail clips, when the rail is lifted using an actuator in a vertical direction, the uplift stiffness is obtained from the relationship between vertical load and rail height.

Figure 4(b) shows the test results. The uplift stiffness of prototype rail clips is 7.7 MN/m between 4 kN and 12 kN in load, where

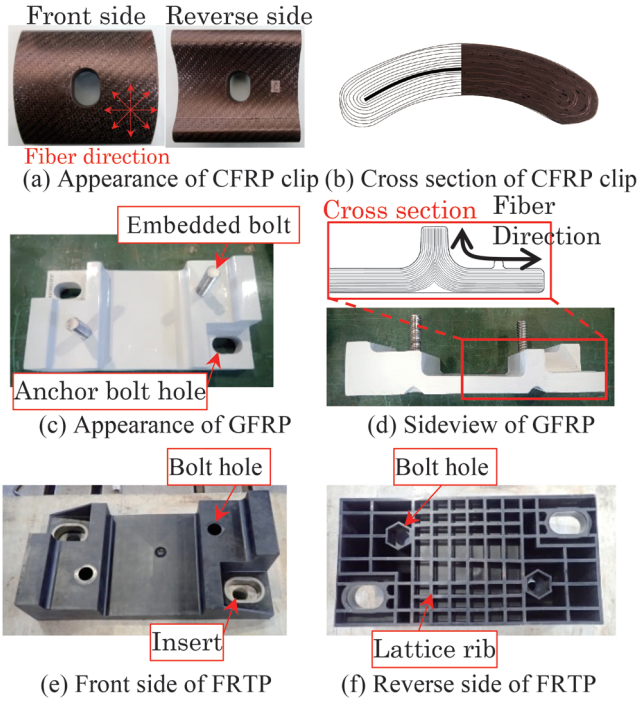

Fig. 3 Components appearance

the axial force of the fastening bolts is around 5 kN. This value is about thirteen times that obtained using the D8.

It can be considered that this is the effect of the thickness of the rail clip. It is clear that the thickness of the clip should be reduced to increase its deformation in order to have the uplift stiffness near to that of the D8.

(2) GFRP and FRTP baseplates

Tests were conducted to obtain the loading capacity of the GFRP and FRTP baseplates against the lateral force applied. The applicable curve radius of rail for the baseplates, which is defined in the Japanese design standard for railway structure[1], was selected on the basis of this test result.

As shown in Fig. 5, the lateral force acts on the bottom of the rail on the assembled rail fastening systems. The relationship between load and displacement of the rail or baseplate is obtained. The loading continues until the destruction of the baseplate is observed.

Figure 6 shows the test results, where the arrows indicate the points where baseplate slides occur. All the tested baseplate slides occur when the lateral load is less than 60 kN, equivalent to the lateral force where the axial load is 150 kN and curve radius is less than 600 m. Therefore, considering this result, the applicable condition of this prototype baseplate is set as a curve radius of 600 m or more with a design axial load of 150 kN.

4. Proposed calculation method for resin member design reference values

The fatigue resistance of rail fastening members is evaluated by comparing the generated stress with the design reference values.

For steel members, endurance limit diagrams have been used as design reference values for each steel material, because the fatigue resistance evaluation methods have been already established.

For resin members, although their mechanical strength is affected by environmental conditions of where they are installed, such

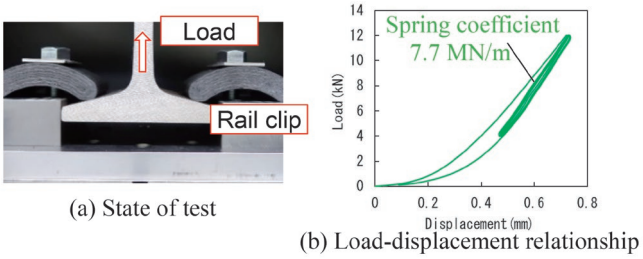

Fig. 4 Measurement of spring coefficient of CFRP clip

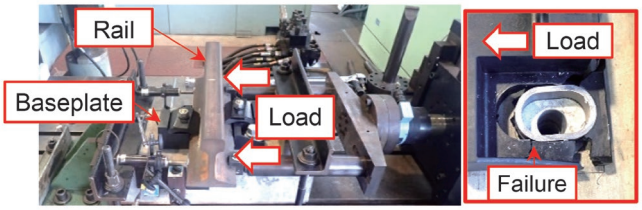

Fig.5 Test of lateral spring coefficient (FRTP)

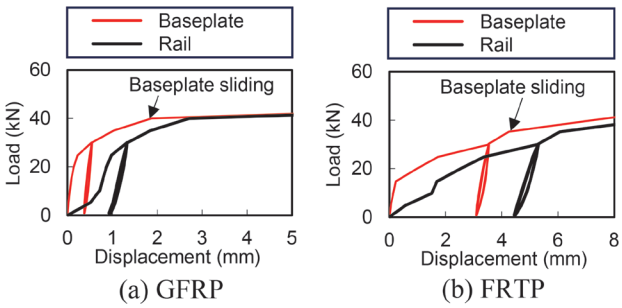

Fig. 6 Relationship between load and lateral displacement

as temperature and ultraviolet rays, so far, design reference values reflecting these conditions have not been defined. Therefore, the authors proposed a provisional method for calculating design reference values for stresses in resin members. The proposed formula is shown in (1).

$$|D_{si}| = (P_s - 3\sigma)\times(1-C_T)\times(1-C_{WA})\times(1-C_F)\times(1-C_W) \quad (1)$$

There,

D_{si}: design basis value

P_s: standard temperature property value

σ: standard deviation of the mechanical strength at standard temperature

C_T: temperature reduction factor

C_{WA}: water absorption reduction factor

C_F: fatigue degradation factor

C_W: weathering degradation factor.

The method to determine the various factors are shown below.

(1) Temperature reduction factor C_T

The temperature reduction factor is the reduction ratio in the minimum mechanical strength between -20 and 60°C relative to the mechanical strength at the standard temperature of 23°C. C_T of CFRPs is not considered because the tensile strength of CFRPs generally have no temperature dependence.

(2) Water absorption factor C_{WA}

The mechanical strength of FRTP decreases due to moisture absorption. Therefore, the water absorption factor is defined as the reduction ratio of the strength on water absorption from the strength

Table 3 Calculation results

Item			CFRP		GFRP		FRTP	
			Tensile	Bending	Tensile	Compressive	Tensile	Compressive
Standard temperature strength (MPa)	P_S	Measured value	638.4	462.0	191.8	317.9	204.1	252.1
Deviation (MPa)	σ		18.0	9.4	24.3	10.1	2.0	3.1
Design reference value (MPa) (provisional)	D_{si}	—	374.0	263.7	85.6	200.8	93.4	119.4

Table 4 Design conditions

Rail type	JIS-60 kg rail
Axle load	150 kN
Alignment	600 m≦R
Fastening interval	625 mm

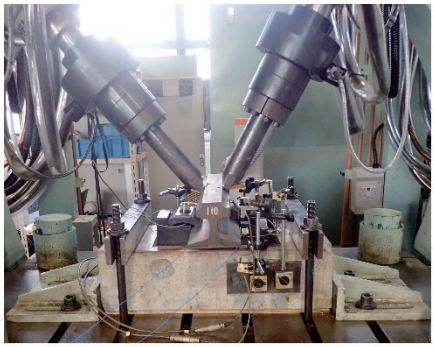

Fig. 7 Two-directional loading test

Table 5 Two-directional loading conditions

Item	Unit	GFRP	FRTP
Load A L_A	kN	48.5	49.6
Load B L_B	kN	34.1	34.2
Angle θ_A	deg	49.1	51.1
Angle θ_B	deg	58.2	60.3
Height of the loading position h	mm	100	110
Minimum load L_0	kN	10	10

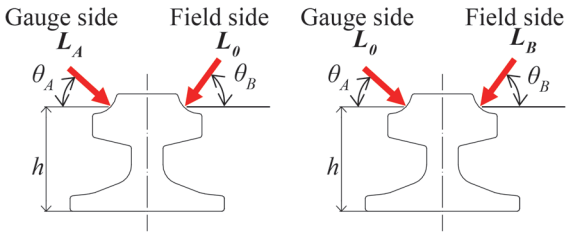

Fig. 8 Two-directional loading conditions

on drying.

(3) Fatigue degradation factor C_F

In this case, the fatigue degradation factor is provisionally set at 0.1, assuming use in conditions where fatigue failure does not occur.

(4) Weathering degradation factor C_W

It was assumed that no significant reduction in member strength would occur because the effect of UV rays would be limited to within a few hundred micrometers on the surface layer. Therefore, the value was provisionally set at 0.1.

Based on the above, measured and provisionally assumed values were set as the reduction factor and design basis values were calculated. Table 3 shows the results of the calculation.

In order to improve the accuracy of the reference values, material characterization tests should be conducted for C_F and C_W, which were set as provisional values.

This formula focuses only on mechanical strength. In addition to the above-mentioned properties, tests on creep and abrasion resistance properties should be conducted when assessing the applicability of resin materials.

5. Performance tests of prototype members

5.1 Static and dynamic two-directional loading tests

Static and dynamic two-directional loading tests were conducted to evaluate the fatigue resistance of the rail fastening assembly consisting of the prototype members, such as the rail clip and baseplates. Figure 7 shows the setup of the loading tests. In the test, the reproduced load which railway vehicle generates is applied to the gauge side and the field side of rail tracks, respectively.

The static two-directional loading test was conducted to evaluate the generated stress of the rail clip against the design load. Table 4 shows the design conditions. The distributed force which acts on a set of the rail fastening assembly are calculated using the proposed finite element method (FEM) model [2] for the derivation of rail tilt considering the design conditions and several stiffnesses of rail fastening assembly obtained in the tests conducted in advance. Table 5 and Fig. 8 show the loading test loading conditions based on the distributed force.

Figure 9 and Fig. 10 show the measuring point of the stress and the relationship between load and stress respectively. The dotted line in Fig. 10 is the design value of mechanical strength calculated using the proposed formulas indicated in Chapter 4. It was confirmed that the maximum tensile and compressive stress of the rail clips and baseplate are within the proposed design value. It is noted that the generated stress of the rail clip is small enough in relation to the physical properties of CFRPs. Hence, it is possible to reduce the thickness of the rail clip.

Dynamic two-directional loading tests were conducted to eval-

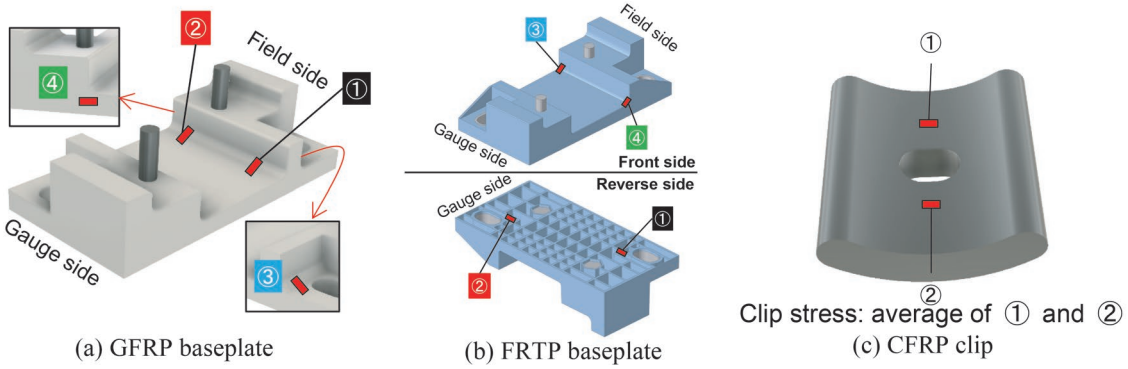

(a) GFRP baseplate (b) FRTP baseplate (c) CFRP clip

Fig. 9 Measuring point of stress

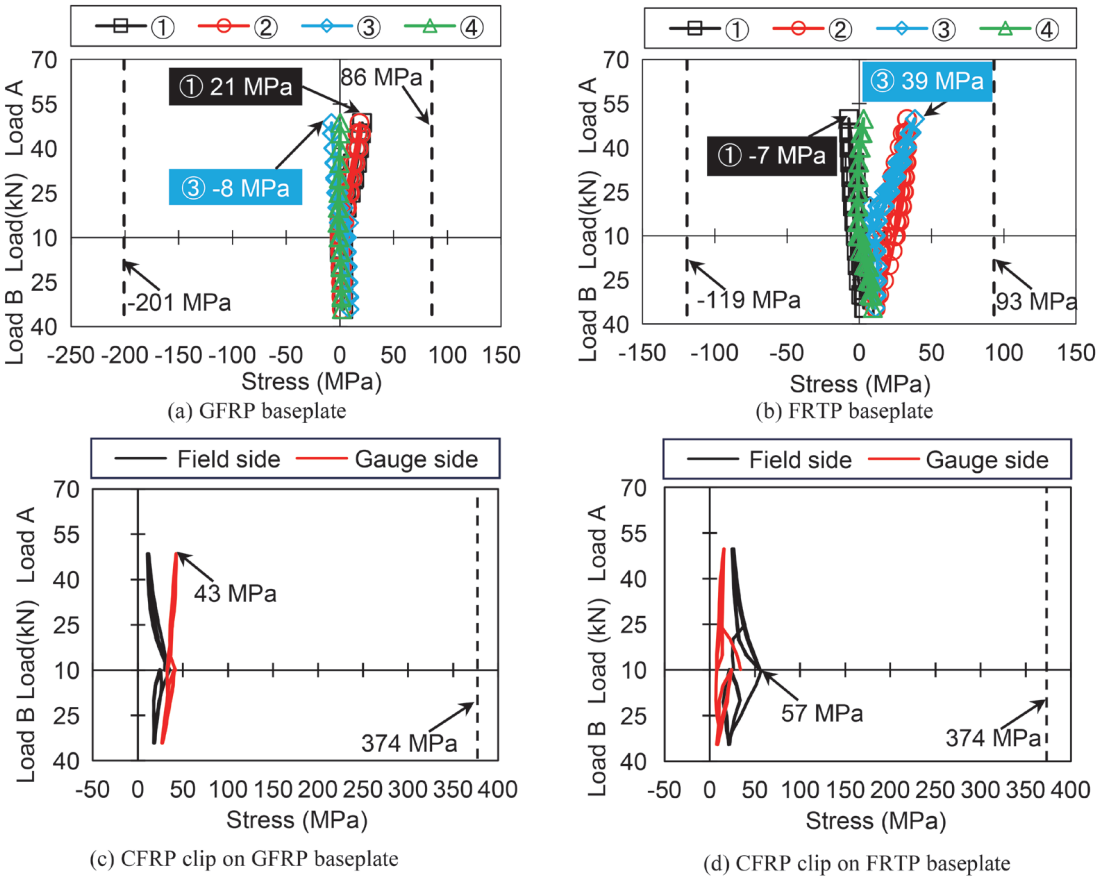

(a) GFRP baseplate (b) FRTP baseplate

(c) CFRP clip on GFRP baseplate (d) CFRP clip on FRTP baseplate

Fig. 10 Relationship between load and generated stress

uate the fatigue resistance of the rail fastening assembly. One million cyclic loadings were carried out by applying alternate loads from the gauge side and field side under the same conditions as the static loading test. After completion of cyclic loading, a visual check was conducted, and no damage was observed.

As a result, it was confirmed that the prototype fastening members had fatigue resistance that could be installed under the track conditions shown in Table 4.

5.2 Electrical insulation resistance test

The electrical insulation resistance test was conducted to compare the electrical insulation properties of the prototype fastening members with the existing rail fastening system.

Figure 11 shows the test setup. In the test, the concrete block on which the fastening assembly is fastened is placed on a grounded electrode. The alternating voltage of 10 V is applied between the rail and electrode. The electrical insulation resistance value is obtained under three testing conditions – dry, wet, and dirty, as shown in Table 6 following the Design Standard for Railway Structure. In particular, the dirty condition is the most severe for electrical insulation among them. It simulates the condition where the dust accumulation on the rail fastening members in a wet environment causes a significant decrease in the electrical resistance on the surface of the members.

Figure 12 shows the test results. In this figure, the dotted line indicates the electrical resistance of design standard value of 1.6 kΩ defined as the required value of forming a track circuit for a set of

Fig. 11 Electrical resistance test

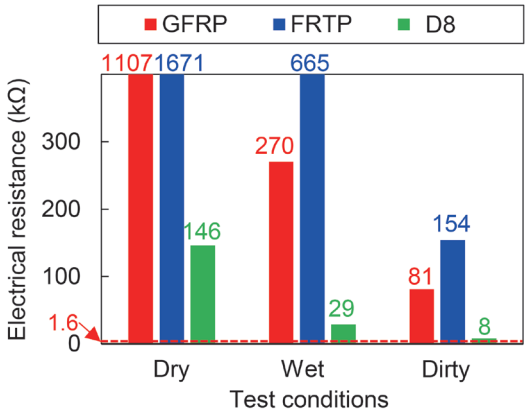

Fig. 12 Electrical resistance of rail fastenings

rail fastenings at the rail fastening intervals in Table 4.

The test results show that the electrical resistance values of the two kinds of prototype and existing D8 exceed the limit value under all test conditions. In particular, the resistance of the prototypes is ten times that of the D8 under the dirty condition.

These results show that the electrical insulation of the proposed prototypes is superior to that of the existing fastening assembly even under the most severe conditions, i.e., with dirt.

6. Conclusions

In this paper, the authors conducted a feasibility study on applying non-metallic materials to the main members of rail fastening systems. The authors proposed and prototyped the CFRP rail clip, and a GFRP and FRTP baseplate. Performance tests of the rail fastening system assembled with the proposed FRP members were conducted to confirm fatigue and electrical resistance. Test results indicated that the prototype of the rail fastening systems can be installed on conventional track. However, the spring coefficient of the CFRP rail clip should be justified by refining its shape, and it is necessary to grasp the material degradation properties of the non-metallic members for accurate evaluation. In future work, the authors will aim to resolve the above issues and optimize the shape of fastening members for application to sections with sharper curves.

Table 6 Test conditions

Test condition	Sprayed or not	Sprayed with:
Dry	Without	Not sprayed
Wet	With	Tap water
Dirty	With	Saline water (0.1% concentration)

Acknowledgment

Some of the results of this research have been obtained in collaboration with Toray Industries, Inc., Toray Carbon Magic Co., Ltd., and Nihon Composite Industries, Inc. The authors would like to thank all parties involved.

References

[1] Railway Technical Research Institute, *Design Standards for Railway Structures and Commentary (Track Structures)*, pp. 31-78, Maruzen, 2012 (in Japanese).

[2] Tamagawa, S., Kataoka, H. and Deshimaru, T., "Practical model for rail tilting and its application to performance test of rail fastening system," *Journal of JSCE*, Vol. 7, pp. 1-14, 2019.

Authors

Atsushi MATSUO
Researcher, Track Structures & Components Laboratory, Track Technology Division
Research Areas: Rail Fastening Systems

Tadashi DESHIMARU, Dr.Eng.
Senior Researcher, Track Structures & Components Laboratory, Track Technology Division
Research Areas: Railway Rails, Rail Fastening Systems, Rail Fatigue Life

Yoshihiro MASUDA, Ph.D.
Researcher, Vibration-Isolating Materials Laboratory, Materials Technology Division
Research Areas: Organic Polymer Materials

Minoru SUZUKI
Senior Researcher, Vibration-Isolating Materials Laboratory, Materials Technology Division
Research Areas: Organic Polymer Materials, Rail Track Materials

Actual Condition Survey of the Effects of Aging and Accumulated Tonnage on the Load-bearing Capacity of PC Sleepers

Tsutomu WATANABE **Shintaro MINOURA**
Track Dynamics Laboratory, Railway Dynamics Division

Keiichi GOTO **Manabu IKEDA**
Structural Mechanics Laboratory, Railway Dynamics Division

Prestressed concrete (PC) sleepers have been treated as replacement track materials that are replaced each time deformation occurs. For this reason, so far, no criteria have been established for quantitative soundness assessment nor for replacement of these sleepers. In this research, to establish a new maintenance management system of PC sleepers, we collected aged PC sleepers to conduct a survey of aging deterioration, with various tests such as bending tests specified by Japanese Industrial Standards (JIS). Using the results, we evaluated the load-bearing capacity of aged PC sleepers through numerical analyses using a three-dimensional FEM model. Finally, we proposed a guideline for the service life of PC sleepers.

***Key words*:** *prestressed concrete sleeper, maintenance, service life, track*

1. Introduction

Prestressed concrete (hereafter referred to as PC) sleepers are an important and essential track component for high-speed operation, ride comfort, and stable transportation. PC sleepers in Japan were first installed on a trial basis in 1951. Since then, over 40 million sleepers have been built by the Japanese National Railways and the Japan Railways Group alone excluding private railway companies.

Although PC sleepers are generally expected to last approximately 50 years [1], in recent years, a large number of PC sleepers have exceeded this life span. This service life of 50 years is only a design period, and in reality, if there are no problems in operation, they can continue to be used. Nevertheless, it is certain that aging deterioration of PC sleepers will progress due to frequent train loads and environmental effects such as solar radiation, wind, and rain. As a result, there is concern that the number of PC sleepers with load-bearing performance problems will increase in the future. In addition, despite the large number of PC sleepers installed on commercial lines in Japan, the number of sleepers that can be replaced in one night's work is extremely limited. Consequently, there is a concern that at some point in the future, replacement work will not be able to keep up with the demand to replace a large number of PC sleepers which no longer satisfy load-bearing capacity performance in fast succession. Therefore, there is a need to set a quantitative service life in advance to shift to a planned maintenance management system in the future.

Based on this context, the authors have recently been evaluating the load-bearing capacity of PC sleepers to establish a new maintenance management system [2, 3]. These studies have clarified the tendency of deterioration in the load-bearing capacity of PC sleepers to some extent, but fall short of proposing a specific service life. Based on the above results, in this study, we collected a wide range of aged PC sleepers installed on commercial lines and focused on the following points:

(1) Conduct various mechanical tests specified in JIS (Japanese Industrial Standards) to understand the load-bearing capacity of PC sleepers;
(2) Evaluate the effects of physical properties of concrete and steel on load-bearing capacity by numerical analysis;
(3) Propose a reference service life for PC sleepers based on the results of a survey of actual conditions such as the load-bearing capacity of PC sleepers.

It should be noted that in this study, PC sleepers with deterioration such as frost damage and alkali-silica reaction were excluded.

2. Load-bearing capacity evaluation of PC sleepers based on mechanical tests

2.1 Evaluation method

2.1.1 Outline of a PC sleeper

Figure 1 shows an outline of PC sleepers. The target PC sleepers are Type 3 PC sleepers classified as 3PR and 3PO in JIS (Japanese Industrial Standards) E 1201 and JIS E 1202 respectively. The method of introducing prestress in 3PR is the pre-tension method, and that in 3PO is the post-tension method. The majority of PC sleepers in Japan are Type 3 PC sleepers installed on straight sections and curved sections with a radius of 800 m or more. The design standard strength of concrete is 49.1 N/mm^2. The 3PR sleepers use 12 PC steel strands, in which each strand consists of 3 steel wires that are twisted together to form one strand, and each wire has a diameter of 2.9 mm. The 3PO sleepers use 4 PC steel bars, in which each bar has a diameter of 10 mm. The 3PR sleeper has a top cover concrete of 25 mm and a bottom cover concrete of 30 mm, while the 3PO sleeper has a top cover concrete of 38 mm and a bottom cover concrete of 37 mm.

Table 1 shows the number of the PC sleepers tested: 70 3PR sleepers and 65 3PO sleepers. We mainly collected PC sleepers installed in multiple railway sections in urban areas.

2.1.2 Bending test specified in JIS E 1201 and JIS E 1202

Figure 2 shows an outline of the bending test specified in JIS E 1201 and JIS E 1202 [4, 5]. Positive and negative bending tests were conducted on the rail seat and center sections of the PC sleepers, respectively. The loading span was 700 mm. The flexural proof load P_{cr} and flexural fracture load P_u were obtained using Equations (1)

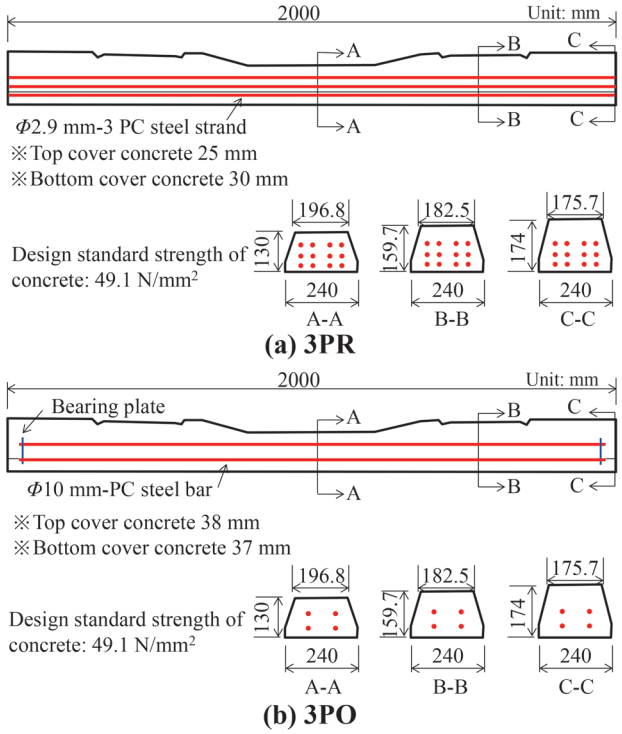

Fig. 1 Outline of PC sleepers

Table 1 Number of 3PR and 3PO PC sleepers

Aging (year)	~10	~20	~30	~40	~50	~60	合計
3PR	9	8	9	11	32	1	70
3PO	16	18	10	5	16	0	65

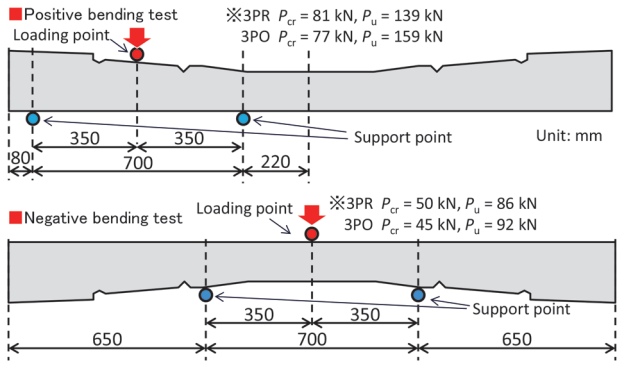

Fig. 2 Outline of bending test specified in JIS E 1201 and JIS E 1202

and (2), respectively. In the test, no cracks occurred when the P_{cr} was applied, and the PC sleepers did not break when the P_u was applied.

$$P_{cr} = 4 * (\sigma_{CPr} * 0.9 + f_{ta}) * Z / L \quad (1)$$

$$P_u = 4 * 3\sigma_{pe} * Z / L \quad (2)$$

where σ_{CPr} is the concrete stress due to the applied prestress force, f_{ta} is the allowable tensile stress (3 N/mm²), σ_{pe} is the concrete stress due to the effective prestress force (65% effective rate), Z is the section modulus, and L is the loading span (700 mm). Regarding test results, the relationship between aging and accumulative passing

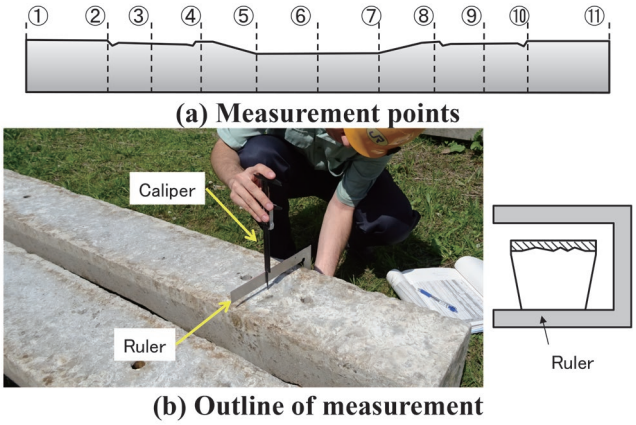

Fig. 3 Measurement test of wear on bottom surface of PC sleepers

tonnage (hereafter, the "passing tonnage") was determined for crack generation and ultimate loads. The crack generation load was the load at which a crack was first detected via visual observation. The ultimate load was the maximum load, past which the PC sleeper could no longer hold the load due to bending.

2.1.3 Compressive strength test and static elastic modulus test

In order to determine the compressive strength and static modulus of concrete for PC sleepers, a concrete compressive strength test specified in JIS A1108 and a static modulus test specified in JIS A1149 were carried out. The maximum diameter of the cylindrical specimen is 50 mm because it interferes with the PC steel stranded wire.

2.1.4 Compressive strength test and static elastic modulus test

Figure 3 shows the measurement points for wear on the bottom surface of PC sleepers. The wear on the bottom surface of PC sleepers was measured at three points widthways for each of the 11 cross sections shown in Fig. 3. There are 33 measurement points in total per PC sleeper. In addition, the results of measurement points that were clearly determined to be "chipped" rather than worn out by visual inspection were excluded.

2.2 Evaluation method

2.2.1 Bending test

Figures 4 and 5 show the positive bending test results for the rail seat section, including the flexural proof load P_{cr} and the flexural fracture load P_u. The figures indicated that the crack generation load and maximum load decreased gradually with increases in age and accumulative passing tonnage. The right vertical axes of these figures indicate the bending moments generated in the PC sleepers. In addition, the green data points in Fig. 4 shows the maximum bending moment of PC sleepers measured at a commercial line (which had been installed on a straight continuous welded rail section of a conventional line) [6]. The bending moment was obtained by converting the measured values of two strain gauges attached to the upper and lower edges of the PC sleepers.

Figures 6 and 7 show the negative bending test results at the center section of sleepers, including the flexural proof load P_{cr} and the flexural fracture load P_u. The results of the negative bending test

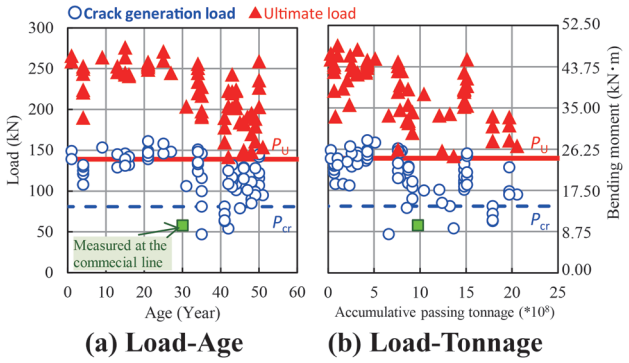

Fig. 4 Positive bending test results of 3PR sleepers at rail seat section

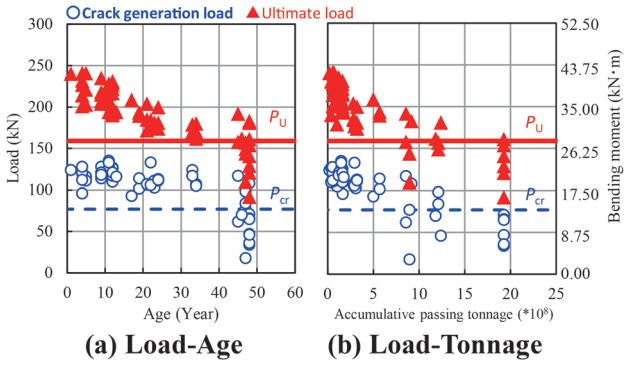

Fig. 5 Positive bending test results of 3PO sleepers at rail seat section

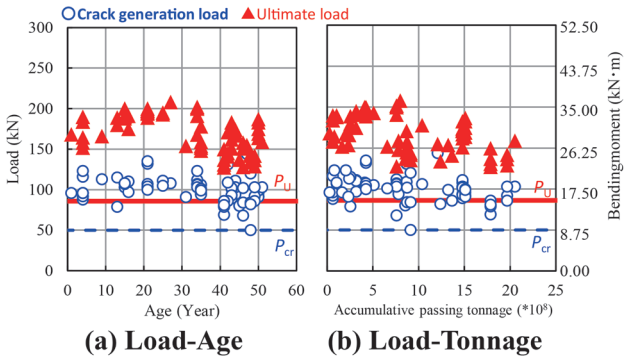

Fig. 6 Negative bending test results of 3PR sleepers at center section of sleepers

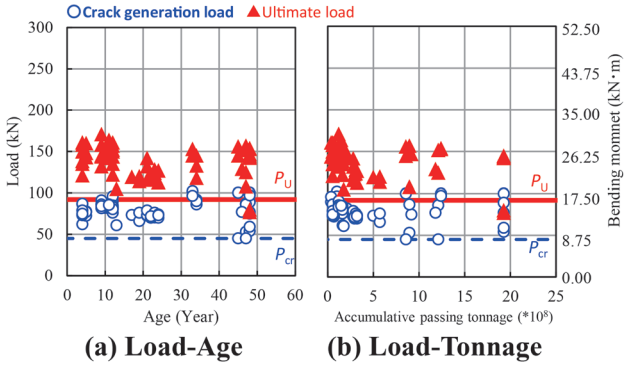

Fig. 7 Negative bending test results of 3PO sleepers at center section of sleepers

were arranged in the same manner as the positive bending test. All results of the 3PR PC sleepers exceeded the P_{cr} and P_u. Some results of the 3PO sleepers were lower than the P_{cr} and P_u, but the degree of decrease was smaller than that of the positive bending test.

2.2.2 Compressive strength test and static elastic modulus test

Figures 8 and 9 show the compressive strength test results and static modulus test results of concrete, respectively. Since there were no clear differences between the results of the 3PR sleepers and 3PO sleepers, they were plotted on the same graph. In addition, the figure shows the design standard strength of concrete for PC sleepers of 49.1 N/mm², and the static elastic modulus standard corresponding to the design standard strength of 33 kN/mm² shown in the Design Standards for Railway Structures and Commentary Concrete Structures [7].

2.2.3 Wear at the bottom surface of PC sleepers

Figure 10 shows the measurement results of the wear on the bottom surface of the PC sleepers. The amount of wear exceeding the bottom cover was not measured for the 3PR sleepers, but the amount of wear exceeding 40 mm was measured for the 3PO sleepers. It should be noted that the reason for the difference in the maximum wear due to the tensioning method cannot be clarified by this investigation alone, as we did not investigate the individual laying conditions of PC sleepers in detail. Thus, the investigation of the cause of this problem is a future issue.

However, when focusing on the maximum amount of wear around 40 years of age, despite a maximum value of 23 mm, there were also results which revealed only a small amount of wear, showing that there were very large variations. Therefore, it may not be rational to uniformly determine the service life by using a certain

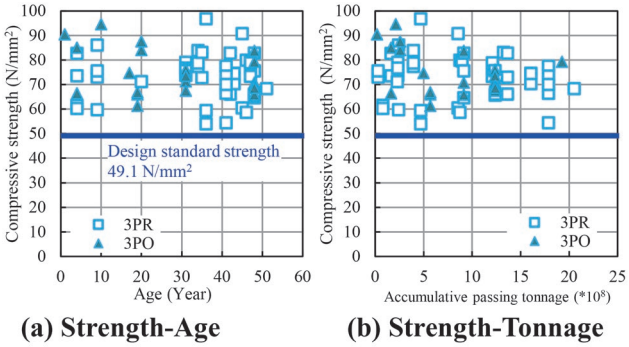

Fig. 8 Results of compressive strength test

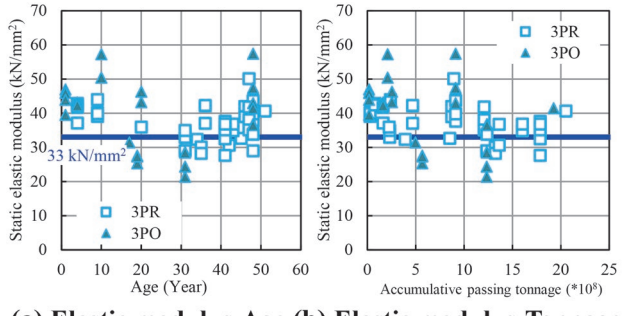

Fig. 9 Results of static elastic modulus test

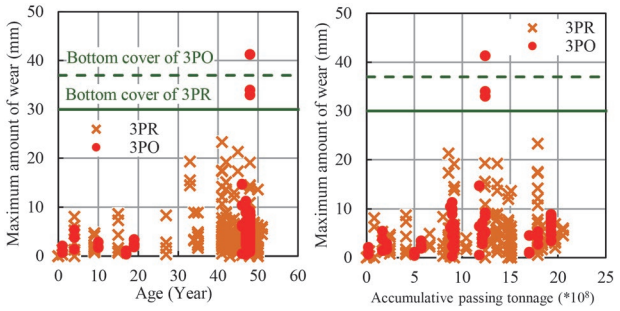

(a) Wear-Age (b) Wear-Tonnage

Fig. 10 Test results of wear on bottom surface of PC sleepers

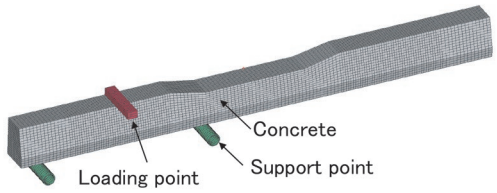

(a) Concrete, Loading and support point

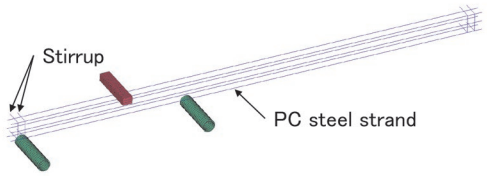

(b) PC steel strand and stirrup

Fig. 11 Outline of numerical analysis model

maximum wear amount as a threshold value.

3. Results of experiments

3.1 Evaluation method

3.1.1 Bending test

Figure 11 shows the outline of the numerical analysis model for a positive bending test at the rail seat section of a 3PR PC sleeper. The concrete, loading point and support point were modeled with 8-node solid elements, and the PC steel strands and stirrups were modeled with beam elements. Also, in order to reduce the analysis time, a 1/2 model was used, taking into account the symmetry of the structure. The standard element size was based on 10 mm, with a maximum size of no more than 20 mm. There was a total of 42,262 nodes in the entire analysis model, and a total of 34,856 elements. The PC steel strand and stirrup beam elements were modeled by embedding them in concrete elements. In the model, the nodes of the PC steel strand and stirrup beam elements were assumed to be completely attached to the concrete elements.

3.1.2 Material model

Table 2 shows the material constants used for the numerical analysis. The material constants of the concrete were set with reference to the unconfined compressive strength of the test piece and the design standard [7]. For the material constants of the PC steel stranded wire, the design standard values were used for the static elastic modulus and Poisson's ratio, and the mill sheet values were used for the yield strength and tensile strength.

Table 2 Material constants used for numerical analysis

Material	Static elastic modulus E (kN/mm^2)	Poisson's ratio	Compressive strength f'_c (N/mm^2)	Tensile strength f_t (N/mm^2)
Concrete	35.0	0.20	60.0	3.53
PC steel strand	200.0	0.30	Yield strength σ_y : 1500.0 Tensile strength σ_u : 1998.0	
Stirrup	200.0	0.30	Elastic body	
Loading and support point	Rigid body			

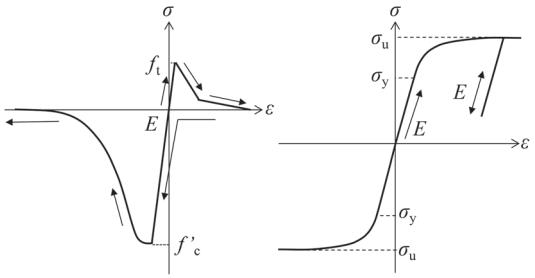

(a) Concrete (b) PC steel strand

Fig. 12 Material model

Table 3 Conditions for numerical analysis cases

	Value
Design standard strength of concrete (N/mm^2)	60, 50, 40, 30
Strength of PC steel strand (Magnification against σ_y, σ_u)	1.0, 0.9, 0.8, 0.7, 0.6
Effective prestress ratio (%)	100, 90, 80, 70, 60

Figure 12 shows the material model used in this analysis. Figure 12 (a) shows the uniaxial stress-strain relationship for concrete. On the compression side, the stress gradually softens as the strain increases after reaching the compressive strength [8]. However, on the tension side, the softening curve after reaching the tensile strength was approximated by two straight lines based on the tensile fracture energy of concrete [7]. Figure 12 (b) shows the uniaxial stress-strain relationship for PC steel strands. In this material model, the tensile test force-elongation relationship read from the mill sheet was converted into the stress-strain relationship and input, where f'_c is the compressive strength of the concrete, σ_y is the yield strength of the PC steel strand, σ_u is the tensile strength of the PC steel strand, f_t is the tensile strength of the concrete, and E is the static elastic modulus. The effective prestress rate of 75% in the analysis model was determined by trial and error so that the load-displacement relationship between the test results and the analysis results would be identical.

3.1.3 Numerical analysis cases

Table 3 shows the conditions for the numerical analysis cases. The design standard strength of concrete, the strength of PC steel, and the prestress ratio were set as parameters. Based on the results

in Section 2, it was assumed that these values fluctuated due to aging of materials and the frequent train loads. In order to verify the effect of this assumption on the load-bearing capacity, the values of the material strength were decreased. The static elastic modulus of concrete was set to a value corresponding to the design standard strength based on the design standard [7]. In addition, as a matter of course, it was assumed that these values might decrease in combination, but in this study, in order to understand the effect due to the individual factors, we decided to change the values individually.

3.2 Numerical analysis results

3.2.1 Validity of the numerical analysis model

Figure 13 shows a comparison of the test results with the analysis results. The test results were for three PC sleepers (tests 1, 2 and 3). As found in Fig. 13, by using the material constants shown in Table 2 and setting the effective prestress rate to 75%, the load-displacement relationship was accurately reproduced. It is also found that this figure includes the generation of the cracks, decrease in rigidity, load-bearing capacity (maximum load), and bending fracture.

3.2.2 Influences of the various parameters

Figure 14 shows the influences of the various parameters set in Table 3 on load-bearing capacity. As a matter of course, if the material strength and effective tension (prestress force) were reduced, the load-bearing capacity decreased. For example, when the compressive strength of the concrete decreases from 60 N/mm^2 to 30 N/mm^2, the maximum load decreased from 197.3 kN to 156.0 kN (reduction of 20%); when the strength of the PC steel decreased by 60%, the maximum load decreases from 197.3 kN to 146.3 kN (reduction of 26%); and when the effective prestress decreased from 100% to 60%, the maximum load decreased from 213.7 kN to 183.0 kN (reduction of 15%). As described in Chapter 2, the reason why the maximum load in the bending test results decreased due to aging and the increasing of the accumulative passing tonnage, and the reason there were PC sleepers that did not satisfy the JIS standard values despite being factory products, was potentially a decrease in their material strength. However, the evaluation of the influence of the combined deterioration of concrete and prestressing steel, the elucidation and the verification of phenomena related to the effects on material strength due to the frequent train loads were left as future tasks.

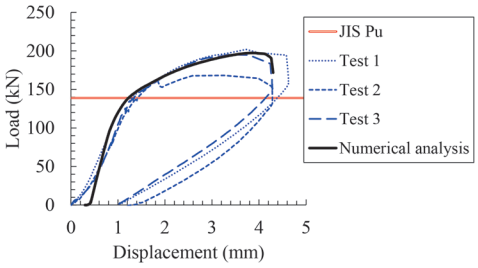

Fig. 13 Comparison of test results with analysis results

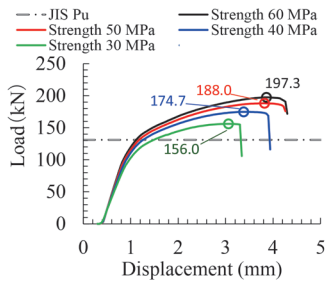

(a) Strength of concrete

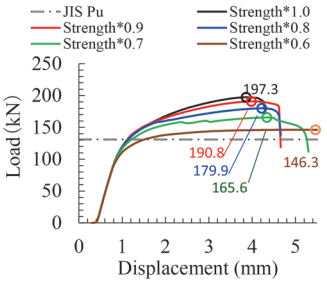

(b) Strength of PC steel strand

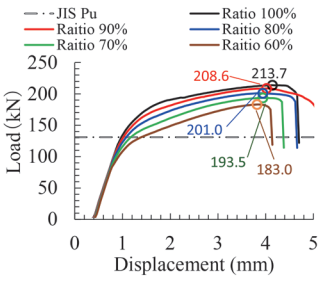

(c) Effective prestress ratio

Fig. 14 Influences of various parameters

4. Proposal for a reference service life for PC sleepers

Figure 15 shows the reference service life of 3PR PC sleepers and 3PO PC sleepers based on the results in Chapter 2. Accumulative passing tonnage, in which the approximation straight line of the maximum load in the positive bending test of the rail seat section was below the JIS standard value P_u, was proposed as the reference service life. The reasons for this are as follows: (1) From Fig. 4 to Fig. 7, it was observed that the crack generation load and the maximum load tended to decrease over time, but it was unreasonable to manage the high transport density railway sections in urban areas and low transport density railway sections in rural areas over the same period of time, (2) In the negative bending test of the center section of the PC sleeper, almost no results fell below the JIS standard value P_u, (3) All compressive strength of the concrete exceeded the design standard strength, (4) There was no standard value for the static modulus of elasticity, and (5) It was extremely rare to measure wear that exposed the PC steel wire.

Table 4 shows the reference service life of PC sleepers arranged from the above viewpoints. Specifically, it is a proposal of 3 billion tons for 3PR PC sleepers, and 1.2 billion tons for 3PO PC sleepers.

5. Conclusions

The findings from this study are summarized as follows:

(1) The bending test of aged PC sleepers (3PR, 3PO) revealed that both the crack generation load and the maximum load tended to

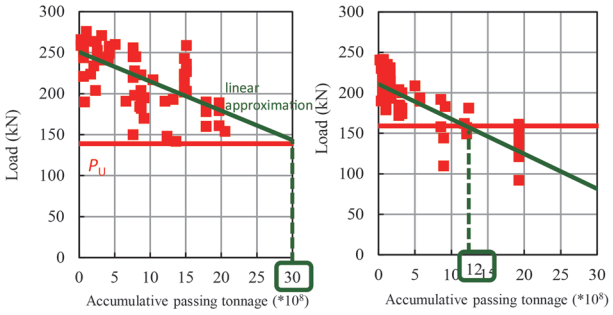

Fig. 15 Reference service life

Table 4 Reference service life of PC sleepers

Type	Reference service life (*10^8 ton)
3PR	3
3PO	1.2

decrease with aging and accumulative passing tonnage.

(2) As a result of numerical analysis, the reason why the maximum load in the bending test results decreased due to aging and the accumulative passing tonnage was potentially a decrease in material strength. The same reason may also be responsible for the existence of PC sleepers that did not satisfy the JIS standard values, despite being factory products.

(3) Based on the results of the tests and the survey of aged PC sleepers, the reference service life of PC sleepers were suggested. Specifically, it is a proposal of 3 billion tons for 3PR PC sleepers, and 1.2 billion tons for 3PO PC sleepers.

We will continue to investigate aged PC sleepers to understand changes in load-bearing capacity. In addition, we will pursue research to elucidate the mechanism underlying aging deterioration of PC sleepers.

References

[1] FIP Commission on Prefabrication, *FIP State of the Art Report (Concrete Railway Sleepers)*. Thomas Telford Ltd.: London, UK, 1987.

[2] Watanabe, T., Goto, K., Minoura, S., "Investigation of Load Environment and Bending Load Capacities of Aged Prestressed Concrete Sleepers," *Applied Sciences*. 2023; 13(13): 7828.

[3] Goto, K., Watanabe, T., Minoura, S., Ikeda, M., "Fatigue Life Evaluation of PC Sleepers Based on Wheel Load Measurement Results," *Quarterly Report of RTRI*, Vol. 63, No. 4, pp. 263-268, 2022.

[4] JIS E1201, *Prestressed Concrete Sleepers-Pretensioning Type*, Japanese Standards Association, Tokyo, Japan, 1997.

[5] JIS E1202, *Prestressed Concrete Sleepers-Posttensioning Type*, Japanese Standards Association, Tokyo, Japan, 1997.

[6] Watanabe, T., Goto, K., Matsuoka, K., Minoura, S., "Validation of a dynamic wheel load factor and the influence of various track irregularities on the dynamic response of prestressed concrete sleepers," *Proc. IMechE Part F J. Rail Rapid Transit*, Vol. 234, pp. 1275-1284, 2020.

[7] Railway Technical Research Institute, *Design Standards for Railway Structures and Commentary (Concrete Structures)*, Maruzen Co., Ltd.: Tokyo, Japan, 2007.

[8] Grasse, P., "CDPM2: A damage-plasticity approach to modelling the failure of concrete," *International Journal of Solids and Structures*, Vol. 50, Issue 24, pp. 3805-3816, 2013.

Authors

Tsutomu WATANABE, Dr.Eng.
Senior Chief Researcher, Head of Track Dynamics Laboratory, Railway Dynamics Division
Research Areas: Concrete Sleeper, Numerical Simulation, Structure-borne Noise, Vibration

Keiichi GOTO, Dr.Eng.
Senior Researcher, Structural Mechanics Laboratory, Railway Dynamics Division
Research Areas: Dynamic Interaction between Vehicle and Bridge, Post-derailment Vehicle Behavior, Numerical Simulation

Shintaro MINOURA, Dr.Eng.
Assistant Senior Researcher, Track Dynamics Laboratory, Railway Dynamics Division
Research Areas: Concrete Sleeper, Numerical Simulation

Manabu IKEDA, Dr.Eng.
Senior Chief Researcher, Structural Mechanics Laboratory, Railway Dynamics Division
Research Areas: Hybrid Structures, Steel Structures

Rail Profile Selection Method to Reduce Gauge Corner Cracking Initiation

Masahiro TSUJIE **Masaharu KONO**
Track Dynamics Laboratory, Railway Dynamics Division

Yoshiaki TERUMICHI
Sophia University

Gauge corner cracking (GCC) occurs on heat treated rails on the high rail of curved sections with a radius of 600 to 800 m. Deep GCC propagation may cause rail breakage. It is therefore very important to prevent the occurrence of GCC to ensure safe railway operation. Previous research has proposed a countermeasure method to suppress the occurrence of GCC by applying rail wear profiles to the high rail of curved sections to relieve contact pressure between the wheel/rail. Since the wear development of rails is closely related to wheel/rail contact conditions, rail wear profile prediction becomes complex due to the variety of contact conditions. The aim of this study is to examine the rail cross-sectional profile that is the most effective in suppressing crack initiation for the high rail of curved sections with a radius of 600 to 800 m where the occurrence of GCC is a concern.

***Key words*:** *wear development, fatigue index, wheel/rail, multibody dynamics, machine learning*

1. Introduction

In Japan, gauge corner cracking (GCC) occurs at the gauge corners of heat treated rails laid on high rail in curved section with a radius of 600 to 800 m (see in Fig. 1). Like rail squats, GCC is a fatigue crack that originates from a fatigue layer accumulated on rail surfaces due to wheel/rail rolling contact. If GCC propagates deeply, it will cause rail defects. Although countermeasures have been taken to detect the occurrence of GCC using ultrasonic flaw detection, preventive measures against GCC have not been established. Previous research [1] has reported that the risk of fatigue crack initiation can be reduced by reducing wheel/rail contact pressure. In addition, the authors have proposed a countermeasure method for suppressing the occurrence of GCC by applying rail wear profiles to the high rail of curved sections to suppress wheel/rail contact pressure [2]. Since wear development is closely related to wheel/rail contact conditions, prediction of rail wear profiles is complex due to the variety of contact conditions. Therefore, to implement this method on an actual line in service, it is necessary to predict the wear profile for each location individually. The aim of this study is to examine the optimal rail profile that is most effective in suppressing crack initiation for high rails in curved sections with a radius of 600 to 800 m where the occurrence of GCC is a concern. A proposal for suitable rail profiles which can suppress GCC for various curve radii should eliminate the need to consider individual construction methods depending on construction location, leading to the development of a heat treated rail with a new profile that is effective in suppressing the occurrence of GCC. This study investigates a method for selecting the rail profile with the highest crack suppression by using machine learning to search for rail profiles that alleviate wheel/rail contact conditions.

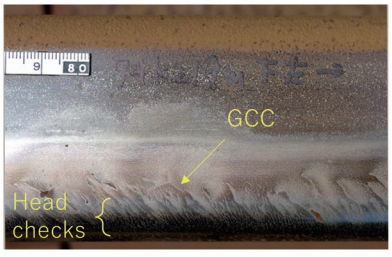

Fig. 1 The examples of GCC appearance on rail

2. Crack initiation evaluation

A method for evaluating rolling contact fatigue (RCF) cracks such as rail squats or GCC by a fatigue index (FI) based on shakedown theory [3][4] has been proposed in previous research [5]. In this theory, RCF depends on the contact pressure and creep force between the wheel/rail. When the contact stress exceeds the shakedown limit, RCF cracks will occur due to accumulation of plastic strain. The relationship between wheel/rail contact conditions and the shakedown limit can be explained using the shakedown diagram. Furthermore, the fatigue index of FI model is obtained in (1).

$$FI = \frac{\sqrt{F_x^2 + F_y^2}}{F_z} - \frac{k_s}{p_0} \tag{1}$$

where F_x and F_y are the longitudinal creep force and lateral creep force respectively. F_z is the contact force between wheel/rail. Furthermore, k_s is the rail material yield stress in shear and p_0 is the maximum contact pressure.

The crack initiation prevention effect is assumed by the reduction of the value of FI which is described above. As for preventive methods for crack initiation, previous research includes the following methods [1]:

- The reduction of the contact stress by controlling the contact geometry
- Increasing the material resistance k_s by introducing materials with a higher yield limit
- The reduction of friction loads by lubrication

In a previous paper [2], the authors proposed a method for reducing wheel/rail contact pressure and the occurrence of GCC by applying a worn profile to high rails in curved sections with a radius of 800 m where GCC is likely to occur.

3. Wear development analysis

In this chapter, in order to accumulate rail wear profile data and fatigue indexes that will be used as training data for selecting the optimal profile to suppress the GCC initiation, a wear development analysis using a multibody dynamics method was applied to a curved section with a radius of 600 m to 800 m.

3.1 The outline of the wear development analysis

The rail wear analysis was carried out using a multibody dynamics prediction model. The analysis flow of this model is shown in Fig. 2.

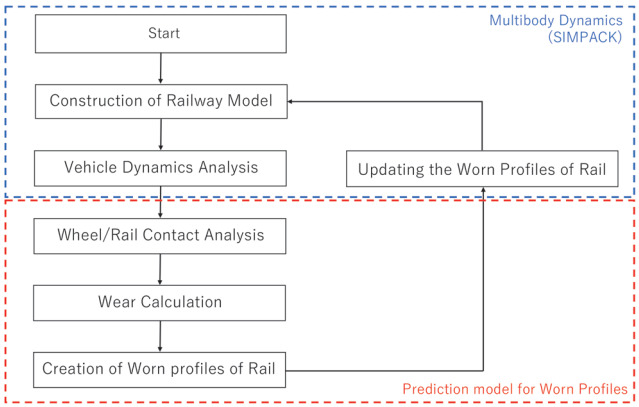

Fig. 2 Flow chart of the wear development analysis

This model consists of the vehicle dynamics analysis using multibody dynamics tool "Simpack" and the wear prediction model. Firstly, the vehicle and track models are constructed in Simpack. Then, the vehicle dynamics analysis is carried out using these models. Secondly, the details of the wheel/rail contact conditions are calculated for each section of the track model. According to the results of the contact conditions, the wear volume of the rail at each section are calculated by Archard's wear law in (2). The wear profiles of the rail are obtained from the wear depth and the rail profiles in the track model. Finally, the rail wear profiles are updated in the track model at each section. By repeating this procedure, the changed rail profiles for each section and time series are obtained. In this research, the update of the wear profiles was repeated 15 times as shown in Fig. 2. The number of the wear profiles updated is indicated by n. This means that, the update number for the design profiles is n=0. Furthermore, in the previous research, k_w=1.73×10^{-4} is identified by the results of the laboratory test [6].

$$W = \frac{k_w \cdot F \cdot S}{H} \tag{2}$$

3.2 Analysis conditions

The track model of wear development analysis was constructed for a curved section with a radius of 600 m ~ 800 m where GCC appearance was observed on an actual line. The details of the track model are shown in Fig. 3 and Table 1.

The vehicle model was constructed to simulate standard vehicles with modified arc wheel treads operated in commuter lines. The vehicle speed in the analysis was set to 105 km/h, which is the same as in actual operating conditions.

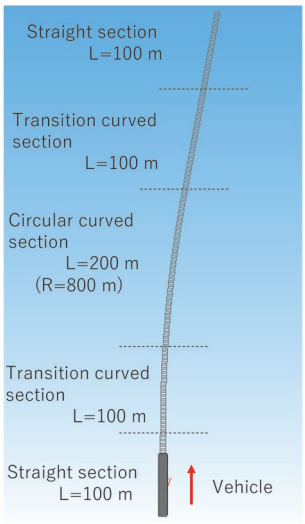

Fig. 3 The outline of the track model (wear development analysis)

Table 1 The specifications of the track model of the wear development analysis

Case	1	2	3
Curve radius [m]	600	700	800
Cant elevation [mm]	105		
Gauge [mm]	1067		
Gauge widening [mm]	0		
Rail profile	JIS 60 kg		

3.3 Analysis results

The analysis results of the wear profiles of the high rail on the curved section are shown in Fig. 4 according to updated numbers. Note that, in Fig. 4, the horizontal axis shows the distance from the center of the rail to the gauge corner side.

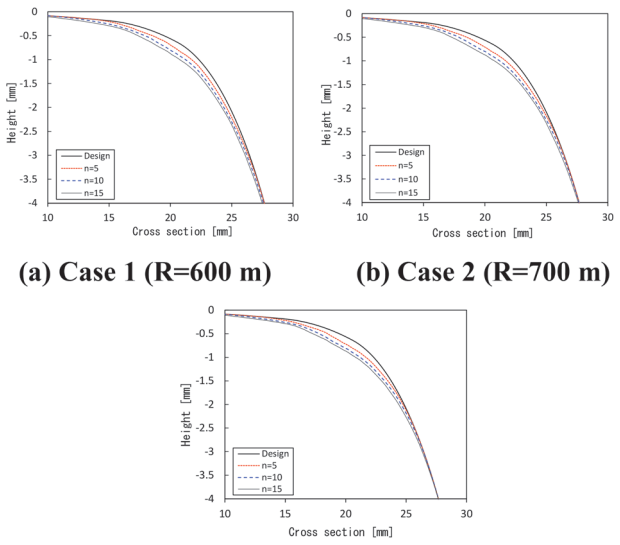

(a) Case 1 (R=600 m) **(b) Case 2 (R=700 m)**

(a) Case 3 (R=800 m)

Fig. 4 The results of wear development analysis

As shown in Fig. 4, the wear profiles at each radius have been predicted. These predicted wear profiles will be utilized for the wheel/rail contact analysis in the next chapter.

4. Crack initiation evaluation for the worn profile

In this chapter, as in the previous chapter, a wheel/rail contact analysis was carried out using the rail wear profiles calculated from the wear development analysis in order to accumulate training data for machine learning. Furthermore, the FI model described in Chapter 2 was used to evaluate the influence of rail wear profiles on crack initiation.

4.1 Analysis conditions

As in the previous chapter, a wheel/rail contact analysis was carried out using Simpack (ver.2019) for curved sections with a radius of 600, 700, 800 m where GCC appearance had been confirmed. However, for the high rail on the circular curved section, the design profile (n=0) and the 15 updated wear profiles (n=1~15) obtained from the wear development analysis in the previous chapter were placed (Fig. 5). Table 2 shows the analysis conditions for the wheel/rail contact analysis conducted in this section.

As shown in Table 2, in order to accumulate training data for selecting the rail profiles that are highly effective in suppressing GCC initiation by machine learning, wheel/rail contact analyses were carried out for cases with other curve radii in addition to the curve radii in the previous chapter. In other words, the wear development analysis in the previous chapter was conducted with a radius of 600 m (the worn profiles (n=1 to 15) obtained from the analysis of case 1 in the previous chapter and the design profile (n=0)). The wheel/rail contact analysis is applied not only to curved sections with a radius of 600 m (case 4-a shown in Table 2) , but also to curved sections with a radius of 700 m (case 5-a shown in Table 2) and 800 m (case 6-a shown in Table 2). Similarly, regarding the wear profiles on curved sections with a radius of 700 m and 800 m, wheel/rail contact analyses were also applied to curved sections with different radii from the wear development analysis. Furthermore, according to the results of contact conditions obtained from the contact analysis (approximately 20 to 22 mm from the center of the rail top to the gauge corner side), the crack initiation was evaluated using the FI model described in Chapter 2.

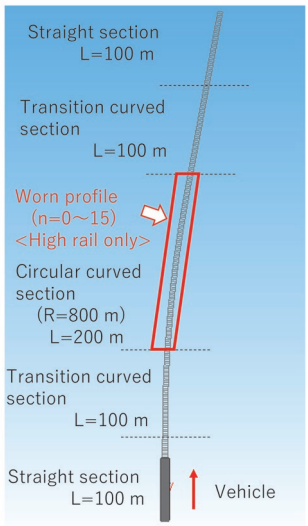

Fig. 5 The outline of the track model (wheel/rail contact analysis)

4.2 Evaluation of crack initiation

The fatigue index of the high rail on the circular curved section was calculated from the results of the wheel/rail contact analysis carried out under the conditions described in Table 2. The shear strength k_s in (1), 1200 N/mm^2 was adopted as the value for the heat treated rail material. The results are shown in Fig. 6 for each of analysis conditions (case 4 to 6) shown in Table 2. In both figures, the horizontal axis is the number of updates n of the profiles in the wear development analysis. In addition, in the case of multi-point wheel/rail contact, the highest value of the fatigue index was adopted for a safer evaluation.

As shown in Fig. 6, when the worn profile is applied to the high rail of each curved section, the fatigue index tends to decrease compared to the designed profile (n=0). In particular, this tendency was more noticeable in case 5 with a radius of 700 m and case 6 with a radius of 800 m. On the other hand, the multiple results shown in cases 4 and 5 (for example, the results for n=8 in case 4-a and the results for n=14 in case 4-b and case 5-b) indicate that there is multiple contact between the wheel/rail. This is because under a contact condition where the local contact pressure is high, the value of the

Table 2 The specifications of the track model of the wheel/rail contact analysis

Case	4-a	4-b	4-c	5-a	5-b	5-c	6-a	6-b	6-c
Curve radius [m]	600			700			800		
Cant elevation [mm]	105								
Gauge [mm]	1067								
Gauge widening [mm]	0								
Rail profile (Curved section in high rail)	Design (n=0) or Worn Case 1 (n=1~15)	Design (n=0) or Worn Case 2 (n=1~15)	Design (n=0) or Worn Case 3 (n=1~15)	Design (n=0) or Worn Case 1 (n=1~15)	Design (n=0) or Worn Case 2 (n=1~15)	Design (n=0) or Worn Case 3 (n=1~15)	Design (n=0) or Worn Case 1 (n=1~15)	Design (n=0) or Worn Case 2 (n=1~15)	Design (n=0) or Worn Case 3 (n=1~15)
Rail profile (Other sections)	JIS 60 kg								

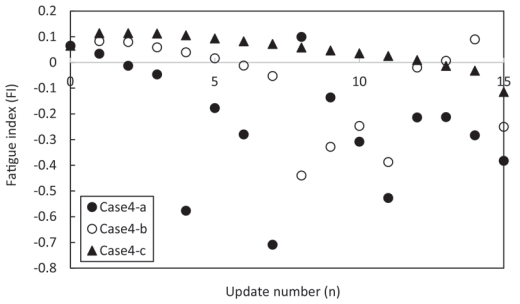

(a) Case 4

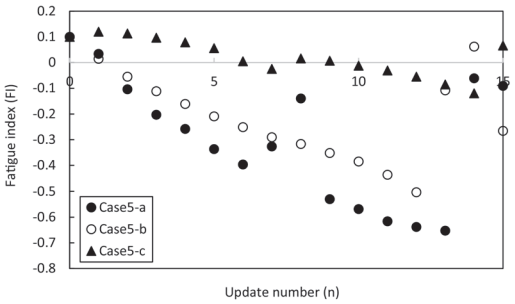

(b) Case 5

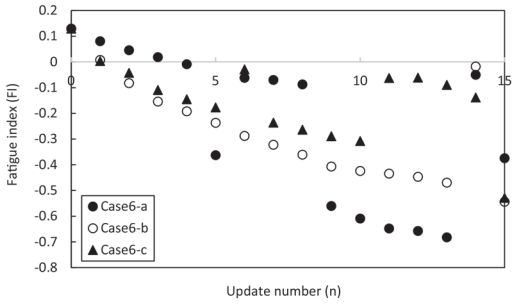

(c) Case 6

Fig. 6 The analysis results of fatigue index

fatigue index increases.

As a general trend, except for some conditions, the fatigue index calculated from the contact conditions with the wear profile to the curved sections (Fig. 6 (a) to (c)) tends to decrease compared to the fatigue index with the design profile.

5. Method for selecting rail profile with high crack suppression effect by machine learning

In this chapter, we attempted to select the most effective rail profile to suppress crack initiation for any curve with a radius of 600 to 800 m by machine learning using the wear profiles (Fig. 4) from the wear development analysis in Chapter 3 and the fatigue index (Fig. 6) calculated from the wheel/rail contact analysis in Chapter 4 as training data. However, if the wear profiles obtained in Chapter 3 are uniformly used as training data for machine learning, a non-smooth uneven profile that combines wear profiles at various curve radii is the optimal solution, which is unsuitable for the wheel/rail contact possibly causing abnormal contact conditions such as multi-point contact or localized high contact pressure.

Therefore, in this study, it was decided to search for the optimal rail profile with a high crack suppression effect for each curve radius, instead of treating the predicted wear profile for each curve radius all at once. This method is expected to avoid the creation of a unique profile that combines the wear profile with various curve radii or the unique wheel/rail contact, as the candidate profile is based on the wear profile explored using a single curve radius model. Therefore, an optimal rail profile with a high crack initiation suppression effect was selected following four steps described below, including the wear development analysis in Chapter 3 and the wheel/rail contact analysis in Chapter 4.

- Predicting wear profiles for each curve radius
- Calculating the fatigue index under each contact condition using wheel/rail contact analysis with the predicted wear profiles
- Searching for the profile with the lowest fatigue index using machine learning with the wear profiles at each curve radius
- From the candidate profiles in the previous step, selecting the optimal profile that is effective in reducing the fatigue index for all curve radii

The scheme from 1 to 3 are shown in Fig. 7, and the scheme 4 is shown in Fig. 8. The details of each step are also described below.

(Step 1)

Firstly, wear profiles for circular curved sections with a radius of 600 to 800 m were predicted using the wear development analysis described in Chapter 3. Figure 7 shows the wear profiles with radii of 600, 700 and 800 m (n=0 to 15) predicted by this procedure.

(Step 2)

Secondly, the wheel/rail contact analysis was carried out by applying the rail wear profile obtained in the previous step to a high rail in a curved section, and the fatigue index was calculated. As described in Chapter 4, the fatigue index calculated from the wheel/rail contact analysis is used as training data in machine learning. Therefore, in addition to the curve radius modeled in the wear development analysis, the wheel/rail contact analysis was also carried out for other curve radii. The calculated fatigue indexes corresponds to $FI\_^{1}_{2}(1)$ and $FI\_^{3}_{1}(2)$ in Fig. 7. Hence, $FI\_^{1}_{2}(1)$ in Fig. 7 is the fatigue index of the wear profile updated once (n=1) for the wear development analysis with a radius of 600 m, and applied to a high rail with a radius of 700 m. Similarly, $FI\_^{3}_{1}(2)$ shows the fatigue index of the wear profile updated twice (n=2) for the wear development analysis with a radius of 800 m, and applied with a radius of 600 m. In this study, the wear development analysis was carried out for three curve radii of 600, 700 and 800 m, and the worn profile was updated 15 times (n=1 to 15) for each condition and the wheel/rail contact analysis was carried out for the same three curve radii. Therefore, data for 48 rail profiles (n=0 is the designed profile, so it has the same profile) and 144 of the fatigue indexes associated with profiles (n=0 has the same profile, so the fatigue index is the same value) are calculated.

(Step 3)

As mentioned at the beginning of this chapter, there is a possibility that a rail profile combining the profiles with various curve radii, which is uneven or not-smooth, may converge as the optimal solution in the profile search, by treating the 48 profiles data and 144 fatigue indexes obtained in step 2 as a whole. In order to avoid these problems, machine learning was carried out to search for the optimal profile for each curve radius, using the wear profiles of the same curve radius and the corresponding fatigue indexes as training data.

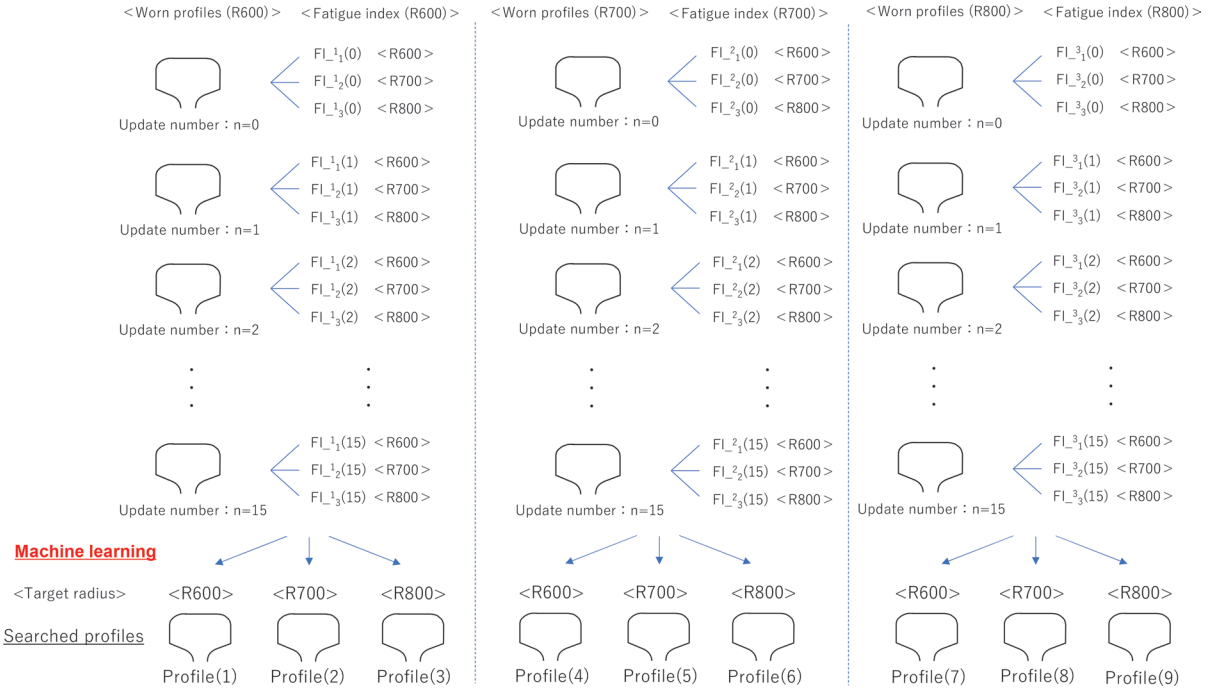

Fig. 7 Scheme for searching for candidate rail profiles

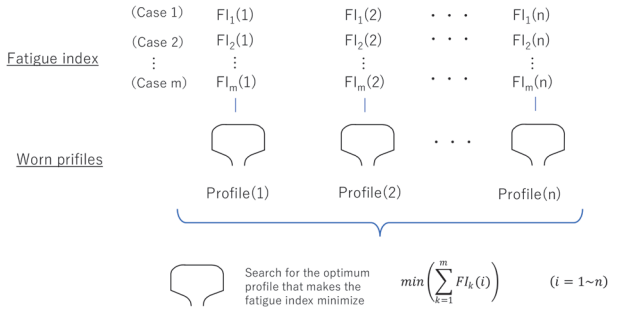

Fig. 8 Scheme for searching for optimal profile from candidate profiles

In other words, machine learning was carried out to search for the profile with the lowest fatigue index when applied to curves with a radius of 600, 700 and 800 m using 16 wear profiles (n=0 to 15) predicted by the wear development analysis in which a curved section with a radius of 600 m was modeled and 48 fatigue indexes $FI\_^{1}_{1}(1)$ to $FI\_^{1}_{3}(15)$ corresponding to each profile used as training data. Let the profiles obtained by machine learning be profile (1), profile (2) and profile (3) respectively (Fig. 7). Similarly, machine learning was carried out to search for the profiles with the lowest fatigue index using the predicted wear profiles of 700 and 800 m radius and their fatigue index, so we obtained six profiles, i.e. profile (4) to profile (9). The machine learning in this study was carried out by neural networks constructed with 5 layers.

(Step 4)

Finally, the fatigue indexes ($FI_1(1)$ to $FI_m(n)$) (see in Fig. 8) were calculated from the wheel/rail contact conditions on the high rail of circular curves, where nine profiles (profile (1) to profile (9)) obtained in step 3 were applied to the three curved sections with a radius of 600, 700 and 800 m as shown in Fig. 5. In this study, as mentioned above, there are three types of curve radii and nine profile candidates, so m=3 and n=9 in Fig. 8. As shown in Fig. 8, the applicability of the candidate profile for the curved section is obtained by calculating the sum of the fatigue index under each condition as shown in the following (3). In other words, when applying the candidate profiles to three curved sections with radii of 600, 700 and 800 m, if the crack suppression effect is high for all curve radii, the calculated sum of fatigue indexes will be low. Conversely, if the crack suppression effect is low, the total fatigue indexes will be high.

$$FI_t = \sum_{k=1}^{m} FI_k(i) \qquad (i = 1 \sim n) \tag{3}$$

where FI_t is the sum of fatigue indexes and $FI_k(i)$ is the fatigue index calculated by applying each profile.

It is possible to select the optimal rail profile with the highest crack suppression effect for any curve radius by the sum of the fatigue indexes calculated under various conditions. For the nine candidate profiles shown in Fig. 7, the wheel/rail contact analysis was carried out for each of the three curved sections with radii of 600, 700 and 800 m as shown in Fig. 5 to calculate the fatigue index for each curve radius. In addition, the sum of the fatigue indexes applied to the three curved sections with radii of 600, 700 and 800 m is given by (3). The results of the total effective fatigue index are shown in Fig. 9. For comparison, the results of applying the JIS 60 kg profile under the same conditions are shown.

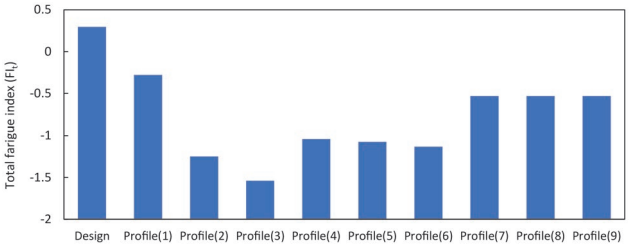

Fig. 9 The analysis results of the total fatigue index

Figure 9 shows that all of the nine candidate profiles investigated in this study have the effect of suppressing crack initiation because these candidate profiles given by (3) have lower total effective fatigue indexes than the result of the JIS 60 kg profile. In particular, profile (3) has the highest suppression effect on crack initiation of the nine candidate profiles in this study because its total effective fatigue index is the lowest.

6. Conclusions

This study proposed rail profiles for multiple curve radii which suppress crack initiation at the gauge corners, which are the starting points of GCC. Machine learning was carried out using the results of wear development analysis and the fatigue indexes as training data. Finally, an optimal profile for the high rail of curved sections with a radius of 600 m to 800 m was proposed.

References

[1] Ekberg, A., and Kabo, E., "Fatigue of railway wheels and rails under rolling contact and thermal loading -an overview," *Wear*, Vol. 258, pp. 1288-1300, March 2005.

[2] Tsujie, M., Okita, M. et al., "A study on the countermeasure method for gauge corner cracking by applying the worn profiles of rail," *Transaction of the JSME*, Vol. 88, No. 908, DOI:10.1299/transjsme.21-00327, 2022 (in Japanese).

[3] Johnson, K. L., "The strength of surfaces in rolling contact," *Proceedings of the Institution of Mechanical Engineers, Part C*, Vol. 203, pp. 151-163, May 1989.

[4] Bower, A. F. and Johnson, K. L., "Plastic flow and shakedown of the rail surface in repeated wheel-rail contact," *Wear*, Vol. 144, pp. 1-18, April 1991.

[5] Ekberg, A., Kabo, E., and Andersson, H., "An engineering model for prediction of rolling contact fatigue of railway wheels," *Fatigue & Fracture of Engineering Material & Structure*, Vol. 25, pp. 899-909, September 2002.

[6] Tsujie, M., Okita, M. et al., "Development of a model for predicting worn profile of rail under mixed slip conditions," *Transaction of the JSME*, Vol. 86, No. 891, DOI:10.1299/transjsme.20-00056, 2020 (in Japanese).

Authors

Masahiro TSUJIE, Ph.D.
Senior Researcher, Track Dynamics Laboratory, Railway Dynamics Division
Research Areas: Wear Development, Crack Initiation, Multibody Dynamics

Masaharu KONO
Researcher, Track Dynamics Laboratory, Railway Dynamics Division
Research Areas: Wear Development, Crack Initiation, Adhesion

Yoshiaki TERUMICHI, Ph.D
Professor, Department of Engineering and applied Science, Faculty of Science and Technology, Sophia University
Research Areas: Multibody Dynamics, Wheel/rail Contact, Pattern Formation

Summaries of Papers in RTRI REPORT (in Japanese)

Outline of Revised Design Standard and Commentary for Railway Structures (Concrete Structures)

Ken WATANABE, Toshiya TADOKORO, Manabu IKEDA, Masaru OKAMOTO
(Vol.37, No.11, 1-5, 2023.11)

Design Standard and Commentary for Railway Structures (Concrete Structures) was revised in January of 2023. In this revision, in addition to reorganization of the previous design standards established mainly for each type of structure and material, the introduction of the latest verification techniques results in making the design standards easier to use. The application of the revised design standard to design practice will lead to realizing superior railway structures.

Design Standard and Commentary for Railway Structures (Concrete Structures) "Outline of Part I: General Principles"

Toshiya TADOKORO, Ken WATANABE, Manabu IKEDA, Masaru OKAMOTO
(Vol.37, No.11, 7-13, 2023.11)

The functional requirements for a railway system that railway structures must satisfy are the same regardless of the type of structure, such as bridges, earth structures, and tunnels. Therefore, in order for railway structures to function as members of a railway system, "Design Standard and Commentary for Railway Structures (Concrete Structures), Part I: General Principles" was established, which includes the basic policy of railway structure design by unifying the general items such as design concepts, performance requirements, and verification for all structures that compose the railway system.

Design Standard and Commentary for Railway Structures (Concrete Structures) Outline of "Part II: Bridge Structures"

Ken WATANABE, Manabu IKEDA, Masaru OKAMOTO
(Vol.37, No.11, 15-23, 2023.11)

This paper outlines Design Standard and Commentary for Railway Structures (Concrete Structures) "Part II: Bridge." All technology related to the design of railway bridges is summarized in this Part II, which have been described commonly into related design standards. By developing "Part II: Bridge," the detail of bridge dimension is optimized, not optimized only beams, columns, foundations, and other members. In addition, it supports to address compatibility with society and to evaluate redundancy and robustness.

Design Standard and Commentary for Railway Structures (Concrete Structures) Outline of "Part III: Concrete Structure"

Ken WATANABE, Yuki NAKATA, Shuntaro TODOROKI
(Vol.37, No.11, 25-33, 2023.11)

Design Standard and Commentary for Railway Structures (Concrete Structures) "Part III: Concrete Structure" summarizes interpretations of the verification described in Part II: Bridge, as well as concrete structure-specific techniques: materials, structural analysis methods, member verification, load-bearing capacity formulas, etc. that can be used as reference in the verification. The latest information is introduced, such as formulas, values, etc., which have been published through actual results, specifications, and papers, and have been verified and validated in the committee meetings.

Design Standard and Commentary for Railway Structures (Concrete Structures) Outline of Part IV: Bearing Structures

Manabu IKEDA, Toshiya TADOKORO, Shuntaro TODOROKI, Akihiro TOYOOKA
(Vol.37, No.11, 35-40, 2023.11)

This paper outlines the Design Standard and Commentary for Railway Structures (Concrete Structures) "Part IV: Bearing Structures." Every technology related to the design of bearing structures in railway bridges is summarized in this part, which has been described in several related design standards. This part provides common design methods for bearing structures, and specific design methods for three typical bearing structures: (a) rubber bearings and stoppers, (b)steel bearings, and (c)bearings for horizontal force dispersing structures and isolation structures. This paper introduces the outline of each chapter of this part and revisions from related design standards.

Trial Design of the RC Rigid Frame Viaduct Applying the Revised Standard for Railway Concrete Structures

Ryo SUZUKI, Katsunari ARAKI, Yuki NAKATA, Shuntaro TODOROKI, Ken WATANABE
(Vol.37, No.11, 41-44, 2023.11)

Based on previous research, the formulas and values in the Design Standard and Commentary for Railway Structures (Concrete Structures) have been revised. In this report, we compare RC rigid frame viaduct designed based on the revised standard (published in 2023) with those designed based on the current standard (published in 2004). Consequently, this comparison resulted in more rational design, for example, in the reduction rebar ratios by revising the shear strength equation of RC members and the specification for stirrup ratio in a joint.

Trial Design of the RC Pier Applying the Revised Standard for Railway Concrete Structures

Ryo SUZUKI, Katsunari ARAKI, Yuki NAKATA, Shuntaro TODOROKI, Ken WATANABE
(Vol.37, No.11, 45-48, 2023.11)

Based on previous research, the formulas and values in the Design Standard and Commentary for Railway Structures (Concrete Structures) have been revised. In this report, we compare RC piers designed based on the revised standard (published in 2023) with those designed based on the current standard (published in 2004). Consequently, this comparison resulted in more rational design, for example, in the reduction of reinforcing-bar ratio, by increasing applicability of yield strength of rebars and revising formulas for the shear strength of RC members and pile foundation.

Development of Safety Check Support Device for Driver Using Side Camera on Rolling Stock

Wataru GODA, Hiroki MUKOJIMA, Nozomi NAGAMINE
(Vol.37, No.12, 1-7, 2023.12)

This paper describes the development of a safety check support device to further enhance safety check on the platform using side cameras on rolling stocks. Utilizing deep learning-based image processing techniques, the developed device detects the approach of passengers on the platform in real-time from camera footage to notify the driver of it, providing assistance in safety checks. Additionally, the device is equipped with the function of automatic passenger counting at each station. This paper presents an overview of the developed device and reports the results of the evaluation experiments.

Aluminothermic Welding Method Applicable to Shinkansen High-Speed Sections
Yoshihiro TERASHITA, Yuta TAKAGI
(Vol.37, No.12, 9-16, 2023.12)

In a previous study, aiming at introduction of an aluminothermic welding method to Shinkansen lines, we developed the aluminothermic welding method that can improve bending fatigue strength. However, since the rails at the base of the rail foot weld collar did not melt slightly, and this had to be removed by grinding. In addition to this, there is concern about the occurrence of "solidification crack" in the aluminothermic welding method, which is a factor preventing its introduction to the Shinkansen lines. Therefore, in this study, we solved the problem that the rail at the base of the rail foot weld collar does not melt by improving the mold shape and welding conditions. We also generally clarified the mechanism of solidification crack and proposed a welding procedure to prevent it.

Study on Interlocking Device on Cloud Computing Environment
Natsuki TERADA, Shunsuke SHIOMI, Takashi TOYAMA
(Vol.37, No.12, 17-25, 2023.12)

We report our study and proposal on interlocking devices in a cloud computing environment, which realizes resilience, reduction of time and cost for replacement, and provides the interlocking process as a service. The proposed system has the feature of processing interlocking logics of different stations independently. The proposed system has three layers: terminal devices to interface track circuits, signals, and switches, etc., logic units to process interlocking logics, and controllers to assign the interlocking table to logic units. We defined the specification of the terminal devices, logic units and controllers, and carried out verifications on them.

Development of Automatic Calculation Method for Maintenance Worker Scheduling Using Tabu Search
Tatsuya KOKUBO, Satoshi KATO, Taichi NAKAHIGASHI
(Vol.37, No.12, 27-33, 2023.12)

Maintenance worker scheduling is a daily schedule for each worker group to perform inspection and maintenance work such as cleaning of rolling stock during a turnaround operation of a superior trains at a terminal station. Since it varies from day to day according to changes in daily train timetables and rolling stock operations, it is required to be created for each day. We have proposed a method for automatic creation of maintenance worker schedules with tabu search, one of meta-heuristics. In this paper, to confirm the effectiveness of the proposed method, we compared an actual schedule with schedules by proposed method. The results indicated that the proposed method could generate a stable solution within a practical computation time of 3 minutes, regardless of the size of the train schedule.

Introduction Manual of Natural Frequency Identification System of Bridge Piers by Constant Microtremor Measurement
Satoshi WATANABE, Hiroki IRI, Shoma FUJIWARA
(Vol.37, No.12, 35-40, 2023.12)

In recent years, disasters have frequently occurred due to rapid river flooding and prolonged high water levels caused by typhoons and localized heavy rainfall. It is therefore necessary to establish a method for monitoring the destabilization of river piers during rising water. In response to this need, we have prepared an introduction manual for a natural frequency identification system, which that includes an the algorithm for identifying the natural frequencies of piers from microtremor measurements, the basic specifications of the acceleration sensors required to construct a microtremor measurement system, the application conditions of this system, and methods for evaluating the measurement results.

Elucidation of Noise Near the Bogie using Sound Source Visualization Method
Minoru SASAKURA
(Vol.38, No.1, 1-7, 2024.1)

There are many sources of noise generated from equipment such as gear devices for a railway vehicle installed in the narrow space of a bogie frame under the floor of a vehicle. Therefore, it is difficult to separate sound sources onboard a vehicle with a sound level meter, and up to now there is no method for separating sound sources. As a method to solve this problem, we are working on applying a sound source visualization method to noise measurement of railway drive device. As the sound visualization method, the 4-channel beamforming method (BF method) and the envelope intensity method (EI method) are used as appropriate, and the test results are compared. This paper reports the results of noise measurement using a sound source visualization method in a bench test of a drive device, and the results of a study on improving accuracy. We confirmed that the beamforming method has excellent imaging stability for transient sounds, and that image processing using multiple small microphone arrays improves the imaging accuracy of the BF method.

Snow Falling Experiments and Modeling to Simulate Phenomena of Snow Falling from Railway Vehicle
Yasushi KAMATA, Hiroki TSUJI, Daisuke TAKAHASHI
(Vol.38, No.1, 9-15, 2024.1)

In order to elucidate the mechanism of snow-falling from railway vehicles in winter, a mathematical model was studied to estimate the time taken for snow to fall in a warm tunnel. In addition, to validate the model which is based on the heat balance to the accreted snow plate, snow-falling experiments were carried out in a low-temperature room, and the onset time of snow-falling was compared between the model and the experiments. The result showed that it was possible to estimate the onset time when snow-falling begins, by setting the appropriate influence range on snowmelt at the interface between the plate and the accreted snow in the model.

Proposal of an Equation for Calculating Fatigue Strength of SD685 Rebar Considering the Range of High Frequency Repetitive Loading
Yuki NAKATA, Masaru OKAMOTO, Ken WATANABE, Toshiya TADOKORO
(Vol.38, No.1, 17-20, 2024.1)

The slope k of the S-N line in the range of high-frequency repetitive loading used in the current equation for calculating the fatigue strength of SD685 rebars is not unmitigated because of the small number of experimental data. In this paper, an equation for calculating the fatigue strength of SD685 rebars was proposed based on experimental data including the range of high-frequency repetitive loading. SD685 rebars had k=0.22 within 2×10^6 cycles, which was larger than that of SD490 rebars. On the other hand, it was found that the fatigue strength can be calculated on the safe side at 2×10^6 cycles or more even if k is set to 0.06, which is the value of SD490 rebars.

Field Verification of Combining Ballast Tamping and Rail Grinding and Application to Planning System
Shuhei KONNO, Mami MATSUMOTO, Kenya MORI
(Vol.38, No.1, 21-26, 2024.1)

In ballasted tracks, track irregularity and rail surface irregularity gradually increase due to the load of repeated train running. To repair these irregularities, ballast tamping or rail grinding are performed as the general maintenance work. This paper verifies effect of combining these two types of track maintenance to reduce a speed of track deterioration. Furthermore, extending the previously developed combined maintenance planning system, the authors simulate maintenance plans considering the effect of combined maintenance.

Concrete Creep Strain Estimation Formula and Design Values of Concrete by Considering the Strength Development

Ken WATANABE, Mami NAKAMURA

(Vol.38, No.1, 27-32, 2024.1)

Based on a literature survey on creep of mixed cements, this paper presents an estimation of creep coefficients in order to investigate design values of creep coefficients for different types of cement., An compressive strength estimation formula during loading used to calculate the creep strain used in estimating the creep strain coefficient was formulated based on the existing compressive strength estimation formula. First, the design values of creep coefficients for effective prestress calculations are presented. The values were calculated assuming cement types and standard conditions for prestressed concrete (PC) bridges. Then the authors confirm the effect of the creep coefficients on the verification of simple PC girder.

QUARTERLY REPORT of RTRI

第 65 巻　第 1 号
2024 年 2 月 1 日　発行
監修・発行所：公益財団法人鉄道総合技術研究所
〒 185-8540　東京都国分寺市光町 2-8-38
発行人：芦谷公稔
問い合わせ：鉄道総研広報

Vol. 65, No. 1
Published date: 1 February 2024
Supervision/Publisher: Railway Technical Research Institute
Address: 2-8-38 Hikari-cho, Kokubunji-shi, Tokyo 185-8540, Japan
Issuer: Dr. Kimitoshi ASHIYA
Contact us: Public Relations, Railway Technical Research Institute
Mail Address: rtripr@rtri.or.jp

QUARTERLY REPORT of RTRI

RAILWAY TECHNICAL RESEARCH INSTITUTE

Printed in Japan